Deuteron Production in Au+Au Collisions at 11.7 AGeV/c

Arata KUMAGAI

January, 1997

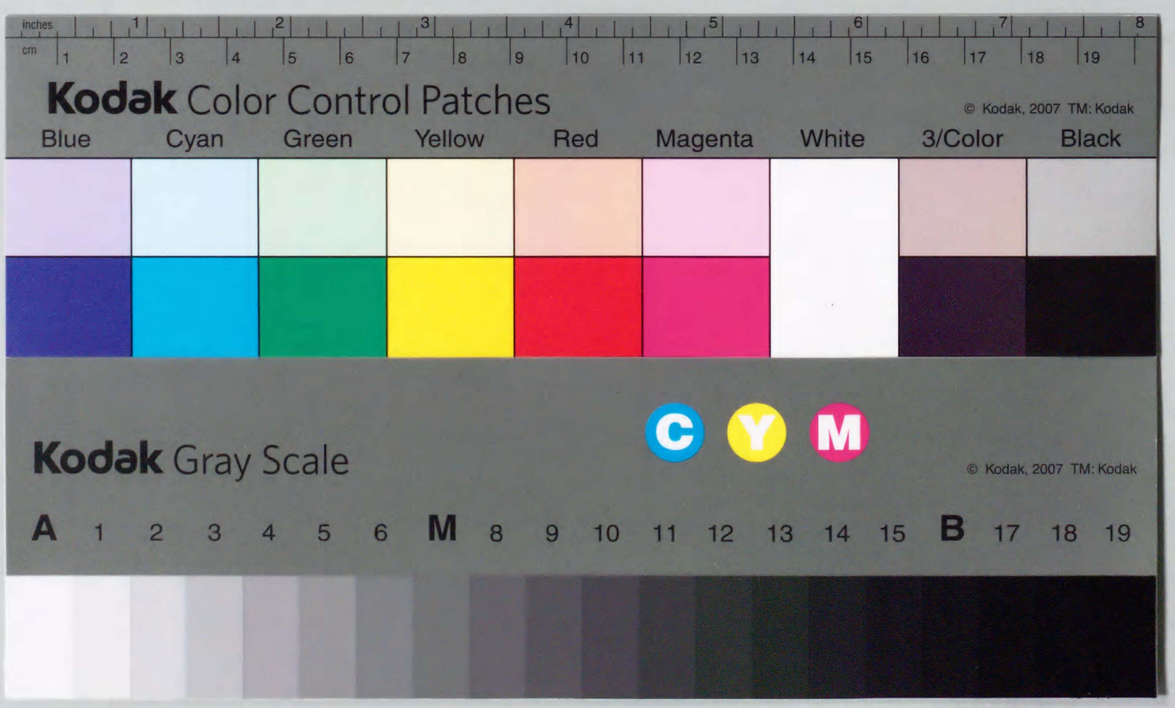

Deuteron Production in Au+Au Collisions at 11.7 AGeV/c

Arata KUMAGAI

A dissertation submitted to the Doctoral Program
in Physics, the University of Tsukuba
in partial fulfillment of the requirements for the
degree of Doctor of Philosophy(Physics)

January, 1997

Abstract

At Brookhaven National Laboratory (BNL), the first heavy ion beam was accelerated in 1986 using the Alternating Gradient Synchrotron (AGS). Furthermore, the AGS started the acceleration of ^{197}Au at 11 A·GeV/c since 1992. This beam energy in heavy ion collisions corresponds to the maximum energy for the projectile nucleus to be stopped by the target nucleus. When they achieve full stop in the center mass system of collisions, the density of the central region is expected to go up by a factor of $2\gamma_{cm}$. At the AGS energy, in other words, the density will be over five times of the normal nuclear density, which may lead to the QCD phase transition.

In order to measure hadron productions in Au+Au collisions, we have constructed a new dedicated spectrometer, Forward Spectrometer, which is designed for the high particle density and for the powerful particle identification capability. We have carried out systematic measurements of semi-inclusive spectra of various identified hadrons from ^{197}Au+^{197}Au collisions at 11.7 A·GeV/c as AGS-E866 experiment at BNL. The first data with the Forward Spectrometer were taken in October, 1993, and data with large statistic were taken in September - October, 1994.

To confirm the formation of hot and dense states of matter in the experiments, it is crucially important to measure the size of hot and dense region together with the measurement of the temperature. Among several methods proposed, measurement of composite particle is expected to give the information on the size of hot and dense region particularly for the baryonic gas.

The production of composite particles have been studied in A+A collisions at Bevalac and also in p+A collisions at CERN. Most successful description of those data is given by the Coalescence Model. As an example, deuterons are produced when a proton and a neutron are formed close enough in the phase space with the Coalescence Model. Then, the production rate of composite particle with mass number A is proportional to the A-th power of the proton(neutron) density in the phase space assuming proton and neutron are identical. This relation is called as a power law. It has been shown that the power law holds not only in the coalescence model, but also in a model which assumes thermal equilibrium. Experimentally the power law has been observed in many collisions at various beam energies.

With the Forward Spectrometer of the AGS-E866, proton and deuteron spectra were measured with event characterization in the wide kinematic coverage; $0.2 < p_t < 1.7$ [GeV/c] at $1.4 < y < 1.6$ for proton and $0.2 < p_t < 1.7$ [GeV/c] at $1.2 < y < 1.4$ for deuteron. From its much wider kinematic coverage and the full event characterization capabilities than the previous experiments, we claim that this is the first systematic measurement of deuteron production at the AGS heavy ion program.

We have shown that the observed deuteron spectra are consistent with the power law and also the scaling coefficient, B_2 stays constant in the whole rapidity range of this measurement. Since this thesis contains data of deuteron only, we cannot claim all the composite production follows the power law. But, the deuteron production in the kinematic region covered in this experiment has been shown to be consistent with the power law.

Furthermore, we found that the scaling coefficient, B_2 depends strongly on the centrality of the collisions. This is the first real measurement of the centrality dependence of B_2. To explain this dependence, spatial proximity of nucleon is considered as an additional condition to the deuteron production. Using the Sato-Yazaki model and also the thermal model developed by Mekjian, we have evaluated the source sizes from the B_2. The deduced source sizes are similar in both model calculations and are proportional to the cubic root of the number of participants, which implies that the deuteron density stays constant from the peripheral to the central collisions of the Au+Au collisions at AGS.

Contents

Chapter 1

Introduction

1.1 Relativistic Heavy Ion Collision

It has been proposed that nuclear matter formed in relativistic heavy ion collisions is dense and energetic so that quarks are no longer confined to each individual nucleon but move freely in a relatively large volume. This new phase of matter is called as a quark gluon plasma(QGP) [1, 2]. According to Lattice QCD calculations [3], phase transition from ordinal hadrons to the QGP is expected at critical temperature of 150 - 200 MeV. Enthusiasm to create such extremely high temperature and high density states of matter initiates modifications of existing proton synchrotron for heavy ion acceleration as well as construction of dedicated heavy ion machines.

The first relativistic heavy ion beam was obtained in 1974 at Bevalac in Lawrence Berkeley Laboratory(LBL). Existing proton synchrotron was modified for heavy ion acceleration up to 2 A·GeV/c. The experimental results certified that relativistic heavy ion collisions are indeed not simple superpositions of nucleon+nucleon collisions but global phenomena. To study those phenomena in collisions of increasing size and beam energy, the Alternating Gradient Synchrotron (AGS) at Brookhaven National Laboratory (BNL) in USA and the Super Proton Synchrotron (SPS) at CERN in Europe have been modified to accelerate heavy ions. The AGS started the acceleration of ^{16}O and ^{28}Si beams at 14 - 15 A·GeV/c since 1986 and ^{197}Au at 11 A·GeV/c since 1992. The SPS started the acceleration of ^{16}O at 200 A·GeV/c since 1987 and ^{208}Pb at 160 A·GeV/c since 1994. Furthermore, at BNL the Relativistic Heavy Ion Collider (RHIC) is now under construction which will provide colliding Au beams at 100 A·GeV/c in 1999.

The goal of heavy ion programs is to confirm the creation of high density and high energy state in the collisions and hopefully to detect the formation of the QGP. For this purpose, first of all, one has to study the reaction mechanism of heavy ion collisions. This is because one has to know how much initial kinetic energy is transfered to the thermal energy and what is the size of "Fire ball" created in the collisions in order to know the energy density achieved in heavy ion collisions.

1.2 Scenario of Collisions at AGS

Elementary process of heavy ion collisions at a few hundred MeV or above is the nucleon+nucleon collision. At low energies, the angular distribution of particle production in nucleon+nucleon collisions is almost isotropic in the center of mass frame. After the first collision, the scattered nucleon easily escapes out of the reaction region. However, at high energies, the angular distribution is sharply forward and backward peaked. Therefore, the scattered nucleons and the produced particles are forced to dive into the opponent nucleus and experience the further successive collisions until they stop in the c.m. frame. Obviously, there is maximum energy above which the projectile and its leading particle penetrate through the total thickness of opponent nucleus. The beam energy of 10 A·GeV is believed to correspond to this maximum energy.

At the AGS energy, the Lorentz contracted nuclei stops each other after violent nucleon+nucleon collisions. When they achieve full stop at the c.m., the density is expected to go up by a factor of $2\gamma_{cm}$. With this scenario, the density will reach five times of the normal nuclear density at the AGS.

In the first phase experiments of AGS heavy ion program, intensive studies were carried out to check out whether such stopping scenario holds or not. As a direct proof of the stopping, proton distributions have been studied. In Fig. 1.1 [4], rapidity distribution of proton in central Au+Au collisions are compared with peripheral Si+Al and central Si+Al collisions [5]. The distribution in peripheral Si+Al shows forward/backward peaking, which is similar to that of p+p collisions [43]. In central Si+Al collisions, the distribution shows peaks of "projectile-like" and "target-like" participating protons. In central Au+Au, however, it shows a broad peak at the c.m.. Indeed, a large fraction of participating nucleons is shown to be piled up in the collisions, which is consistent with the stopping scenario described above. The

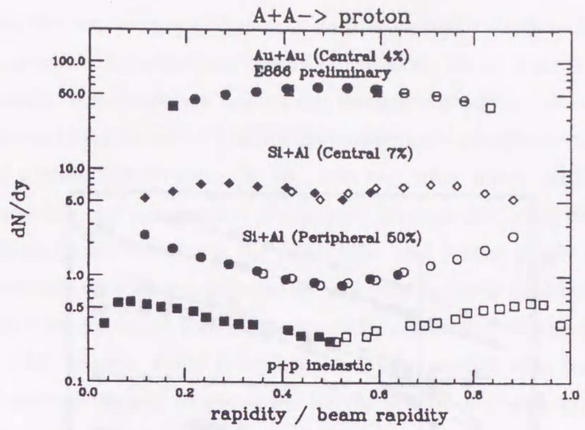

Fig. 1.1: Rapidity distributions of protons in Au+Au, Si+Al [5] and p+p [43] collisions. The dN/dy is plotted versus the normalized rapidity y/y_{beam}. The filled symbols are the measured data while the open symbols represents the data reflected with respect to the y_{cm}.

Au+Au collisions at AGS might provide great opportunity to study the high density states of matter.

1.3 Size of Reaction Volume

Important questions for the study of heavy ion collisions are the following: How hot and dense region is created, over what volume and for how long ? Particularly, the size of the hot and dense region is important subject for the experimentalists. Two methods have been proposed to measure the size of the reaction volume; Hanbury-Brown Twiss measurements [6] with two pions or two kaons detection and the coalescence parameters of composite particle productions (the latter method is discussed in Section 6.5). We consider the size information from the composite particle measurement is more appropriate at the AGS energy from the following argument. As discussed, the dominant features of the heavy ion collisions are given by the nucleon+nucleon collisions. In Fig. 1.2, rates of particle production in a collision is as small as 4 at the AGS energy. In other words, there is single pion produced per nucleon. Furthermore, those secondary pions are believed to be emitted via excited states of baryons, such

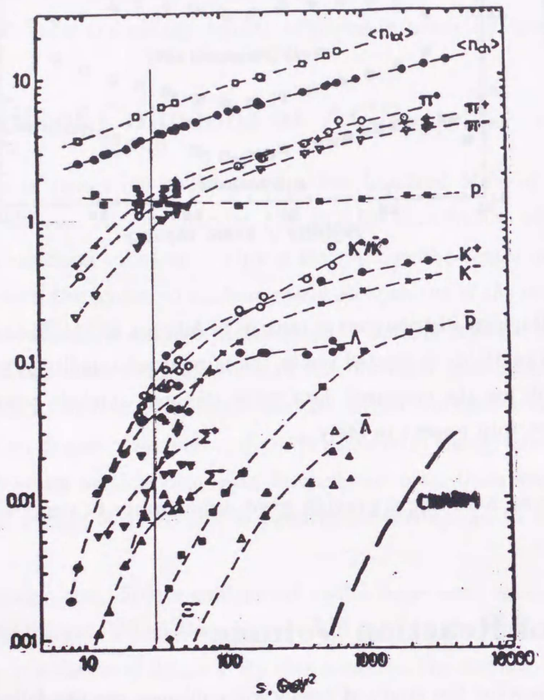

Fig. 1.2: Number of produced particles versus the squared total energy at the center of mass frame, s in p+p collisions. The solid straight line shows the AGS energy, $s = 30$ GeV^2 corresponding to the beam with incident momentum of 15 GeV/c and target. The total number of produced charged particles, n_{ch} is about 4 at the AGS energy.

as Δ's. Indeed, the importance of baryonic collisions, particularly of low lying resonances was understood from the comparison of the pion/proton data with the several model calculations. Any models of naive intra nuclear cascade are shown to overestimate the pion yield by a factor of 2 while they underestimate the average transverse momentum of protons significantly [9, 10]. On the other hand, ARC [11, 12] and RQMD [13] models which treats pion production through low lying resonances such as Δ's, have been shown to explain the pion, kaon and proton production properly. From these successes, it is widely believed by now that baryons particularly low lying resonances play the dominant role in the particle production in the heavy ion collisions at the AGS energy. From this viewpoint, we consider that baryons such as protons and deuterons should be measured for the studies of the reaction size.

1.4 Power Law

The most successful model to describe composite particle production in A+A collisions at Bevalac is the coalescence model [14, 15, 16]. With this model, when a proton and a neutron are accidentally emitted close together in the momentum phase space in a nucleus+nucleus collision, the proton and the neutron coalesce into a deuteron. Therefore, the yield of deuteron should be proportional to the squared density in the momentum phase space of proton (neutron). The relation can be written with invariant differential yield as;

$$E_d \frac{d^3Nd}{dp_d^3} \propto \left(E_p \frac{d^3Np}{dp_p^3} \right)^2 \tag{1.1}$$

where $p_d = 2 \cdot p_p$. In general, for the composite particle consisting of A nucleons, Eq. 1.1 is extended to;

$$E_A \frac{d^3N_A}{dp_A^3} = B_A \left(E_p \frac{d^3N_p}{dp_p^3} \right)^A , \tag{1.2}$$

where $p_A = A \cdot p_p$. Those relations assume that the shapes of the proton and neutron spectra are identical. This relation is called as a power law of the coalescence model.

It turned out that this power law can be explained by a thermal model [47, 48, 49]. The model is static, non-relativistic and assumes thermal and chemical equilibrium to be achieved and composite particles are produced uniformly over the volume. This model is further discussed in Section 6.5.1.

The power law has been applied to light nucleus in A+A collisions with incident energy from 9 A·MeV to 2 A·GeV [17, 18]. Furthermore, it has been shown that

the power law can describe the spectra of the light nucleus from deuteron to ^{14}N, in Fig. 1.3 [18]. However, it is known that the disagreement of the power law is as large as some ten percent at low p_t region. It may be due to the difference of the distribution between proton and neutron. Thus the measurement at wide p_t region is important to test the power law.

Fig. 1.4 shows that the values of B_2 are almost constant for A+A collisions at Bevalac [46, 17] and p+A collisions [20] at CERN. It has been believed that the B_2 does not depend the beam energy and the collision system. This uniformity of the B_2 is remarked as a universality of the composite particle production.

1.5 Deuteron Measurements at AGS

Previously deuteron measurements have been performed in the relativistic heavy collisions at AGS.

One of them was performed by E814 group. They measured cross sections of the composite particles of mass $A \leq 4$ in collisions of 14.6 A·GeV/c ^{28}Si nuclei with targets of Pb, Cu, and Al [21]. However, they do not have proton data in the kinematic regions for deuteron to be compared with their experimental coverage. They are forced to use model prediction (ARC model [11, 12]) instead of real data for proton spectra in order to test the power law, which by no means can be considered as an experimental proof. Furthermore, their p_t coverage is narrow: p_t as $0 < p_t < 0.14$ [GeV/c] for deuteron.

E886 group measured composite particles, deuteron, triton, ^{3}He and ^{4}He at magnetic rigidities of p/Z = 0.8, 1.2, 1.5, and 1.8 GeV/c in collisions of ^{197}Au beam of 12 A·GeV/c with target of Pt [22]. They have shown that the power law holds to the inclusive production cross section of the deuteron, triton, ^{3}He and ^{4}He, as shown in Fig. 1.5. Since they do not have an event characterization detector, their data are only for inclusive measurements. For comparison, they also measured the composite particles in ^{28}Si+Pt collisions of 14.6 A·GeV/c and p+Pt collisions of 12.9 GeV/c. Furthermore, the source radii which were deduced from the Sato-Yazaki model [50] were proportional to the cubic of the number of participant nucleons. However, the evolution of collision might be quite different in central and peripheral collisions, such as ^{197}Au+^{195}Pt. Specifying impact parameter is preferable in heavy ion collisions. Furthermore, since they used a beam line spectrometer system fixed at 5.7 deg,

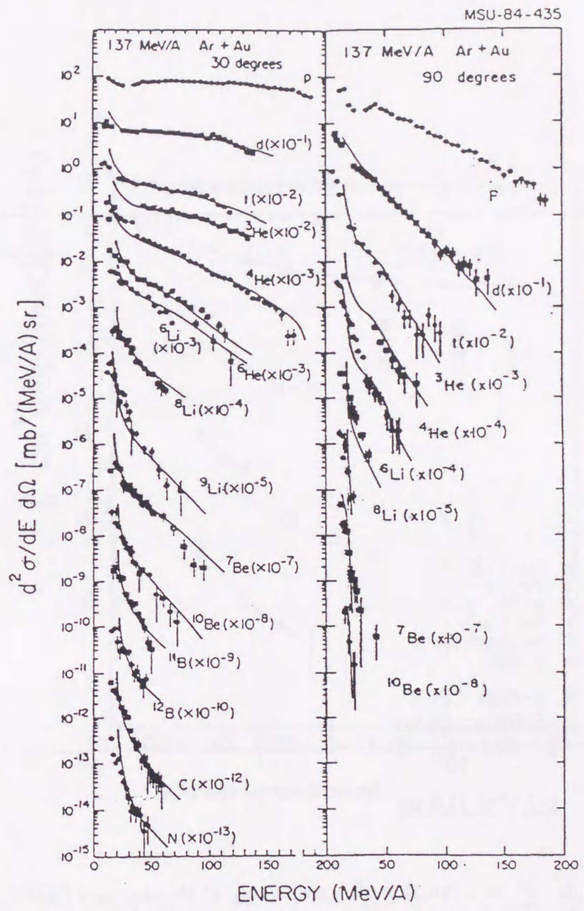

Fig. 1.3: The power law test for the range of $2 \leq A \leq 14$ at Bevalac. Differential cross section for fragments from 137 A·MeV Ar+Au at 30 deg. and 90 deg. [19]

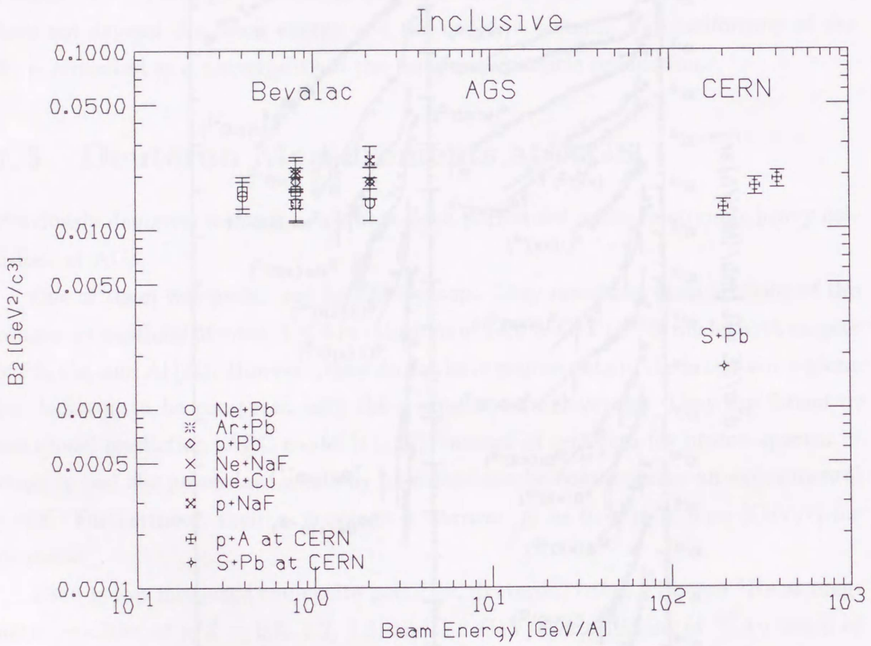

Fig. 1.4: B_2 as a function of beam energy at Bevalac and CERN.

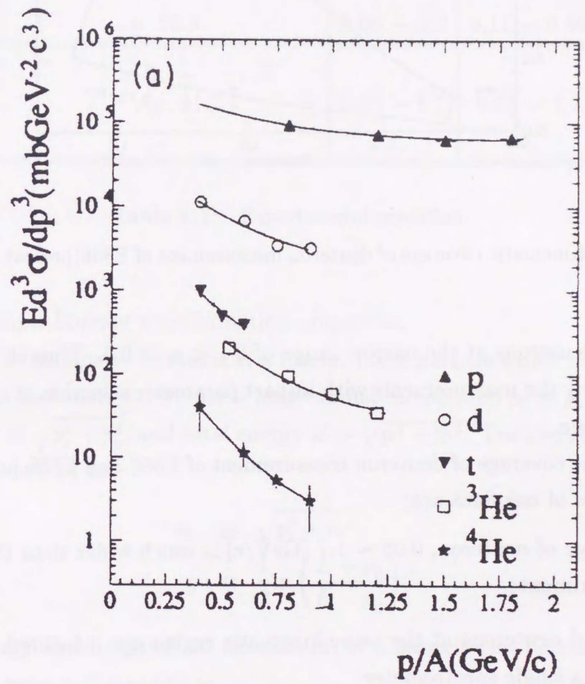

Fig. 1.5: The power law test for d, t, ^{3}He and ^{4}He in Au+Pt collisions at AGS (E886) [22]. The curves in the figure are the results of a coalescence fit.

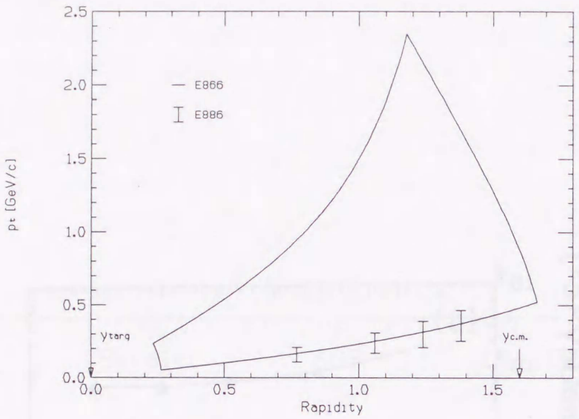

Fig. 1.6: Kinematic coverage of deuteron measurement of E866(present data) and E886.

they measured deuterons at the narrow range of $0.1 < p_t < 0.5$. Thus it is awaiting to be confirmed by the measurements with impact parameter selection at much wider kinematic coverage.

The kinematic coverage of deuteron measurement of E866 and E886 are shown in Fig. 1.6. Features of our data are;

- The p_t range of deuteron, $0.05 \sim 1.7$ [GeV/c] is much wider than those of the other experiments.
- Protons and deuterons at the same kinematic region are measured simultaneously with a single spectrometer.
- The centrality of collisions are also measured.

We claim that our data is the first systematic measurement of deuteron production in Au+Au collisions at AGS energy.

The experimental conditions are summarized in Table 1.1.

1.6 Kinematics

Here, we introduce kinematic variables. Since we are dealing with relativistic particles and systems, it is useful to describe them with Lorentz invariant variables or variables

Experiment	Beam, Momentum [A·GeV/c]	p_t range [GeV/c]		centrality
		p	d	
E814	^{28}Si, 14.6	–	$0 - 0.14$	inclusive 6 centrality cuts
E886	^{197}Au, 11.5	$0.06 - 0.2$	$0.11 - 0.46$	inclusive
	^{28}Si, 14.6	~ 0.2	~ 0.46	inclusive
	p, 12.9	$0.06 - 0.2$	$0.11 - 0.46$	inclusive
E866	^{197}Au, 11.7	$0.05 - 1.7$	$0.05 - 1.7$	inclusive central peripheral

Table 1.1: Experimental condition.

which have simple Lorentz transformation properties.

We take a beam line to be z-axis of a frame. For a particle which has momentum $\mathbf{p} = (p_x, p_y, p_z)$ and mass m, we use a longitudinal momentum $p_{\parallel} \equiv p_z$, a transverse momentum $p_t \equiv \sqrt{p_x^2 + p_y^2}$, and total energy $E = \sqrt{\mathbf{p}^2 + m^2}$. Transverse mass m_t and rapidity y are defined as

$$m_t \equiv \sqrt{p_t^2 + m^2} \tag{1.3}$$

$$y \equiv \frac{1}{2}\ln\left(\frac{E + p_{\parallel}}{E - p_{\parallel}}\right). \tag{1.4}$$

The total energy and longitudinal momentum of a particle can be easily related to its transverse mass and rapidity as

$$E = m_t \cosh(y) \tag{1.5}$$

$$p_{\parallel} = m_t \sinh(y). \tag{1.6}$$

1.7 Thesis Objectives

The data presented in this paper was obtained in the fall of 1994. Event characterization was performed by the Bull's Eye counter and the zero-degree calorimeter. From the experimental results, we get the information of the size of the interaction volume at freeze-out, utilizing the coalescence model and compare it with other experimental

results. A particular interest is in the size of the coalescence scaling coefficient, B_A and its dependence on the centrality.

In this thesis, we describe the experimental setup in chapter 2, the run condition in chapter 3 and calibrations of detectors, particle identification and corrections in chapter 4. In chapter 5, we present the experimental results. The results are discussed in chapter 6 on basis of coalescence relation, and compared with other experimental results. Conclusions are described in chapter 7.

1.8 Contribution of Author

The author has contributed to AGS-E866 experiment as following,

- Has taken part in construction of the Forward Spectrometer since he was master degree.
- Constructed the time of flight wall with Ueno-Hayashi.
- Worked on development of the on-tube discriminator, which was used to the time of flight wall, as master thesis. Then high resolution, $\sigma \sim 76$ psec, was kept during experimental run.
- Calibrated the time of flight wall.
- Analyzed the deuteron production.

Chapter 2

Experimental Setup

2.1 Overview

Fig. 2.1 shows the configuration of the experiment E866. It consists of a large solid angle (25 msr) magnetic spectrometer (Henry Higgins Spectrometer), a small solid angle (5 msr) magnetic spectrometer (Forward Spectrometer), and event characterization detectors. In this chapter, the accelerator facility, the target arrangement, event characterization detectors and the detector components in the Forward Spectrometer are described.

2.2 Accelerator facility

Fig. 2.2 shows the layout of the heavy ion accelerator facility at Brookhaven National Laboratory. First, the Au beam is accelerated to 1.00 MeV per nucleon with a charge state of 13+ at Tandem Van de Graaff accelerator. And the beam is transferred to Booster ring through Heavy Ion Transfer Tunnel, and accelerated to 192 MeV per nucleon with a charge state of 33+. Finally, the beam is accelerated up to 11.7 A·GeV/c with a charge state of 79+ at AGS main ring [24], and led to the E866 experimental area. The beam had the repetition cycle of ~ 4 sec, and the flat top of ~ 1 sec per spill.

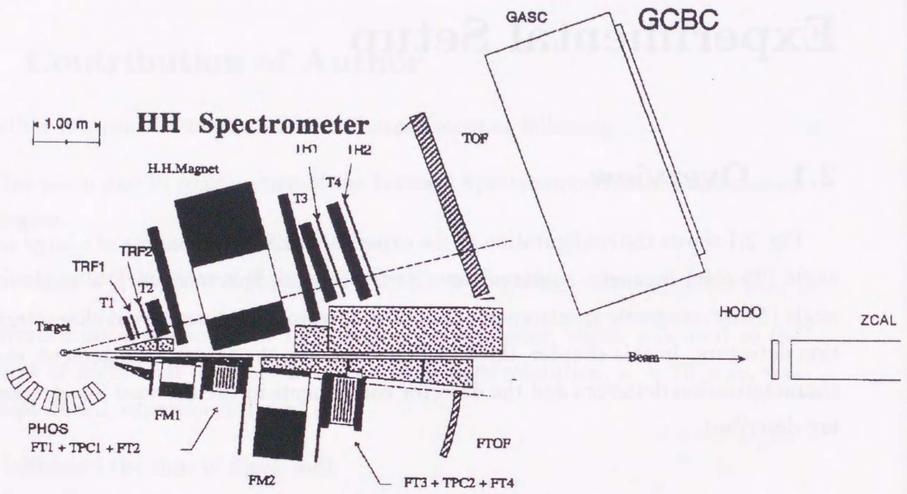

Fig. 2.1: The top view of the E866 spectrometer.

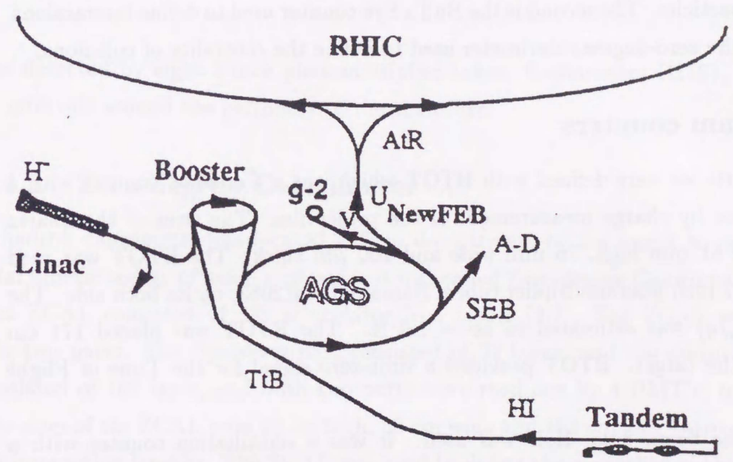

Fig. 2.2: A schematic layout of the AGS accelerator complex.

2.3 Target Arrangement

Each target is mounted in an aluminum frame. The whole target assembly is in vacuum. The target assembly has six target holders. One of the six is always kept open and used as empty target for the background study. The targets are positioned by remote control.

2.4 Global Detectors

Three global detectors are described in this section. The first is beam counters used to define beam particles. The second is the Bull's Eye counter used to define interactions. The third is the zero-degree calorimeter used to define the centrality of collisions.

2.4.1 Beam counters

The beam particles were defined with BTOT which was a Čerenkov counter with a quartz radiator by charge measurement of the projectiles. The sizes of the quartz radiator were 51 mm high, 76 mm wide and 200 μm thick. The BTOT was read out with two 2-inch photomultiplier tubes, Hamamatsu R2083, on its both side. The resolution (σ_q/q) was estimated to be $\sim$ 1.9 %. The BTOT was placed 171 cm upstream of the target. BTOT provided a time-zero signal for the Time of Flight system.

To veto the beam halo, Hole was used. It was a scintillation counter with a circular hole 10 mm diameter. The size of its scintillator was 51 mm high, 76 mm wide and 3 mm thick. It was placed 145cm upstream. Specifications of the counters are summarized in Table 2.1.

2.4.2 Bull's Eye counter

Bull's Eye counter was used to detect an interaction of a beam nucleus with a target nucleus. The counter was a Čerenkov counter with a quartz radiator of 20 cm diameter and 300 μm thick. The Bull's Eye counter measured the charge of the remnant of the beam. The measured charge smaller than that of the beam particle provided the minimum bias interaction trigger. The resolution, σ_q/Z was $\sim$ 6.7 % in 1994 runs [26]. The schematic view of the Bull's Eye is shown in Fig. 2.3 [25]. The Čerenkov light

Counter	BTOT	HOLE
Material	Quartz	Scintillator
Thickness [mm]	0.20	3.2
Width [mm]	76.2	76.2
Height [mm]	50.8	50.8
Hole Diameter [mm]	–	10.
Distance from the Target [cm]	−171.	−145

Table 2.1: Specification of the beam counters.

was detected by eight 2-inch photomultiplier tubes, Hamamatsu H1161, located at 45 intervals around the periphery of the enclosure.

2.4.3 Zero-degree Calorimeter

A hadron calorimeter was located 11.7 m downstream of the target to measure the total kinetic energy of beam remnants. It was called Zero-degree Calorimeter(ZCAL). The ZCAL consisted of 138 scintillator/iron layers [27]. The ZCAL was divided into two parts. The Upstream part consisted of 32 layers and the downstream part consisted of 106 layer, and both two parts were read out by 4 PMT's, respectively. The sizes of the ZCAL were 60 cm high, 60 cm wide and 193 cm long corresponding to 8.9 interaction lengths. The ZCAL was used to define the centrality of the collisions. The energy resolution of the ZCAL was $\sigma_E/\sqrt{E} = 2.88 \pm 0.02$ [GeV$^{1/2}$] in 1993 run [28].

2.5 Forward Spectrometer

The Forward Spectrometer consisted of a collimator, two dipole magnets, two tracking chamber complexes, and a time-of-flight wall. Each of the tracking chamber complexes consisted of a time projection chamber and two accompanying drift chambers, and one of two complexes was placed in front of the second magnet and the other one was placed behind of the second magnet. The spectrometer could be swept from 6 degrees to 24 degrees.

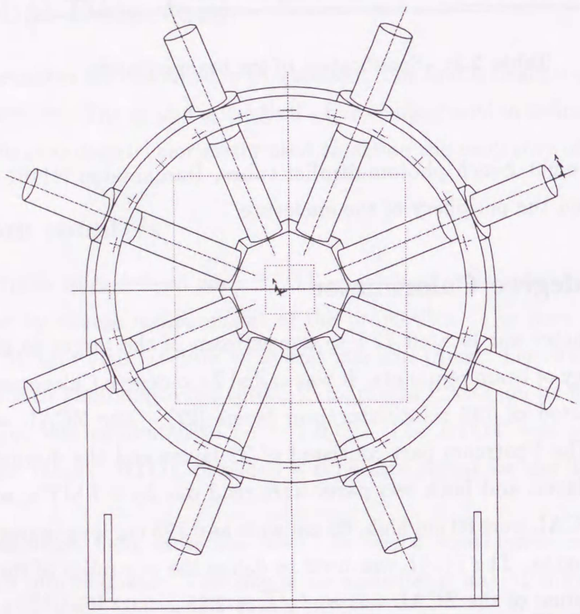

Fig. 2.3: A beam view of Bull's Eye [25].

To reduce the particle density at the detectors, the solid angle of the acceptance was designed to be rather small (5 msr) and the distance between the target and the center of first chamber complex was extended to be 2.5 m. The first magnet was placed in front of the first drift chamber to reject secondary particles with low momenta. Further, a collimator was placed upstream of the first magnet. The window of the collimator determined the acceptance of the spectrometer to be 4 degrees in the horizontal direction and $\pm$ 2 degrees in the vertical. It corresponds to the solid angle of $\sim$ 5 msr.

The time projection chambers were used to find and define tracks because of their high capability of three dimensional pattern recognition. Then the drift chambers used to determine precise hit positions and angles of the found tracks with their high spatial resolution.

The time-of-flight wall was placed 6 m downstream of the target as the device for particle identification. The time-of-flight wall had high resolution of 76 psec.

The performance of the spectrometer is summarized in Table 2.2.

	Performance
Solid angle [msr]	~ 5
Setting angle [degree]	$6 - 24$
Momentum resolution (σ_p/p) [%] (proton, $0 < p \leq 5$[GeV/c])	$1.5 - 5$
Time of flight resolution, $\sigma_{TOF}(\pi)$ [psec]	76.
$\pi - K$ PID separation (2.5σ) [GeV/c]	$0 < p \leq 2.5$
$K - p$ PID separation (2.5σ) [GeV/c]	$0 < p \leq 3.5$
$p - d$ PID separation (2.5σ) [GeV/c]	$0 < p \leq$

Table 2.2: Specification of the beam counters.

2.5.1 Forward Spectrometer Coordinate System

We defined a coordinate system on the spectrometer as in Fig. 2.4. The origin was at the target position. The z-axis called the 6-degree line was a line perpendicular to the surfaces of the magnets and the tracking chambers. The y-axis was upward. The x-axis was taken so that the coordinate system was the right handed system.

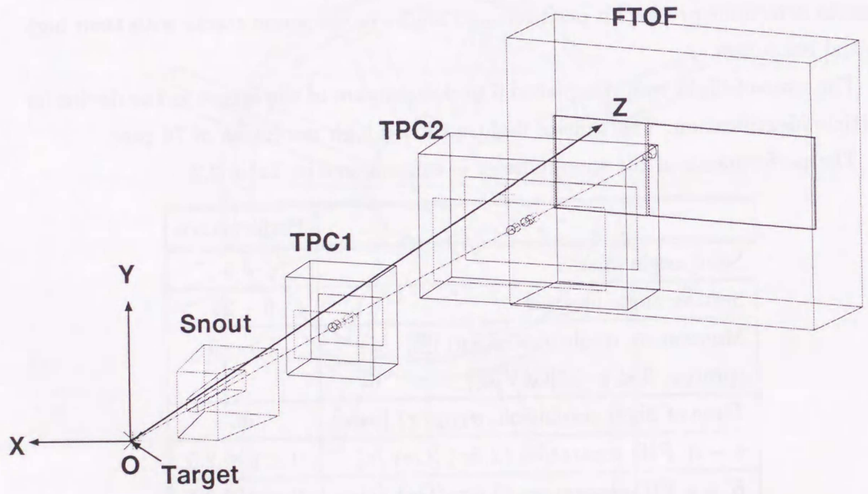

Fig. 2.4: A schematic view of the Forward Spectrometer to demonstrate the definition of the FS coordinate system. Note that M1 and M2 are not shown. A single reconstructed track is shown. The origin is at the target position. The z-axis is along the beam side of the spectrometer, whose beam-downstream direction is positive. The y-axis is vertical upward. The x-axis is determined so that the FS coordinate system is right-handed.

2.5.2 Magnets

We had two dipole magnets on the Forward Spectrometer. One called FM1 was placed in front of the first tracking chamber system to remove background particles with low momenta. The other called FM2 was placed between the tracking chamber systems as an analyzing magnet. FM2 had an 94 cm effective length and bending power of about 0.9 T·m at its full strength. Field maps of FM1 and FM2 were measured with Hall probes at 0.4T and 0.6T settings, respectively. Their specifications are summarized in Table 2.3.

Magnet	FM1	FM2
Distance from the target [mm]	1754.	3505.
Field Gap Size (x × y × z) [mm^3]	229. × 159. × 508.	597. × 283. × 762.
Yoke Size (x × y × z) [mm^3]	546. × 616. × 800.	1346. × 1442. × 1156.
Effective Field Length [cm]	623.2	943.4

Table 2.3: Specification of the beam counters.

2.5.3 Tracking Detectors

The spectrometer had two tracking chamber complexes. Both tracking chamber complexes consisted of one time projection chamber and two drift chambers. First, the time projection chambers found tracks, next the drift chambers improved spatial resolution of the tracks.

2.5.4 Time Projection Chambers

A time projection chamber (TPC) [29] was placed at the center of each tracking chamber complexes as a main tracking device.

Each of the time projection chamber consisted a field cage, an end-cap wire chamber, a gating grid plane and a gas cage. The time projection chamber measured the y-position as the drift time and x and z-position by the end-cap wire chamber. Fig. 2.5 shows the schematic structure of TPC1 [30].

The time projection chamber (TPC1) placed upstream of FM2 was operated with Ar-isobutane (75:25) mixture and the time projection chamber (TPC2) [31] placed

downstream of FM2 was operated with P-20. To operate time projection chambers under the high particle density condition, the readout scheme of the time projection chambers was segmented anode wire readout [34, 35], while conventional time projection chambers equipped at its end-cap MWPC with cathode pad readout [32, 33].

Further, TPC1 and TPC2 were equipped with gating grid systems to suppress field distortion due to the position ions from the anode wires. The gating grid was usually closed, and the bias voltage, $\pm$ 50 V for TPC1 and $\pm$ 80 V for TPC1, are supplied to each adjacent gating grid wires. When a trigger signal came, the gating grid was opened so that the drift electrons could pass through the gate to the anode wires. The performance of TPC1 and TPC2 is summarized in Table 2.4.

Chamber	TPC1	TPC2
Frame Size (x $\times$ y $\times$ z) [mm^3]	406. $\times$ 450. $\times$ 352.	965. $\times$ 660. $\times$ 450.
Field Cage Size (x $\times$ y $\times$ z) [mm^3]	300. $\times$ 248. $\times$ 280.	800. $\times$ 409. $\times$ 330.
Window Size (x $\times$ y) [mm^2]	300. $\times$ 220. $\times$ 280.	800. $\times$ 380.
Effective Field Length [cm]	623.2	943.4
Effective Volume (x $\times$ y $\times$ z) [mm^3]	290 $\times$ 200 $\times$ 280	770 $\times$ 350 $\times$ 330
Number of Rows	6	6
Row-to-Row Pitch [mm]	46.	54.
Drift Field [V/cm]	800.	640.
Maximum Drift Length [cm]	26.	42.
Anode-to-Anode Pitch [mm]	3.	4.
Anode-to-Cathode Gap [mm]	3.	4.
Effective Anode Wire Length [mm]	7.	7.
Anode Wire Diameter [μm]	15.	15.
Operation Voltage [-kV]	1.90	2.15 – 2.20
Number of Anode Wires [/row]	96	192
Total Number of Readout	576	1152
Gating Grid Wire Pitch [mm]	1.	1.
Grid-to-Cathode Distance [mm]	8.	8.
Gating Grid Operation Voltage [V]	$\pm$50.	$\pm$80.

Table 2.4: Specification of the time projection chambers.

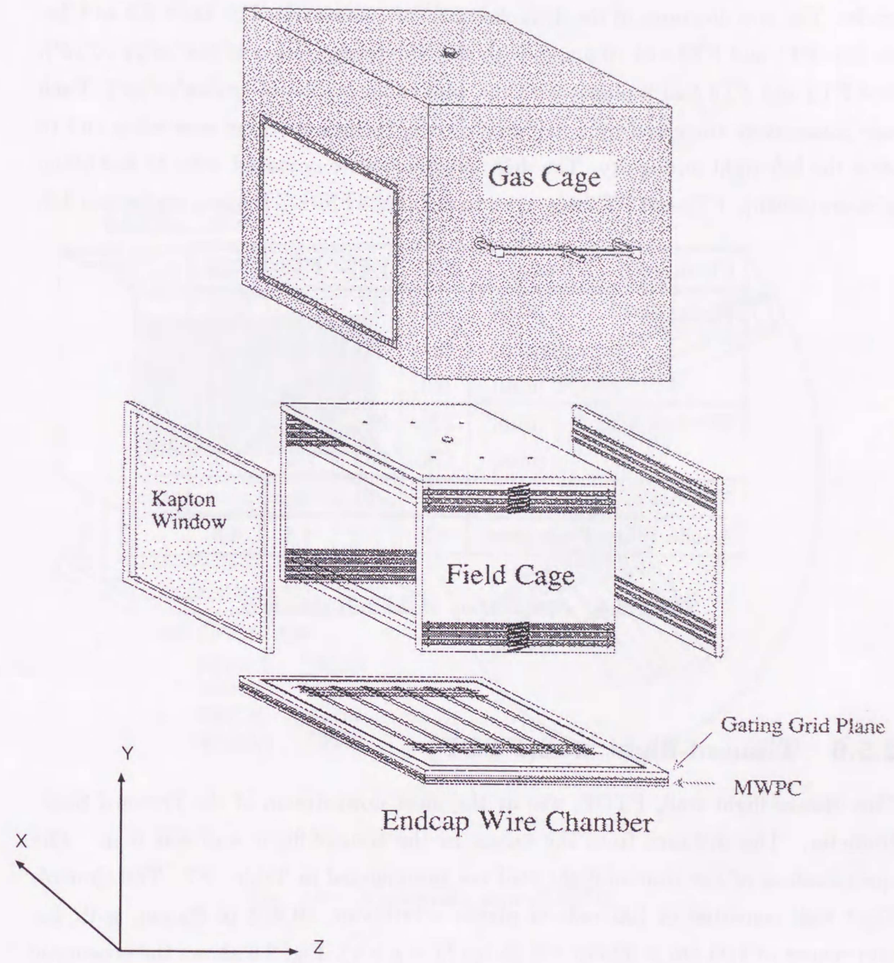

Fig. 2.5: A schematic structure of TPC's.

2.5.5 Drift Chambers

Four drift chambers (FT1 – FT4) were used to improve spatial resolution of the tracks. The specifications of the drift chambers are summarized in Table 2.5 and Table 2.6. FT1 and FT2 had 10 planes with the wire configuration of ($xx'uu'yy'vv'xx'$). And FT3 and FT4 had 8 planes with the wire configuration of ($xx'uu'vv'xx'$). Each pair planes were staggered by a half cell to cover inefficient region near wires and to solve the left-right ambiguity. The drift chambers were operated with Ar-isobutane mixture (50:50). FT2 and FT3 were used to define the FSPEC trigger (see Section 3.3.

Chamber		FT1	FT2	FT3	FT4
Frame Size	x [mm]	338.	503.	844.	1003.
	y [mm]	394.	394.	520.	520.
	z [mm]	60.	60.	81.	81.
Window Size	x [mm]	238.	353.	644.	803.
	y [mm]	174.	233.	320.	360.
Number of Planes		10	10	8	8
Anode Plane Pitch [mm]		3.2	3.2	4.8	4.8

Table 2.5: Specification of the drift chambers.

2.5.6 Time-of-flight wall(FTOF)

The time-of-flight wall, FTOF, was at the most downstream of the Forward Spectrometer. The distance from the target to the time-of-flight wall was 6 m. The specifications of the time-of-flight wall are summarized in Table 2.7. The time-of-flight wall consisted of 100 rods of plastic scintillator, BC404 of Bicron, with the dimensions of 1.24 cm × 42 cm × 1.25 cm ($x \times y \times z$). Fig. 2.6 shows the schematic view of FTOF. Each scintillator, called a slat, was read out with two 3/4 inch photomultiplier tubes, R3478S of Hamamatsu, through light guides on its both ends. Each PMT was mounted on a board which had a bleeder circuit for PMT and a discriminator, called on-tube discriminator [36]. The on-tube discriminator had two outputs: passively internally split analog signal and discriminated output. The discriminated signals were rediscriminated in the counting house to reshape the signals before send-

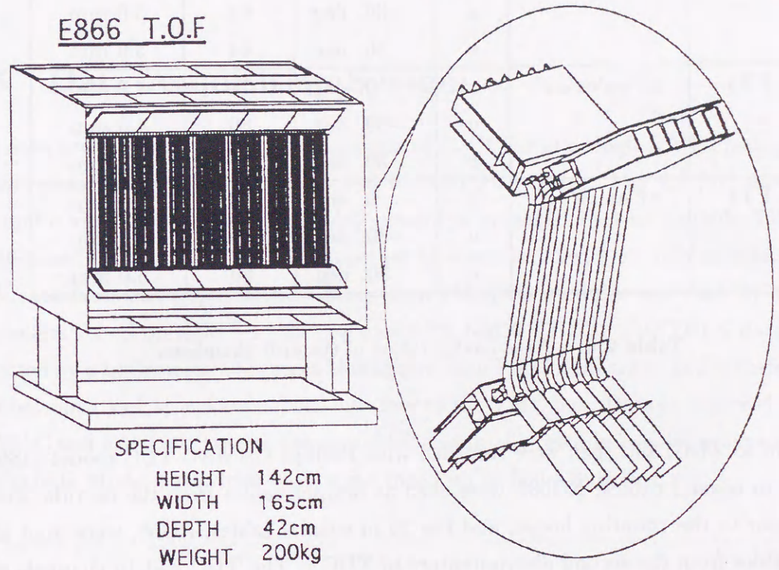

Fig. 2.6: A schematic view of FTOF.

Chamber	Plane Order	Wire	Orientation	# Wires	Drift Length
FT1	$xx'uu'yy'vv'xx'$	x	0. deg.	56	2.0 mm
		y	90. deg.	40	2.0 mm
		u	−30. deg.	64	2.0 mm
		v	30. deg.	64	2.0 mm
FT2	$xx'uu'yy'vv'xx'$	x	0. deg.	56	3.0 mm
		y	90. deg.	36	3.0 mm
		u	−30. deg.	64	3.0 mm
		v	30. deg.	64	3.0 mm
FT3	$xx'uu'vv'xx'$	x	0. deg.	78	4.0 mm
		u	−30. deg.	80	4.0 mm
		v	30. deg.	80	4.0 mm
FT4	$xx'uu'vv'xx'$	x	0. deg.	78	5.0 mm
		u	−30. deg.	80	5.0 mm
		v	30. deg.	80	5.0 mm

Table 2.6: Plane configuration of the drift chambers.

ing them to TDC, and then were recorded with Phillips CAMAC TDC model 7186. The 68 m coaxial cables, RG58f, were used as jumper cables from the on-tube discriminator to the counting house, and the 30 m coaxial cables, RG58, were used as delay cables from the second discriminators to TDC's. The TDC had 16 channels of time digitizers with the minimum bin of 25 psec. The analog signals were recorded with LeCroy FASTBUS ADC 1882N in the counting house. ADC values are used in off-line analysis for so-called slewing correction [1] as well as for a charge cut.

2.5.7 Heavy Metal Shields

The collimator was made of heavy metal, mainly Tungsten, was placed in front of the FM1 to screen chamber frames and the yoke of FM1. The heavy metal shield was also fixed on the beam side wall of FM1 in order to stop the particles from the beam pipes.

[1] correct the time changes which are caused from relation of the pulse height and threshold level of the discriminator

	FTOF
Flight-Path Length [m]	6.0
Effective Area ($x \times y$) [mm^2]	1260×420
Number of Slats	100
Slat Size ($x \times y \times z$) [mm^3]	$12.4 \times 12.5 \times 419.$

Table 2.7: Geometrical specifications of FTOF.

2.6 Data Acquisition System

The data acquisition (DAQ) system consists of 11 CPU's in a single VME create, and gathers data from 8 CAMAC crates and 6 FASTBUS crates. Fig. 2.7 [37] shows a schematic view of the DAQ. The DAQ system is managed by two Tadpole TP40V 68040-based CPU's which function together as event builder, data reformatter, network interface, and tape logger. Data from CAMAC modules are read by crate controllers based on SBE VPU25 modules with 68020 CPU's. FASTBUS data are collected by a LeCroy 1821 Segment Manager in each FASTBUS crate, and transferred via fiber-optic link to a custom-built interface to the VME bus. Data transferred from CAMAC and FASTBUS crates are assembled and finally recorded on 8 mm tape using an Exabyte Model 8510 drive with write speed up to 500 kByte/sec.

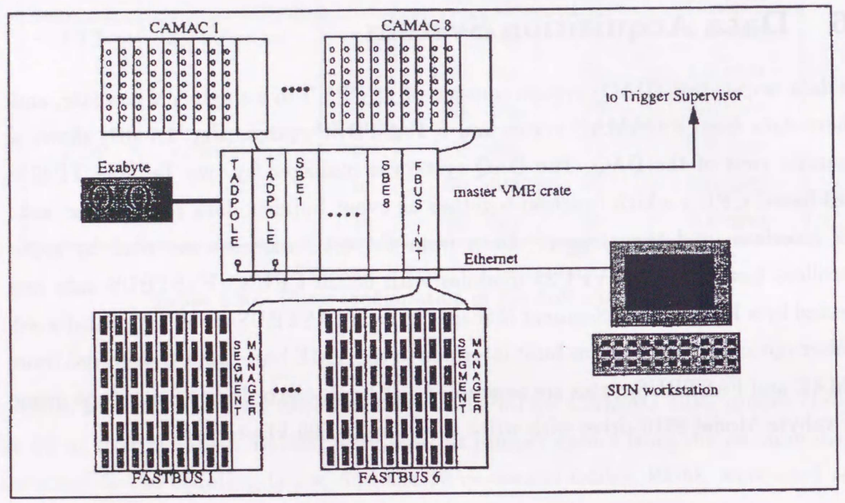

Fig. 2.7: A schematic view the E866 DAQ system [37].

Chapter 3

Experimental Runs

The E866 Forward Spectrometer was operated with the 11.7 A·GeV/c ^{197}Au beam from September to October in 1994.

3.1 Beam conditions

The beam intensity was adjusted at $(3-10)\times10^4$ particles per spill. It depended on the spectrometer setting angle. The beam size and location at the target position were monitored with the beam line chambers (SWIC). The beam size was also monitored with the counting rate of the beam counters.

3.2 Targets

We used a ^{197}Au target. Its thickness was 0.975 g/cm corresponding to the interaction rate of about 1.5 %. Data without a target (empty target) were also taken to subtract the background contribution.

3.3 Trigger conditions

We collected data in parallel with three different triggers for the Forward Spectrometer. The trigger ratio in data taking was managed by the trigger supervisor with a scale-down factor for each trigger.

The first one was the BEAM trigger for a good beam particle. It was defined with

the beam counters as;

$$BEAM = \overline{PRE} \cap BTOT \cap \overline{HOLE}, \tag{3.1}$$

where $\overline{PRE}$ shows that there was no other particle arrived within 500 nsec [38] (pile-up rejection).

The second was the interaction trigger (INT) defined with Bull's Eye counter for an event in which a beam particle interacted with a target particle. Its definition is as follows;

$$INT = BEAM \cap \overline{BE}, \tag{3.2}$$

where $\overline{BE}$ indicates that the measured charge of particle with Bull's Eye counter was lower than a threshold.

The third was FSPEC for an event in which at least one particle entered the Forward Spectrometer. Its definition is as follows;

$$FSPEC = INT \cap FT2 \cap FT3, \tag{3.3}$$

where $FT2(FT3)$ was required to have at least one of all wires on the first and second planes of the FT2(FT3).

3.4 Spectrometer Setting and Kinematic Coverage

We took data with 10 spectrometer angle settings from 6 degrees to 24 degrees in 2-degree step. At each spectrometer angle from 6 degrees to 14 degrees, we took data with two different magnetic settings of FM1 and FM2 namely, 2kG/4kG and 2kG/6kG. And we took data with 2kG/4kG at each angle from 16 degrees to 24 degrees. The polarity was set to bent positive particles away from the beam line. We also took data with 0kG/0kG to calibrate geometry of tracking chambers. Fig. 3.1 and Fig. 3.1 show the kinematic coverage for deuteron and proton, respectively.

3.5 Data set

Table 3.1 shows the summary of data set.

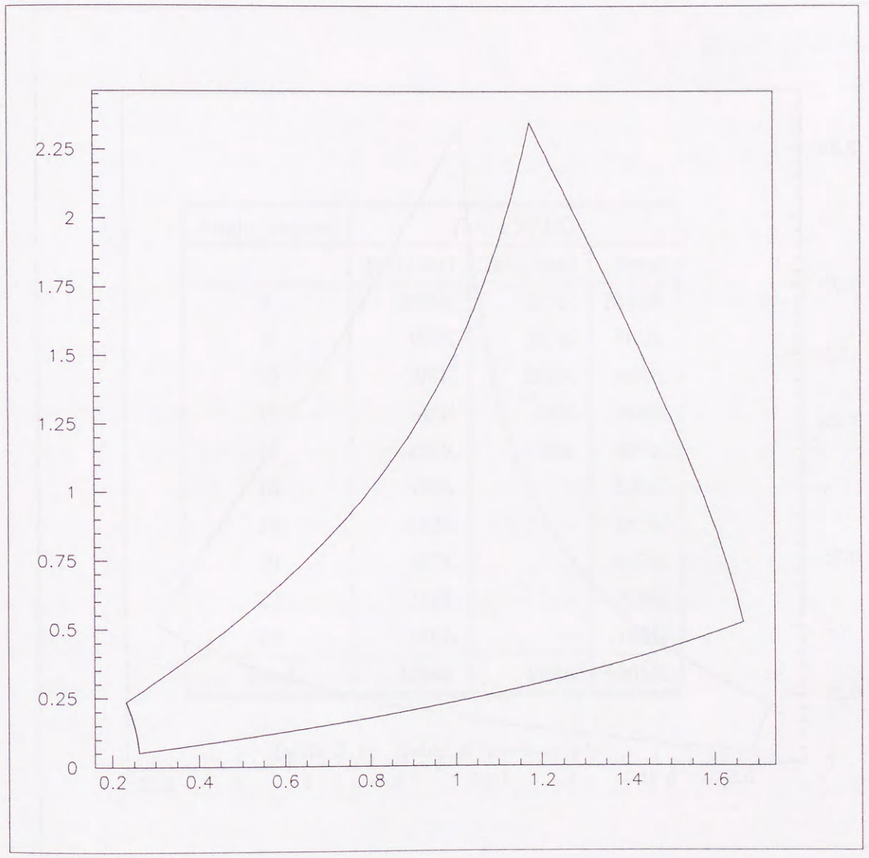

Fig. 3.1: The kinematic coverage for deuteron. The x-axis is rapidity and the y-axis is p_t [GeV/c].

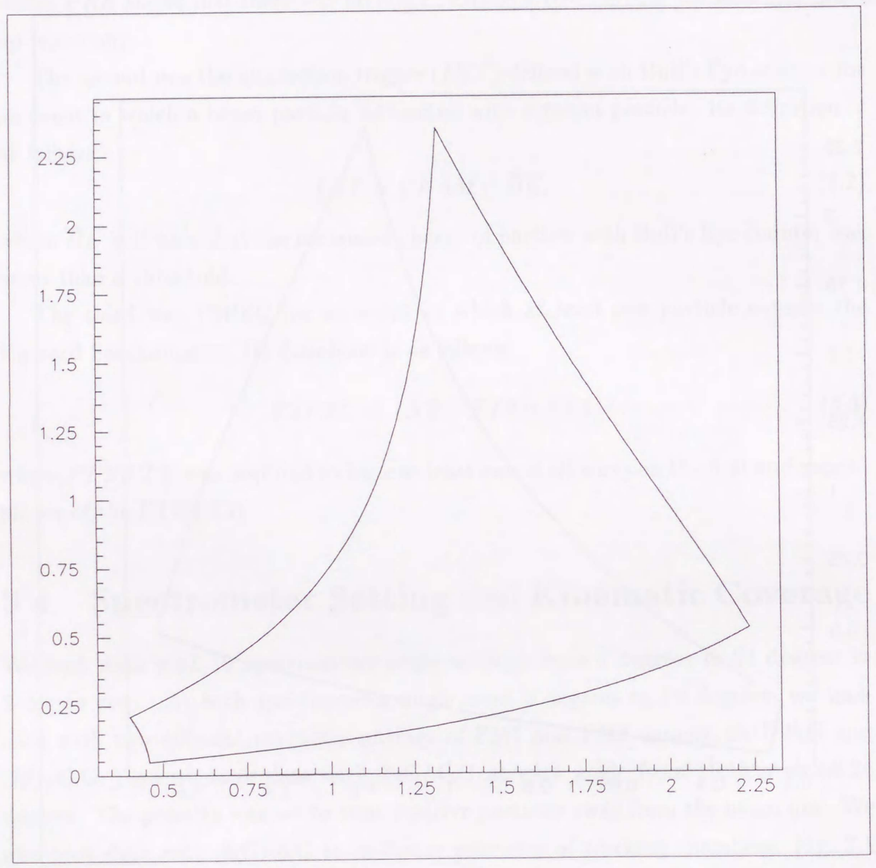

Fig. 3.2: The kinematic coverage for proton. The x-axis is rapidity and the y-axis is p_t [GeV/c].

Angle [degree]	No. FSPEC		
	2kG/4kG	2kG/6kG	Total
6	1039K	377K	1416K
8	355K	207K	562K
10	298K	200K	498K
12	192K	76K	268K
14	427K	70K	497K
16	539K	–	539K
18	642K	–	642K
20	467K	–	467K
22	219K	–	219K
24	186K	–	186K
Total	4364K	903K	5295K

Table 3.1: Table of the data set.

Chapter 4

Detector Analysis

4.1 Calibration

At the beginning of data analysis, two kinds of calibrations are needed. One is geometry calibration among detectors and the other is calibration of the detector components.

4.1.1 Geometry Calibration

The positions of all detectors were surveyed before the run started. The results of the survey were used as primary geometry. The fine geometry of x and y position (see Section. 2.5.1) of each detectors was calibrated using zero-field runs for each angle setting. First, the hits on FT's were found with tracks reconstructed with TPC, then the FT's were adjusted to be straight in the x-direction using FT's x-planes only. The y positions of FT's were adjusted using wire positions of y-plane for FT1 and FT2, and u- or v-planes for FT3 and FT4. Next, the geometry of TPC's at each row was adjusted in the x- and y- directions with the tracks reconstructed with FT's. At last, x position of FTOF wall was adjusted in the x-direction with FTR2 tracks which were reconstructed with the tracking chamber complex downstream of FM2. The y-position of each slat of FTOF wall was also adjusted with the FTR2 tracks (see Section 4.1.4).

4.1.2 FT Calibration

The drift time and the drift length were calibrated with TPC track for each drift chamber. The two parameter were parameterized as following;

$$l(t) = a_1\sqrt{t - t_0} + a_2(t - t_0) + a_3(t - t_0)^2, \tag{4.1}$$

where $l(t)$ is the drift length, t is the TDC value, t_0 is the time-offset, and a_i are calibration constants. The t_0 were calibrated on wire-by-wire for every zero-field run. The calibration constants were calibrated on plane-by-plane only once.

4.1.3 TPC Calibration

The y-position of a track on TPC was given from the time information as

$$y = v(t - t_0), \tag{4.2}$$

where v is the drift velocity of electrons, t is a drift time, t_0 is a time-zero. The v and t_0 were calibrated on row by row at the same time with the geometry calibration. To TPC2, the additional calibration was applied because the hit position shifted due to the drift field distortion and the magnet fringing field.

4.1.4 FTOF Calibration

After track reconstruction and momentum determination (see Section 4.2.4, FTOF calibration was performed. The time of flight, TOF, and y position of a particle, y_{tof}, were calculated from the time and the charge information as follows;

$$TOF = \frac{t_{S_t} + t_{S_b}}{2} - BTOT - t_0, \tag{4.3}$$

$$y_{tof} = \frac{(TDC_b - TDC_t)}{2} \cdot v + y_0, \tag{4.4}$$

$$t_{S_i} = TDC_i \cdot C_i - \frac{S_i}{\sqrt{ADC_i - PED_i}}, \tag{4.5}$$

$$BTOT = \frac{TDC_l \cdot C_l + TDC_r \cdot C_r}{2}, \tag{4.6}$$

where

TDC_i : TDC value
ADC_i : ADC value
PED_i : ADC pedestal [ADC bin]
t_0 : time offset [nsec]
y_0 : y-position offset [mm]
C_i : TDC clock [nsec/TDC bin]
v : propagation velocity of scintillation light [mm/TDC bin]
S_i : slewing correction factor [nsec/ (ADC bin)$^{1/2}$]

and suffices $i = t$ or d denotes a photo-multiplier tube mounded on the top or bottom of the slat of FTOF wall, suffices l or r denotes a photo-multiplier tube mounted on the left or right side of BTOT counter. The y_0 was calibrated with the FS tracks (see Section 4.2.2 for each slat. Then the slewing correction factor was calibrated with $\pi^{\pm}$, roughly identified with squared mass of $-0.2 < m^2 < 0.15$, for each photomultiplier tube. After the calibration of the slewing correction, the t_0's were recalibrated with $\pi^{\pm}$, roughly identified with squared mass of $-0.2 < m^2 < 0.15$. The calibration of the t_0 or y_0 was performed every 4 - 10 runs.

4.2 Track Reconstruction

We developed a track reconstruction code for the Forward Spectrometer, called FAR-eAST [1]. The track reconstruction algorithm is as follows. The tracks were reconstructed independently in each tracking chamber complex. In each tracking chamber complex, initial tracks were formed with the TPC and the tracks were extended to the both upstream and downstream drift chambers. Next, the tracks were associated with the hits of drift chambers, then FTR1/FTR2 tracks were reconstructed. FTR1 and FTR2 tracks were connected at the mid-plane of FM2. If position differences between a FTR1 and a FTR2 are close within 3σ of distribution, their momentum were calculated with a transfer matrix (see Section 4.2.4) and the track was traced back to the target z position through FM1 using the momentum. And the tracks were also extended to the FTOF wall and FTOF hits were searched within a 3σ of the track positions for the association with the tracks.

[1] Forward Arm Reconstruction Algorithm Starting from the TPC's.

4.2.1 TPC track

The start point of the track reconstruction was at the TPC's. Since the drift electrons diffused, a few wires on a row could be fired by a single particle. A cluster was formed from the hits on a row which were close in both of x- and y- directions. Then an array of the clusters on a straight line was searched for the cluster array was fitted to a straight line, as a TPC track. For the reconstruction of TPC tracks, hits on at least 3 rows hits were required.

4.2.2 FTR track

TPC tracks were extended onto adjacent FT's to find hits on the FT's. If one or both of the two wires closest to the track on each plane, was fired, the wire was regarded as associated with the track. Then the track was combined with the wires, and was refitted as a FTR track. The number of planes without hits on the closest wire, missing planes, was required to be at most 4 for FTR track.

4.2.3 Track Matching at Analyzing Magnet

After reconstruction of FTR tracks, they were extended to FM2 and FTR1 and FTR2 were connected at the FM2. The plane m in FM2 was defined as shown in Fig. 4.1, and the track position matchings in the x- and y-directions (Δx and Δy) and the vector matching in y-direction ($\Delta\theta_y$) are defined as follows.

$$\Delta x \equiv x_2 - x_1, \tag{4.7}$$
$$\Delta y \equiv y_2 - y_1, \tag{4.8}$$
$$\Delta\theta_y \equiv \frac{dy_2}{dz_2} - \frac{dy_1}{dz_1}, \tag{4.9}$$

where x_i and y_i denote the x- and y-position of FTRi track projected onto the plane m, and dy_i/dx_i denotes the slope of the track in the y-z plane. The cut criteria of distance between FTR1 and FTR2 track at the matching plane should depend on momentum due to multiple Coulomb scattering. Since the momenta of the tracks were not determined yet at this stage, the cut was set loose as,

$$\Delta x < 5\sigma_{\Delta x}, \tag{4.10}$$
$$\Delta y < 5\sigma_{\Delta y}, \tag{4.11}$$
$$\Delta\theta_y < 5\sigma_{\Delta\frac{dy}{dz}} \tag{4.12}$$

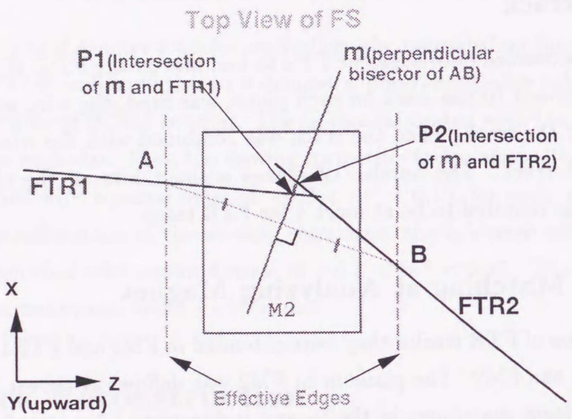

Fig. 4.1: A demonstration of the definition of track matching parameters. Points A, B are intersections of FTR1 and FTR2 with effective edges of FM2. Plane m is the perpendicular bisector of AB. P1 and P2 are intersections of FTR1 and FTR2 with m. Coordinates of P1 and P2 are P1(x_1, y_1), P2(x_2, y_2), where x_i and y_i are defined in Eq. 4.7 and 4.8, respectively.

where Δx and Δy are the distance in x- and y-directions, respectively, and $\Delta dy/dz$ is the angle difference on the y-z plane, and σ denotes the width in r.m.s of their distributions of the deuteron with 0.4 GeV/c, which were determined from the data. The pairs of FTR1 and FTR2 tracks which passed the loose criteria, were left as FS tracks. The widths of their distribution were mainly determined by the multiple Coulomb scattering. The widths were fitted with a function as follows,

$$\sigma_i(\beta p) = \sqrt{a_0 + \frac{a_1}{(\beta p)^2}} \tag{4.13}$$

where i denotes x, y or dy/dz, a0 and a1 are fitting parameters. After momentum determination and TOF association, Eq. 4.10- 4.12 were replaced to refined cuts as follows,

$$\Delta_i < 3\sigma_i(\beta p). \tag{4.14}$$

The widths of the matching were plotted as a function of βp in Fig. 4.2.

4.2.4 Momentum Determination

The momentum calculation of the FS tracks was performed with the field map of FM2 which was measured with the Hall probe. The measured field map was consistent with the other field map calculated with the TOSCA within 1 written as follows,

$$\Delta \mathrm{p} = 0.29979 \cdot q \int \mathbf{B} \times d\mathrm{s}\ [\mathrm{GeV/c}], \tag{4.15}$$

where $q[e]$ is the charge of a particle, $B[T]$ is the magnetic field, s[m] is the path of a particle.

Since B_z is less than a few percent of the main component B_y and the path length in x-direction is less than 15 %, $intB_z dy$ is 3 order smaller than $\int B_y dz$. Then the $B_z dy$ was negligible for the momentum calculation. Therefore, the momentum change in x-direction was written as following from Eq. 4.15.

$$\Delta p_x = 0.29979 \cdot q \int B_y dz\ [\mathrm{GeV/c}]. \tag{4.16}$$

At a point (x_i,y_i), By was integrated along z-axis from entrance effective edge to exit effective edge, and was stored in the field map. We take two points, $\mathrm{x_{inner}}$ and $\mathrm{x_{outer}}$ as shown in Fig. 4.3. The two points are defined as,

$$\mathrm{x_{inner}} = \frac{\mathrm{x_{in}} + \mathrm{x_{close}}}{2}, \tag{4.17}$$

$$\mathrm{x_{outer}} = \frac{\mathrm{x_{close}} + \mathrm{x_{out}}}{2}, \tag{4.18}$$

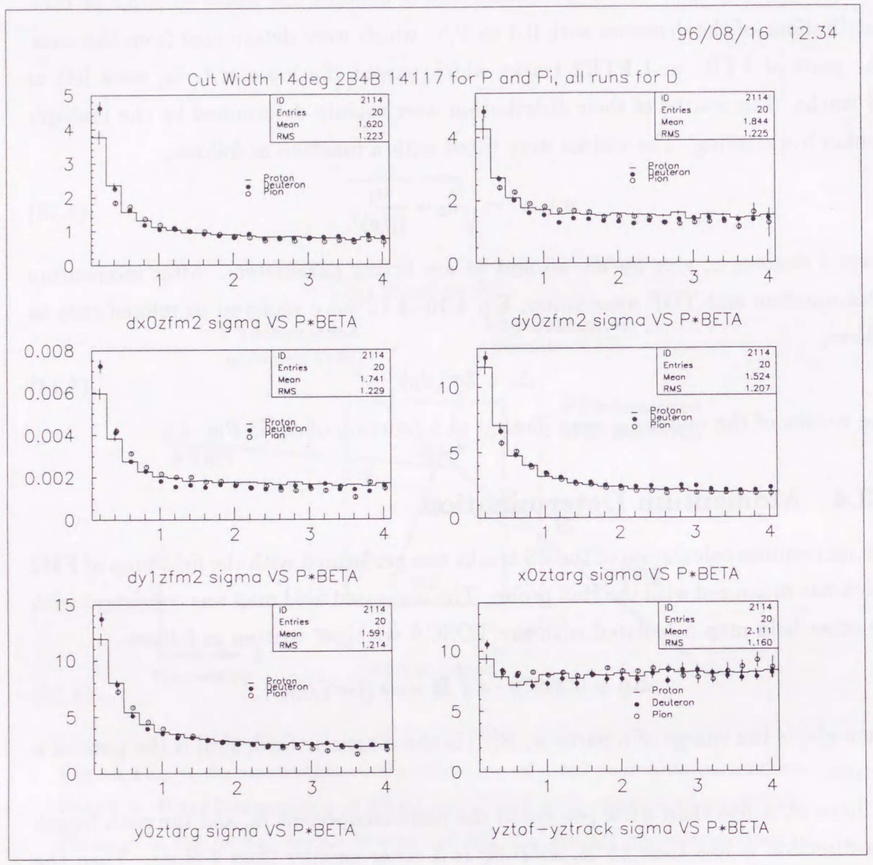

Fig. 4.2: Widths of cut parameters in r.m.s as a function of βp [GeV/c]. Six plots show from the top left figure; widths of track matching in the x-direction [mm] (1st row left), in the y-direction [mm] (1st row right), the track angle matching in the y-direction [rad] (2nd row left), target position in the x-direction [mm] (2nd row right), in the y-direction [mm] (3rd row left), and the FTOF hit residual with respect to the track position in the y-direction [mm] (3rd row right).

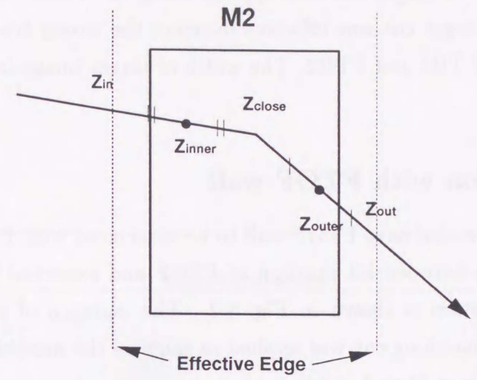

Fig. 4.3: A demonstration of $\int B_y dz$ sampling points for the momentum calculation.

where $\mathbf{x}_{\rm in} = (x_{\rm in}, y_{\rm in}, z_{\rm in})$ is the FTR1 track position at $z_{\rm in}$ (entrance effective edge), $\mathbf{x}_{\rm out} = (x_{\rm out}, y_{\rm out}, z_{\rm out})$is the FTR2 track position at $z_{\rm out}$ (exit effective edge), and $\mathbf{x}_{\rm close}$ is the closest approach point between a pair of FTR1 and FTR2 tracks.

The momentum change in the x-direction is calculated with the average of the two field integration $\int B_y dz$, as

$$\Delta \mathbf{p_x} = \frac{0.29979q(\int Bydz_{(inner)} + \int Bydz_{(outer)})}{2}, \tag{4.19}$$

where $\int Bydz(inner)$ is calculated along z-axis through the point ($\mathrm{x_{inner}}$, $\mathrm{y_{inner}}$), so as $\int Bydz(outer)$. The momentum of the particle was calculated as

$$p = \frac{\Delta p_x}{u_x^2 - u_x^1} \tag{4.20}$$

where u_x^i denotes dx/dz of FTR_i track (i=1,2).

4.2.5 Target Cut

Each FS track was traced back to the target position through FM1 with the determined momentum. The width of the target image in each x- or y-direction also

depended on momentum as those of the matching. The widths were also fitted with Eq. 4.13. Therefore, the target cut was applied using the widths as a function of βp as Eq. 4.14. The target cut was effective to reject the wrong tracks with wrong combination between FTR1 and FTR2. The width of target image in each direction was shown in Fig. 4.2.

4.2.6 Association with FTOF wall

Each FS track was extended onto FTOF wall to be associated with FTOF hits. The width of the distances between hit position of FTOF and expected hit position by FTR2 track in y-direction is shown in Fig. 4.2. The variance of the widths was relatively small. The matching cut was applied as same as the matching cut at FM2 and target cut using Eq. 4.13 and 4.14.

4.3 Particle Identification

Particle identification was performed with squared mass m^2 which was calculated from momentum, time-of-flight and flight-path length as

$$m^2 = p^2\left(\frac{TOF}{L}\right)^2 - 1, \tag{4.21}$$

where p is the momentum, TOF is the time-of-flight, and L is the flight-path length. Fig. 4.4 shows a scatter plot of measured squared mass versus momentum in a 14 degree run.

The resolution of m^2 was determined by the momentum resolution of the tracking system and the time resolution of the time-of-flight system. The momentum resolution σ_p was calculated as

$$\left(\frac{\sigma_p}{p}\right)^2 = (C_{ang}p)^2 + \left(\frac{C_{mult}}{\beta}\right)^2, \tag{4.22}$$

$$C_{ang} = \frac{\sigma_\theta}{\Delta p_x} \tag{4.23}$$

$$C_{mult} = \frac{0.0136z}{\Delta p_x}\sqrt{\frac{x}{X_0}}\left(1 + 0.038ln\frac{x}{X_0}\right), \tag{4.24}$$

$$\Delta p_x = 0.29979\int Bydz, \tag{4.25}$$

where p, β, and z are the momentum [GeV/c], velocity,and the charge of the particle, σ_θ is the intrinsic angular resolution of the tracking system, x/X_0 is the thickness of

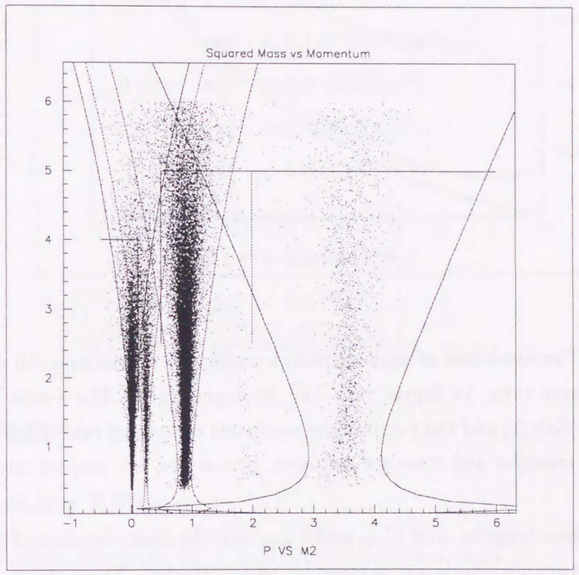

Fig. 4.4: Measured squared mass [GeV^2/c^4](x-axis) versus momentum [GeV/c](y-axis) in a 14 degree run.

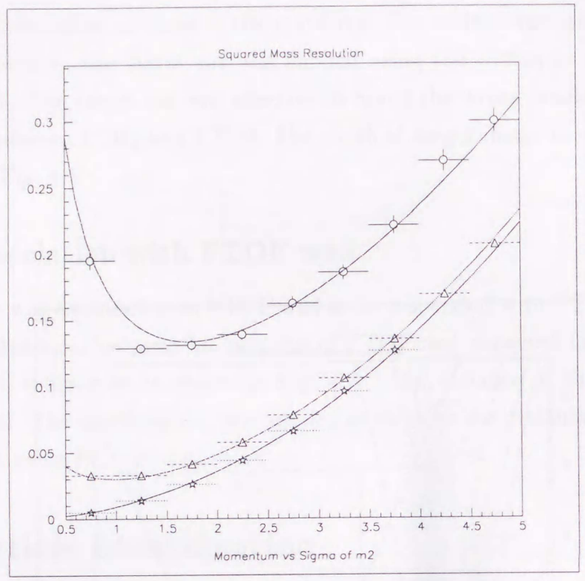

Fig. 4.5: The resolution of squared mass for sum of 8 degree runs, 10 degree runs, 12 degree runs, 14 degree runs and 16 degree runs. The x-axis is the momentum [GeV/c] and the y-axis is the resolution of squared mass [$\mathrm{GeV}^2/\mathrm{c}^4$]. The circles, triangles and stars are deuteron, proton and π^+, respectively.

material in radiation lengths, and C_{ang} and C_{mult} are the contributions of the angular resolution and Multiple Coulomb scattering, respectively. Then the resolution of squared mass σ_{m^2} was written as,

$$\sigma^2_{m^2} = 4m^4\left(\frac{\sigma_p}{p}\right)^2 + \frac{4p^4}{\beta^2}\left(\frac{\sigma_{TOF}}{L}\right)^2 \quad (4.26)$$

$$= 4m^4p^2\cdot C^2_{ang} + 4m^4\left(1+\frac{m^2}{p^2}\right)\cdot C^2_{mult} + 4p^2(m^2+p^2)\cdot C^2_{tof} \quad (4.27)$$

$$C_{tof} = \frac{\sigma_{TOF}}{L}, \quad (4.28)$$

where m is the mass of the particle, σ_{TOF} is the time-of-flight resolution, and L is the flight-path length. Fig. 4.5 shows the width of squared mass as a function of momentum for deuteron, proton and π^+ using the real data. The line in the figure shows the result of fitting to Eq. 4.27.

The fitting results are consistent with the detector resolutions.

The basic boundary of the particle identification was determined using the squared mass resolution as a function of momentum, as follows;

$$|m^2_{measured} - m^2_{real}| < 2.5\sigma_{m^2}, \quad (4.29)$$

where m^2 is the squared mass calculated from the measured momentum and the measured time-of-flight, m_{real} is the real mass of the particle species. And additional particle identification boundary for π, K, p and d were following,

$$m^2_\pi < 0.125\ [\mathrm{GeV}^2/\mathrm{c}^4], \quad (4.30)$$

$$0.18 < m^2_K < 0.5\ [\mathrm{GeV}^2/\mathrm{c}^4], \quad (4.31)$$

$$0.5 < m^2_p < 2.0\ [\mathrm{GeV}^2/\mathrm{c}^4], \quad (4.32)$$

$$2.0 < m^2_d < 6.0\ [\mathrm{GeV}^2/\mathrm{c}^4], \quad (4.33)$$

$$0.45 < p_\pi < 4.0\ [\mathrm{GeV/c}], \quad (4.34)$$

$$0.45 < p_K < 3.0\ [\mathrm{GeV/c}], \quad (4.35)$$

$$0.45 < p_p < 5.0\ [\mathrm{GeV/c}], \quad (4.36)$$

$$0.5 < p_d < 5.0\ [\mathrm{GeV/c}]. \quad (4.37)$$

4.4 Corrections

4.4.1 Tracking Efficiency

Track reconstruction efficiency, ϵ_{track} was divided to three parts as,

$$\epsilon_{track} = \epsilon_{FT}\cdot\epsilon_{TPC}\cdot\epsilon_{soft} \quad (4.38)$$

where

ϵ_{FT} : FT hardware efficiency
ϵ_{TPC} : TPC hardware efficiency
ϵ_{soft} : track reconstruction software efficiency.

FT hardware efficiency was regarded as 100 % because the efficiency per plane of FT's was higher than 95 %. FT1 and FT2 were required to have hits at least 6 out of 10 planes. FT3 and FT4 were required to have hits at least 4 out of 8 planes. Therefore ϵ_{FT} was almost equal to 100 %. TPC hardware efficiency and the track reconstruction software efficiency are described later.

TPC Hardware Efficiency

TPC hardware efficiency depends on the position of the hits and the momentum of the particle. The position dependence in x-direction of the TPC hardware efficiency was due to field distortion. The y-position dependence of the efficiency was regarded as due to electron diffusion and absorption during drift. The momentum dependence of the efficiency was due to the change of energy deposit of the particle in TPC, dE/dx. Thus the momentum dependence of the efficiency was estimated as a function of $\beta\gamma$, where $\beta = v/c$, and $\gamma = 1/\sqrt{1-\beta^2}$. The TPC hardware efficiency per row was written as;

$$\epsilon_{TPC_{r,x,y}}(\beta\gamma) = 1 - A_{r,x,y} \cdot Ineff(\beta\gamma), \tag{4.39}$$

where suffices r, x and y denote the row number of the TPC, hit position in x-direction and y-direction at each row, respectively, A is the normalization factor indicating the degree of inefficiency, and $Ineff(\beta\gamma)$ is TPC hardware inefficiency averaged over row and hit position. The TPC inefficiency of row i, $Ineff_i$ was calculated as follows;

$$Ineff_i = 1 - \epsilon_{TPC_i}, \tag{4.40}$$

$$\epsilon_{TPC_i} = \frac{\text{No. of tracks with hits on all row } i}{\text{No. of tracks with hits on all rows except row } i}. \tag{4.41}$$

Fig. 4.6 and Fig. 4.7 show the averaged inefficiency as a function of $\beta\gamma$ of TPC1 and TPC2, respectively. Then line shows the fitting functions. While the the inefficiency averaged by $\beta\gamma$ was written using normalization factor of each row, x and y, $A_{r,x,y}$, and inefficiency averaged by row and hit position as,

$$Ineff_{r,x,y} = \frac{\int A_{r,x,y} \cdot Ineff(\beta\gamma) \cdot N_{r,x,y}(\beta\gamma)}{\int N_{r,x,y}(\beta\gamma)} \tag{4.42}$$

where N denotes the number of tracks with hits on all the rows except row r. From Eq , $A_{r,x,y}$ was written as,

$$A_{r,x,y} = \frac{Ineff_{r,x,y} \cdot \int N_{r,x,y}(\beta\gamma)}{\int Ineff(\beta\gamma) \cdot N_{r,x,y}}. \tag{4.43}$$

The TPC hardware efficiency was calculated track by track with $\epsilon_{TPC_{r,x,y}}$ of the hit position as,

$$\epsilon_{TPC} = \epsilon_{TPC^0} + \epsilon_{TPC^1} + \epsilon_{TPC^2} + \epsilon_{TPC^3}, \tag{4.44}$$

where

$$\epsilon_{TPC^0} = \epsilon_1 \cdot \epsilon_2 \cdot \epsilon_3 \cdot \epsilon_4 \cdot \epsilon_5 \cdot \epsilon_6 \tag{4.45}$$

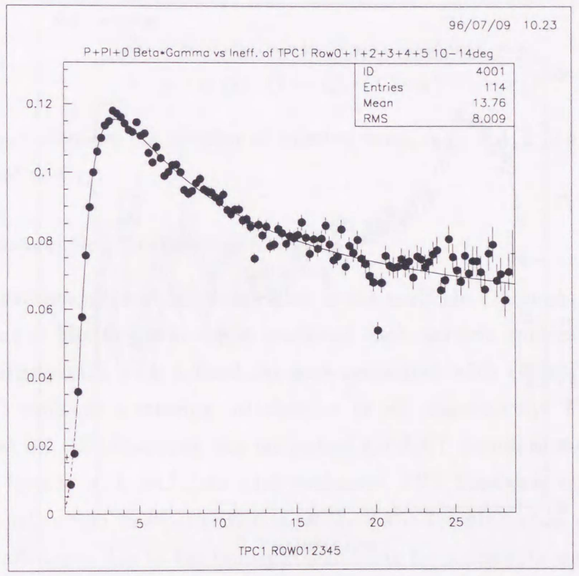

Fig. 4.6: The TPC1 inefficiency(y-axis) as a function of $\beta\gamma$(x-axis) with the fitting functions for deuterons, protons and π^+'s.

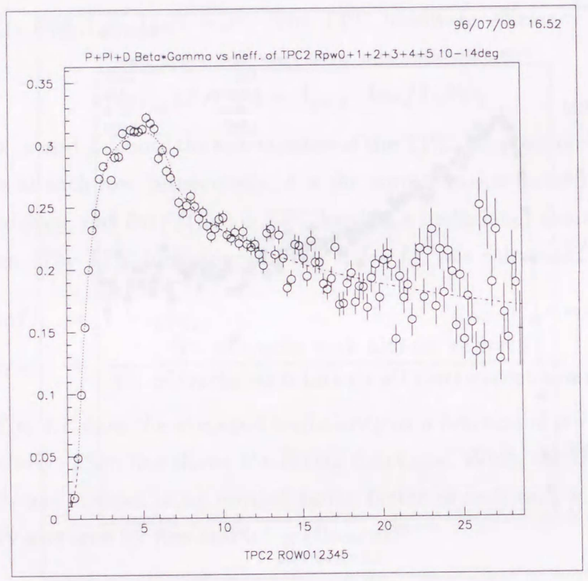

Fig. 4.7: The TPC2 inefficiency(y-axis) as a function of $\beta\gamma$(x-axis) with the fitting functions for deuterons, protons and π^+'s.

$$\begin{aligned}
\epsilon_{TPC^1} &= (1-\epsilon_1)\cdot\epsilon_2\cdot\epsilon_3\cdot\epsilon_4\cdot\epsilon_5\cdot\epsilon_6 \\
&+ \cdots \\
&+ \epsilon_1\cdot\epsilon_2\cdot\epsilon_3\cdot\epsilon_4\cdot\epsilon_5\cdot(1-\epsilon_6) \qquad (4.46)\\
\epsilon_{TPC^2} &= (1-\epsilon_1)\cdot(1-\epsilon_2)\cdot\epsilon_3\cdot\epsilon_4\cdot\epsilon_5\cdot\epsilon_6 \\
&+ \cdots \\
&+ \epsilon_1\cdot\epsilon_2\cdot\epsilon_3\cdot\epsilon_4\cdot(1-\epsilon_5)\cdot(1-\epsilon_6) \qquad (4.47)\\
\epsilon_{TPC^3} &= (1-\epsilon_1)\cdot(1-\epsilon_2)\cdot(1-\epsilon_3)\cdot\epsilon_4\cdot\epsilon_5\cdot\epsilon_6 \\
&+ \cdots \\
&+ \epsilon_1\cdot\epsilon_2\cdot\epsilon_3\cdot(1-\epsilon_4)\cdot(1-\epsilon_5)\cdot(1-\epsilon_6) \qquad (4.48)
\end{aligned}$$

where n of ϵ_{TPC^n} denotes the number of missing rows, ϵ_i $(1 = 1, 2, 3, 4, 5, 6)$, denotes the efficiency at row i.

Track Reconstruction Software Efficiency

Track reconstruction software efficiency due to the multiple Coulomb scattering was evaluated using a Monte Carlo single tracks of each particle species. A thousand events with single track with a fixed βp were generated with GEANT [40] simulation code with multiple scattering switched on or off, respectively. The energy loss was always set on. Furthermore the output of GEANT simulation was converted to same data format with real data with evaluated TPC hardware efficiency. Then the track reconstruction was performed with the same tracking code with real data. The software efficiency due to the multiple scattering for a fixed βp was evaluated as follows;

$$\epsilon_{soft} = \frac{\text{No. of reconstructed tracks of events with multi. scattering on}}{\text{No. of reconstructed tracks of events with multi. scattering off}} \qquad (4.49)$$

In the GEANT simulation, Forward Spectrometer was set at 6 degree and the magnetic strength were set to 2 kGauss and 4 kGauss for FM1 and FM2, respectively. The magnetic field was set to bent positive particles away from the beam line. Then the single tracks of deuteron, proton or positive pion were generated with a fixed emission angle with theta of 6.5 deg. and phi of 180 deg. with each βp from 0.2 to 5 GeV/c. The efficiency is parameterized as,

$$\epsilon_{soft} = a_0 + a_1 log(\beta p), \qquad (4.50)$$

where a_0 and a_1 are fitting parameters. Fig. 4.8 shows the track reconstruction

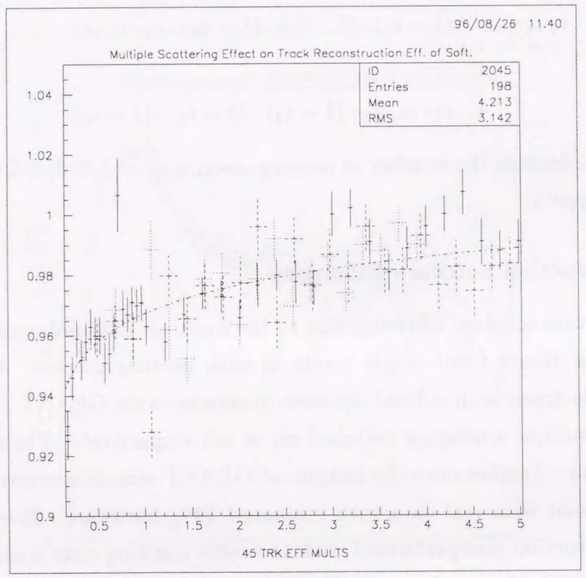

Fig. 4.8: The software efficiency(y-axis) due to the multiple scattering as a function of βp [GeV/c](x-axis) with the fitting functions for deuterons, protons and π^+'s. The solid cross, the dot cross and the dash cross are deuteron, proton and π^+, respectively.

software efficiency due to the multiple scattering as a function of βp. The dash line is the fitting function. The fitting parameters, a_0 and a_1 are 0.967 and 0.0306, respectively. The efficiency goes down as the βp decreasing, from 99 % to 94 %.

In previous analysis by Sako [41], the track multiplicity dependence of the track reconstruction software efficiency is obtained. Fig. 4.9 [41] shows the track reconstruction efficiency as a function of βp for multiplicities 1 (solid), 5 (dashed) and 9 (dotted). The efficiency decreases as the multiplicity increases at momentum higher than 2 GeV/c, while it is stable at momentum less than 2 GeV/c. Then Fig. 4.9 [41] shows the average number of tracks as a function of spectrometer angle. The number of tracks in the inclusive events is less than 2. Thus, the track multiplicity dependence of the software efficiency is small. However the definition of the central events is different; the central events in Fig. 4.10 is central 10 % while that in this thesis is central 6 % (see Section 5.1.3), the number of tracks in the central events is expected to be less than 3 because our analysis does not include the data at the most forward spectrometer angle of 6 deg. for the central events. Therefore, the correction of the track multiplicity dependence of the track reconstruction software efficiency is not applied in this analysis, then the ambiguity of the track reconstruction software efficiency, less than 5 % is put into the systematic errors.

4.4.2 Time-of-Flight Wall Occupancy

Since the TDC of FTOF did not have multiple hit capability, even if a slat had two or more hits, only first hit could be recorded. The occupancy causes inefficiency for slow particles. The inefficiency was evaluated for each forward spectrometer setting and trigger type as,

$$\epsilon_{TOF_i} = 1 - P_i(t), \tag{4.51}$$

$$P_i(t) = \frac{\int n(t)dt}{N_i} \cdot \frac{N_i}{N} = \frac{\int n(t)dt}{N} \tag{4.52}$$

where $P_i(t)$ is a probability that the slat, i had been hit by another particle by the time t, $n(t)$ is the number of hits on a slat at time t, N_i is the total number of hits on a slat i, N is the total number of hits on FTOF wall. Fig. 4.11 shows FTOF occupancy.

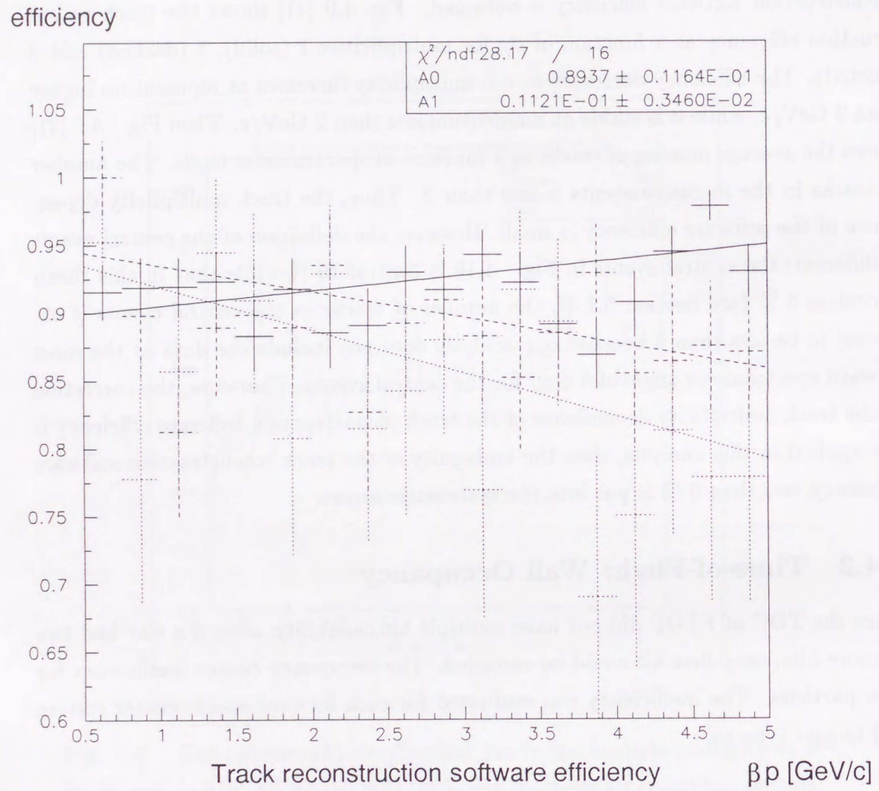

Fig. 4.9: Track reconstruction efficiency of anti-protons as a function of βp [GeV/c] for reconstructed track multiplicities of 1 (solid), 5 (dashed), and 9 (dotted) [41]. The efficiency at high βp decreases as the multiplicity increases.

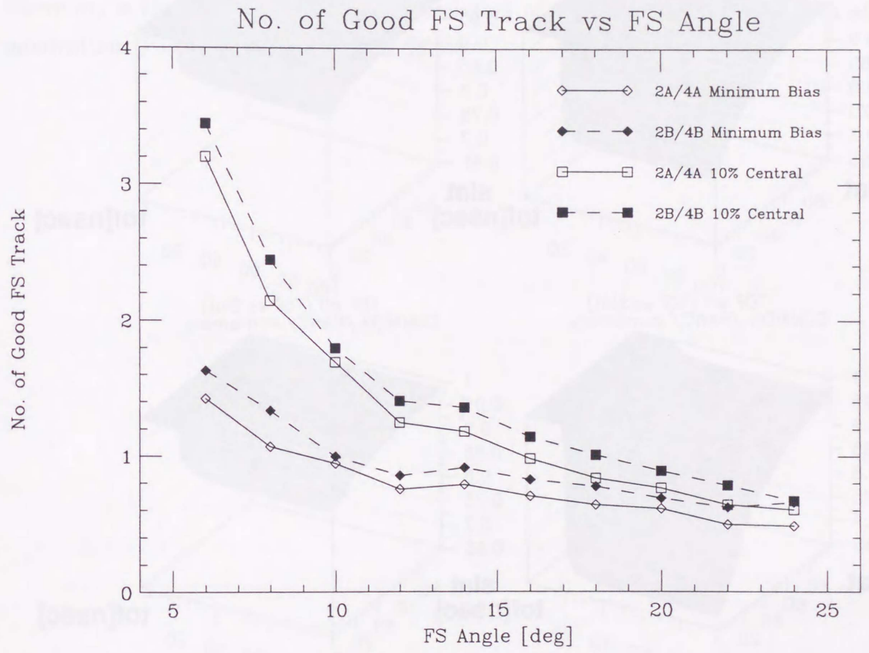

Fig. 4.10: The numbers of good FS tracks as a function of the FS angle [degree] for 2A/4A and 2B/4B settings in minimum bias events and in 10 % central events [41].

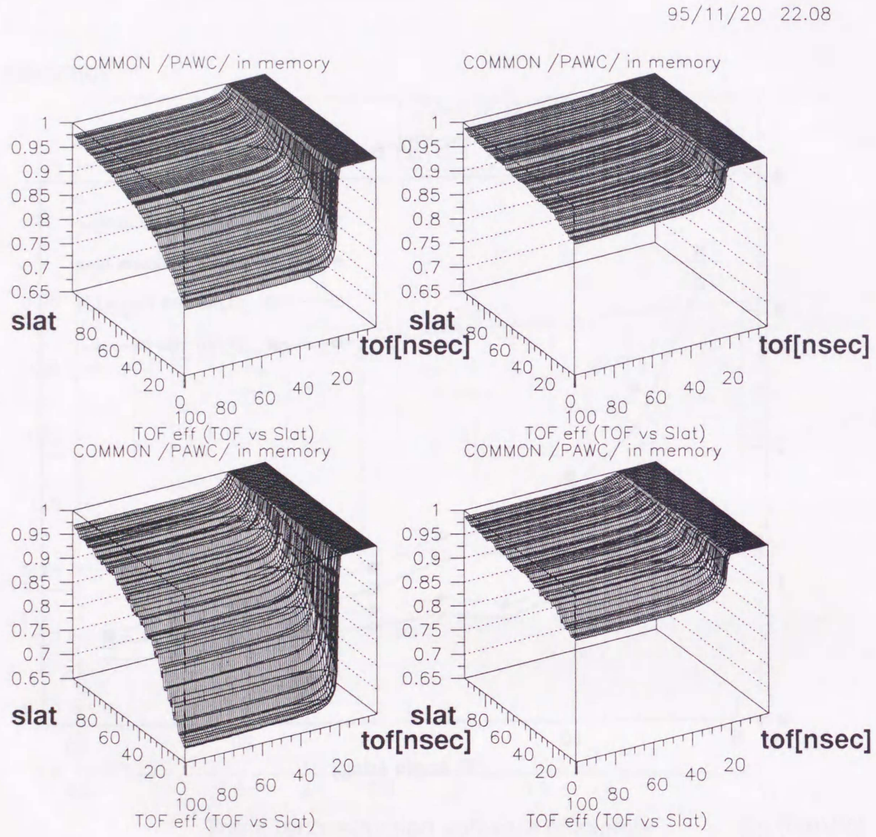

Fig. 4.11: FTOF detection efficiency as a function of the slat number (the left-side axis) and a time-of-flight in nsec (the right-side axis). Four plots correspond to $FSPEC$ events at 6 degrees (top left), at 24 degrees (top right), 6 % central events at 6 degrees (bottom left), and at 24 degrees (bottom right).

4.4.3 Particle Identification Efficiency

Since the 2.5 σ cut in m^2 from the data was used as the particle identification cut, its efficiency was evaluated using a Gaussian approximation as

$$\epsilon_{PID} = \int_{m^2_{\rm min}}^{m^2_{\rm max}} \frac{1}{\sqrt{2\pi}\sigma_{m^2}} exp\left(-\frac{(m^2 - m_0^2)^2}{2\sigma_{m^2}}\right) dm^2, \qquad (4.53)$$

where m_0 is the real mass, σ_{m^2} is the resolution of squared mass as a function of momentum. The efficiency is basically 98.8%.

Chapter 5

Experimental Results

5.1 Cross Section Evaluation

5.1.1 Trigger Cross Section

The trigger cross section σ_{trig} of the interaction (INT) trigger was evaluated with Au target run and empty target run as

$$\sigma_{trig} \equiv \left(\frac{S_{trig} N_{trig}}{N_{beam}} - \frac{S^{MT}_{trig} N^{MT}_{trig}}{N^{MT}_{beam}} \right) \frac{10^{24} A}{N_A D} \text{ [barn]}, \tag{5.1}$$

where N_{beam} is the number of beam triggers, N_{trig} is the number of the INT triggers, S_{trig} is scale-down factor of INT trigger, A is the mass number of the target nuclei [amu], N_A is Avogadro's number = 6.02×10^{23} [mol^{-1}], D is the target thickness [g/cm^2]. Suffice MT denotes target was empty. σ_{trig} was plotted as function of run number in Fig. 5.1 [41]. The mean value of σ_{trig} is 5.25 barn and stable within 10 %. The mean value corresponds to the geometrical cross section σ_geom of Au+Au collisions with $R_0 = 1.11$ calculated as

$$\sigma_{geom} = \pi (2 \cdot^3 \sqrt{197} \cdot R_0)^2. \tag{5.2}$$

5.1.2 Invariant Cross Sections

The Lorentz invariant cross section of particle production is written as,

$$E \frac{d^3\sigma}{dp^3} = \frac{d^3\sigma}{p_t dp_t dy d\phi} = \frac{d^3\sigma}{m_t dm_t dy d\phi}, \tag{5.3}$$

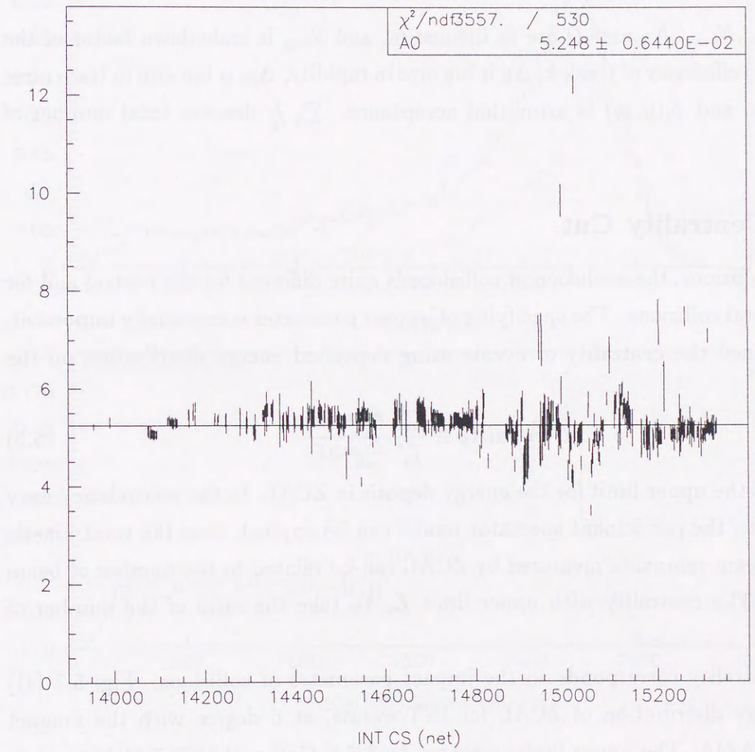

Fig. 5.1: *INT* cross sections [barn] as a function of the run numbers, the solid line is the fit with the value of 5.25 barn [41].

where p_t is transverse momentum, $m_t(=\sqrt{p_t^2+m_0^2})$ is transverse mass, m_0 is the real mass, p is momentum, E is total energy, y is rapidity, and ϕ is azimuthal angle. The invariant cross section was evaluated at each bin of rapidity and transverse momentum, as

$$E\frac{d^3\sigma}{dp^3} = \frac{S_{trig}\sum_k \frac{1}{\epsilon_k}}{N_{beam}} \cdot \frac{10^{24}A}{N_A D} \cdot \frac{1}{p_t \Delta y \Delta p_t \Delta\phi_i(y,p_t)} \,[\text{barn}\cdot\text{GeV}^{-2}\text{c}^3], \qquad (5.4)$$

where S_{beam},N_{beam},N_A,and D are as defined in, and S_{trig} is scale-down factor of the trigger, ϵ_k is efficiency of track k, Δy is bin size in rapidity, Δp_t is bin size in transverse momentum, and $\phi_i(y,p_t)$ is azimuthal acceptance. $\sum_k \frac{1}{\epsilon_k}$ denotes total number of particle.

5.1.3 Centrality Cut

In heavy collisions, the evolution of collisions is quite different for the central and for the peripheral collisions. The specifying of impact parameter is essentially important.

We defined the centrality of events using deposited energy distribution on the ZCAL, as

$$Centrality \equiv \frac{\int_0^{E_c} \frac{dN_{int}}{dE} dE}{\int_0^{\infty} \frac{dN_{int}}{dE} dE} \qquad (5.5)$$

where E_c is the upper limit for the energy deposit in ZCAL. In the relativistic heavy ion collisions, the participant spectator model can be applied, then the total kinetic energy of beam remnants measured by ZCAL can be related to the number of beam remnants. The centrality with upper limit E_c To take the ratio of the number of event

The centrality corresponds to the impact parameter of collisions. Fig. 5.2 [41] shows energy distribution of ZCAL for INT events, at 6 degree with the magnet setting of 2A/4A. The upper limits were set to 325.6 GeV and 1679.7 GeV so as to adjust the trigger cross section to be 0.32 barn and 2.62 barn for the centrality 6 % and 50 %, respectively, corresponding to 6 % and 50 %, or the impact parameter less than 3.2 fm and 9.1 fm, respectively. The peak of ZCAL energies were plotted as function of the run number in Fig. Fig shows the peak of ZCAL energy fluctuated around 2066 GeV within $\sim$ 2 %.

We defined here two types of trigger, central and peripheral as centrality 0 $\sim$ 6 % and 50 $\sim$ 100 %, respectively.

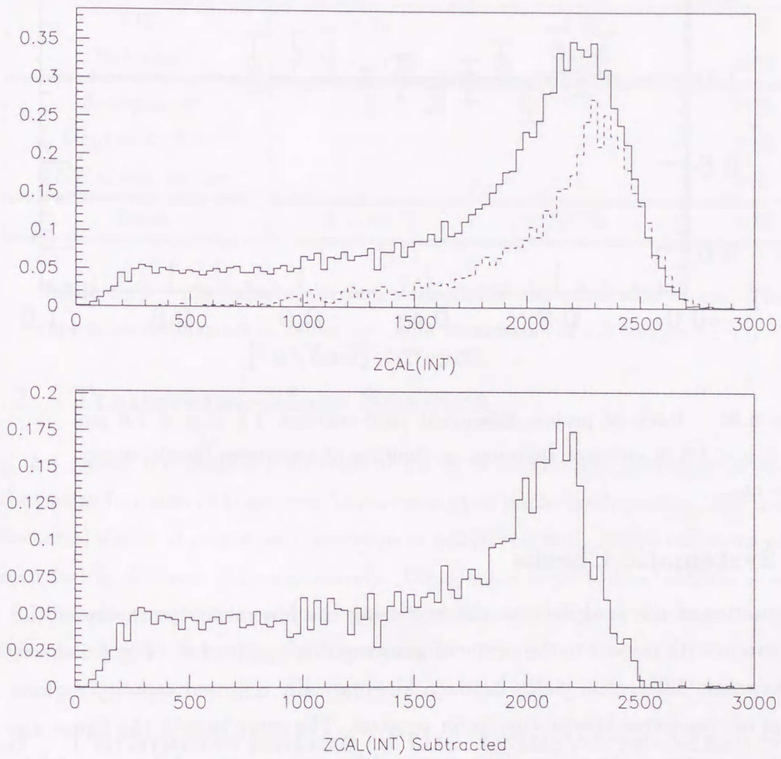

Fig. 5.2: ZCAL spectra [GeV] for *INT* events, for 6-degree with the Au target (top figure, solid line) and for 6-degree without the target(top figure, dashed line), normalized with *BEAM* counts [41]. The net ZCAL spectrum obtained by subtracting the two spectra (bottom figure).

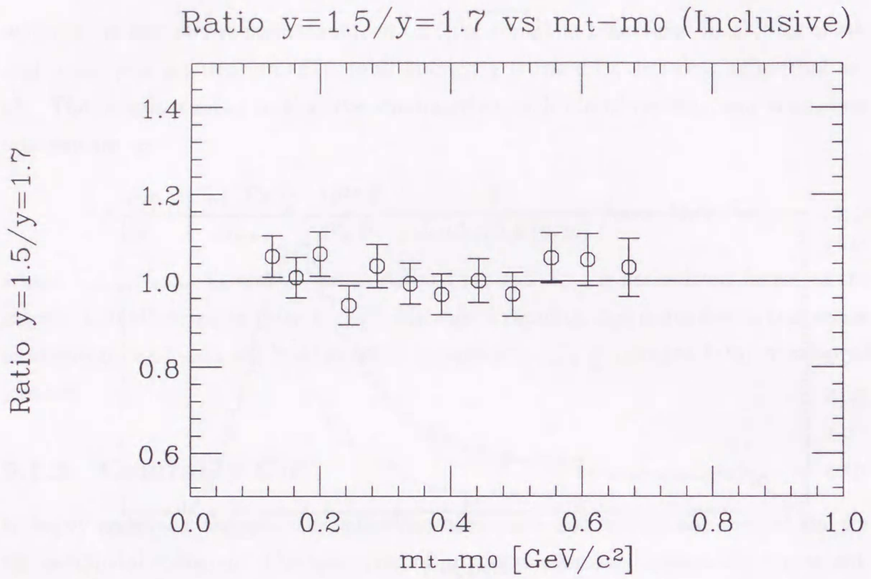

Fig. 5.3: Ratio of proton differential yield between $1.4 < y < 1.6$ and $1.6 < y < 1.8$ in inclusive collisions, as function of transverse kinetic energy, $m_t - m_0$.

5.1.4 Systematic Checks

The systematics of the analysis was checked using the kinematic symmetry of the collision system with respect to the center of mass rapidity $y_{c.m.}(\simeq 1.6)$. Fig. 5.3 shows ratio of invariant differential yields between kinematically reflected rapidity regions as function of transverse kinetic energy for protons. The error bars in the figure are the statistical errors of the ratios. The proton differential yield in $1.4 < y < 1.6$ is consistent to that in $1.6 < y < 1.8$ within 7 %. It is considered as a systematic error originating from the geometrical acceptance calculation.

5.1.5 Summary of Systematic Errors

The applied corrections and the systematic errors in the analysis are summarized in Table . The overall systematic error of the invariant cross sections was estimated to be 8 %.

	Correction Range	Typical Correction Inclusive	Sys. Error
TPC Hardware Eff.	0 – 7 %	2 %	1 %
Track Recon. Soft. Eff.	1 – 7 %	2 %	5 %
FTOF Detection Eff.	0 – 30 %	7 %	2 %
PID	1 %	1 %	1 %
Subtotal	1 – 40 %	12 %	6 %
Acceptance	–	–	5 %
Centrality Cut	–	–	2 %
INT Cross Section	–	–	3 %
Total	1 – 40 %	12 %	8 %

Table 5.1: The table of correction amplitude and systematic errors. The typical corrections are at 14 degrees, with momentum of 2.5 GeV/c.

5.2 Transverse-Mass Spectra

Fig. 5.4 shows the invariant differential yields of proton and deuteron in inclusive collisions as function of transverse kinetic energy at each rapidity-slice. The invariant differential yields of proton and deuteron in peripheral and central collisions are also shown in Fig. 5.5 and 5.6, respectively. The spectra in peripheral collisions seem to be in a single exponential, and the spectra in central collisions also seem to be in a single exponential except for the low m_t region.

5.3 Parameterization of the Transverse-Mass Spectra

The differential cross sections are generally represented as function of transverse kinetic energy $(m_t - m_0)$ [42, 43, 44, 45] because it is empirically known that production cross sections of secondary particles in $p+p$, $p+A$, and $A+A$ collisions are described well with a single exponential function of transverse kinetic energy, as

$$\frac{d\sigma^2}{2\pi m_t dm_t dy} = A_0 exp\left(-\frac{m_t - m_0}{T_0}\right), \tag{5.6}$$

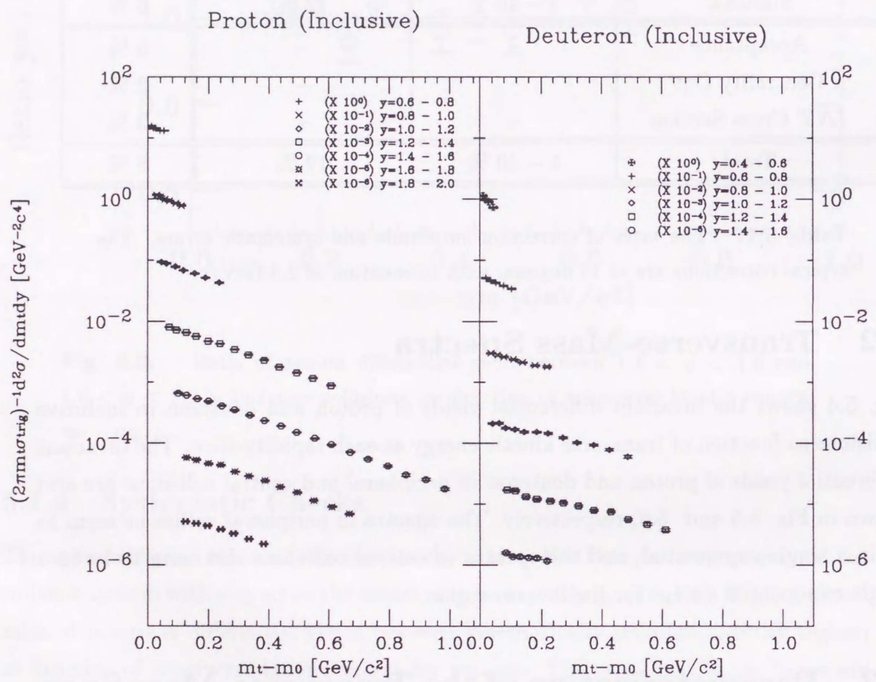

Fig. 5.4: The invariant differential yield of proton(left) and deuteron(right) in minimum-bias collisions, as function of transverse kinetic energy, $m_t - m_0$.

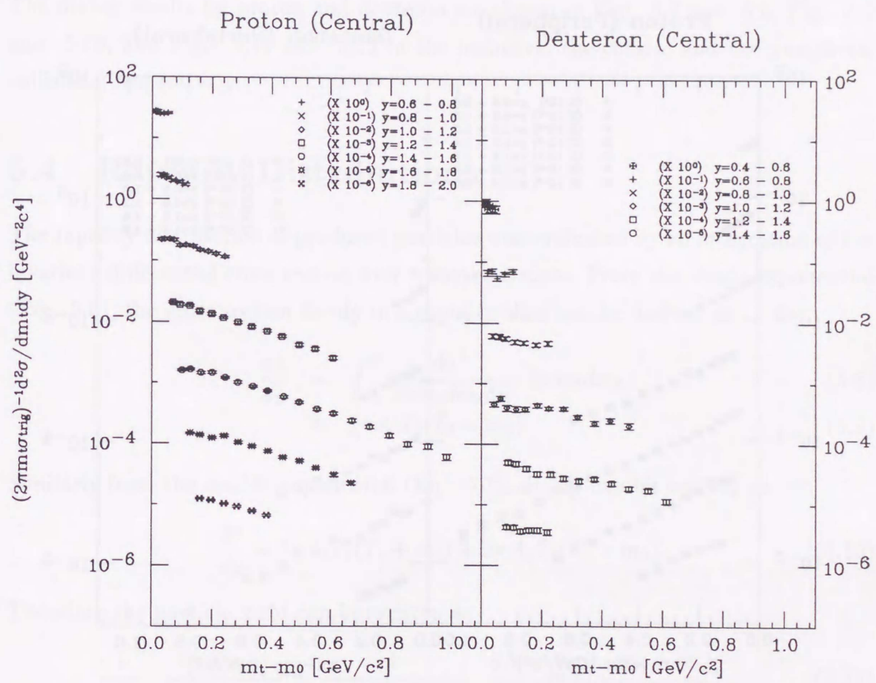

Fig. 5.5: The invariant differential yield of proton(left) and deuteron(right) in central collisions, as function of transverse kinetic energy, $m_t - m_0$.

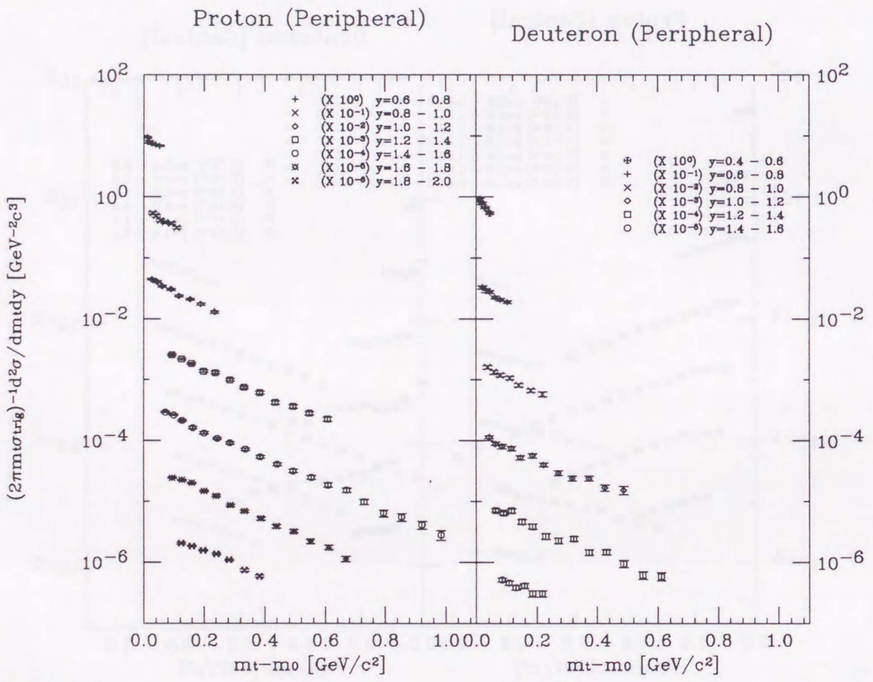

Fig. 5.6: The invariant differential yield of proton(left) and deuteron(right) in peripheral collisions, as function of transverse kinetic energy, $m_t - m_0$.

where T_0 is called the inverse slope parameter and A_0 is a normalization factor. But the single exponential function was not suitable to describe the results, especially for low m_t region in central collision. To describe those spectra, a double exponential function was used, as

$$\frac{d\sigma^2}{2\pi m_t dm_t dy} = A_1 exp\left(-\frac{m_t - m_0}{T_1}\right) + A_2 exp\left(-\frac{m_t - m_0}{T_2}\right). \tag{5.7}$$

The fitting results for proton and deuteron are shown in Fig. 5.7 and 5.8, Fig. 5.9 and 5.10, and Fig. 5.11 and 5.12 in the inclusive, the central and the peripheral collisions, respectively.

5.4 Rapidity Distributions

The rapidity distribution of produced particles was evaluated by an integration of the invariant differential cross section over transverse mass. From the single exponential (Eq. 5.6), the cross section $d\sigma/dy$ in a rapidity slice can be derived as

$$\frac{d\sigma}{dy} = \int_{m_0}^{\infty} \frac{d\sigma^2}{2\pi m_t dm_t dy} \cdot 2\pi m_t dm_t \tag{5.8}$$

$$= 2\pi A_0 T_0 (T_0 + m_0). \tag{5.9}$$

Similarly from the double-exponential (Eq. 5.7), $d\sigma/dy$ can be written as

$$\frac{d\sigma}{dy} = 2\pi A_1 T_1 (T_1 + m_0) + 2\pi A_2 T_2 (T_2 + m_0). \tag{5.10}$$

Therefore the particle yield can be written as

$$\frac{1}{\sigma_{trig}} \cdot \frac{d^2\sigma}{2\pi m_t dm_t dy} = \frac{1}{2\pi T_0 (T_0 + m_0)} \cdot \frac{dN}{dy} \cdot \exp\left(-\frac{m_t - m_0}{T_0}\right) \tag{5.11}$$

assuming the single exponential or

$$\frac{1}{\sigma_{trig}} \cdot \frac{d^2\sigma}{2\pi m_t dm_t dy} =$$

$$\frac{1}{2\pi T_1 (T_1 + m_0)} \cdot \frac{1}{1+w} \cdot \frac{dN}{dy} \cdot \exp\left(-\frac{m_t - m_0}{T_1}\right)$$

$$\frac{1}{2\pi T_2 (T_2 + m_0)} \cdot \frac{w}{1+w} \cdot \frac{dN}{dy} \cdot \exp\left(-\frac{m_t - m_0}{T_2}\right) \tag{5.12}$$

$$w = \frac{A_2 T_2 (T_2 + m_0)}{A_1 T_1 (T_1 + m_0)}. \tag{5.13}$$

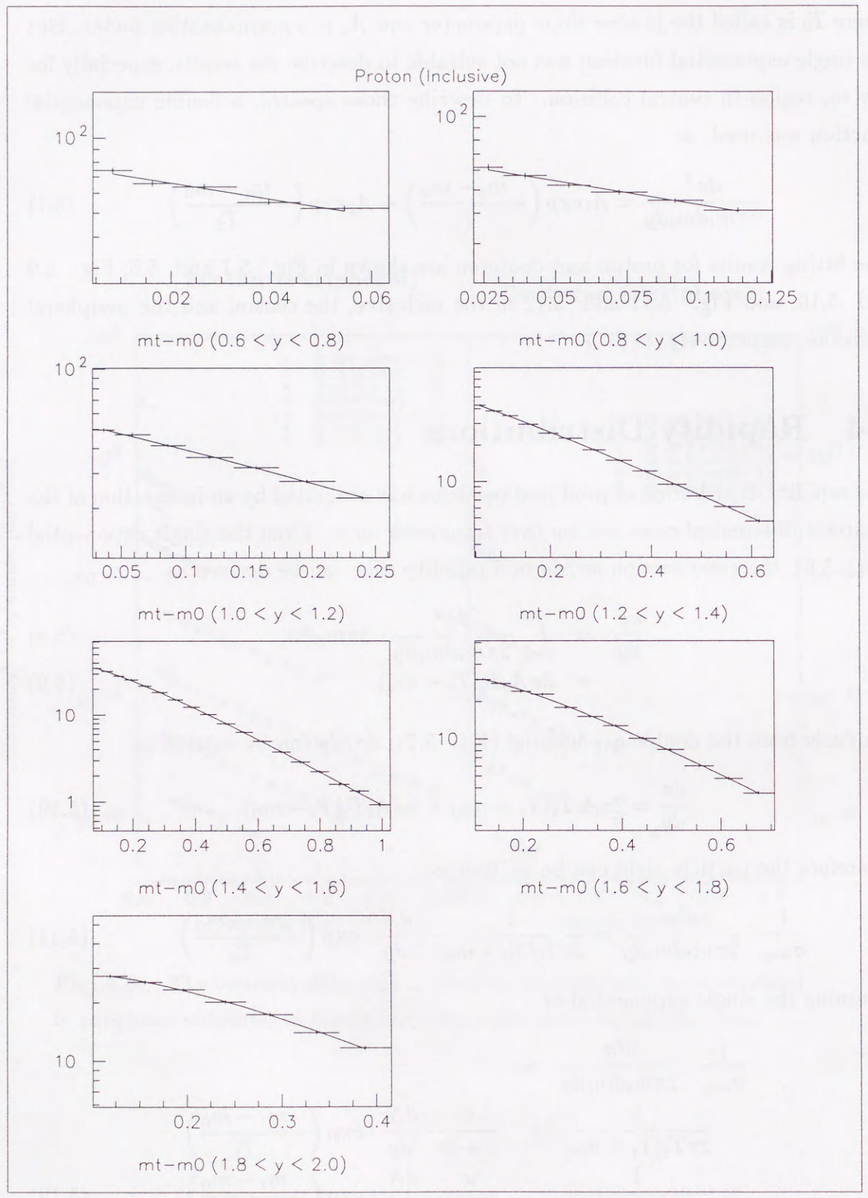

Fig. 5.7: Proton fitting in inclusive collisions. The x-axis is $m_t - m_0$ [GeV/c^2] and the y-axis is invariant differential cross section [barn GeV^{-2}c^4].

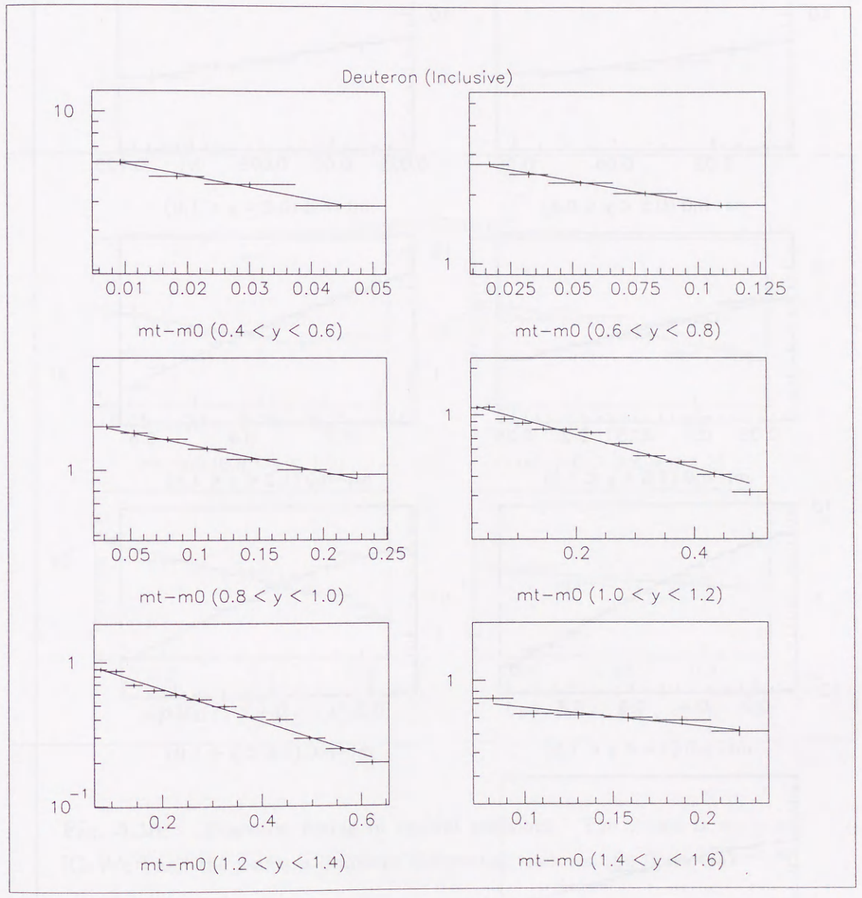

Fig. 5.8: Deuteron fitting in inclusive collisions. The x-axis is $m_t - m_0$ [GeV/c^2] and the y-axis is invariant differential cross section [barn GeV^{-2}c^4].

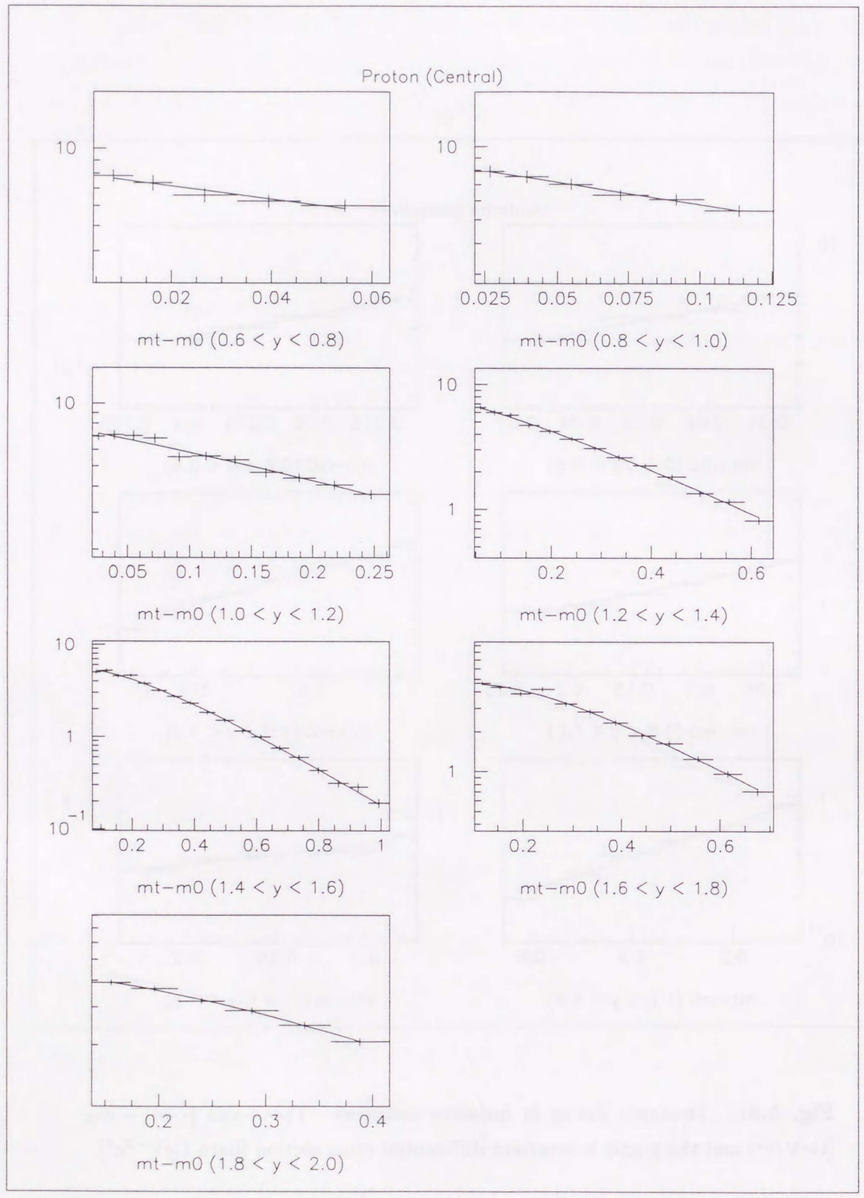

Fig. 5.9: Proton fitting in central collisions. The x-axis is $m_t - m_0$ [GeV/c^2] and the y-axis is invariant differential cross section [barn GeV^{-2}c^4].

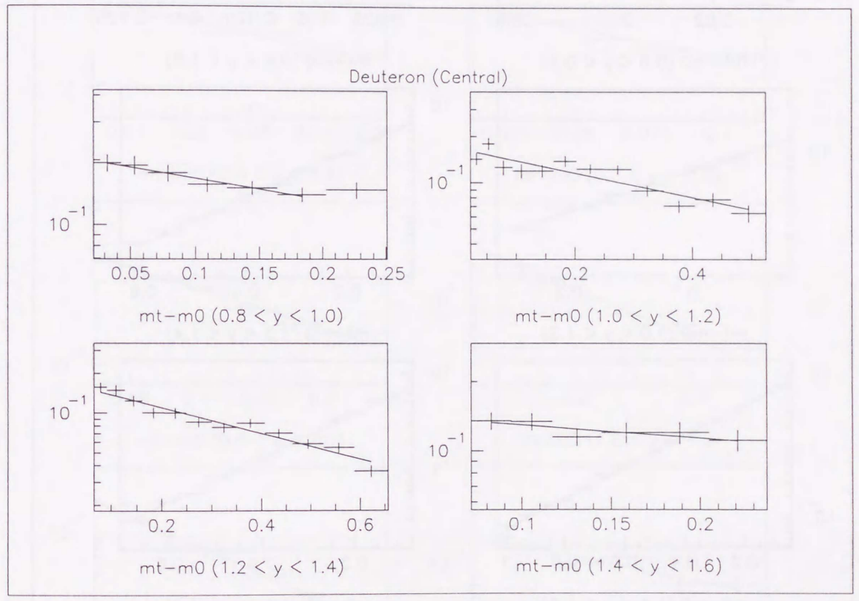

Fig. 5.10: Deuteron fitting in central collisions. The x-axis is $m_t - m_0$ [GeV/c^2] and the y-axis is invariant differential cross section [barn GeV^{-2}c^4].

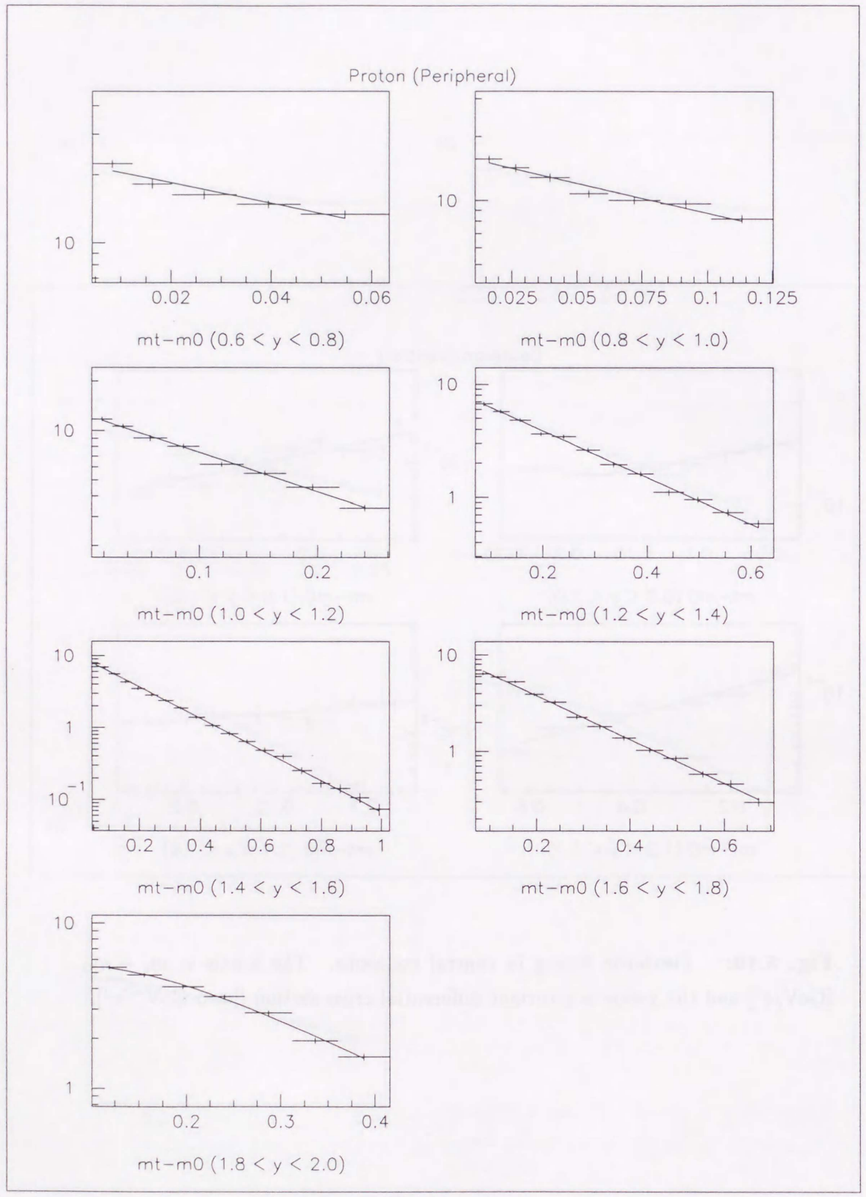

Fig. 5.11: Proton fitting in peripheral collisions. The x-axis is $m_t - m_0$ [GeV/c^2] and the y-axis is invariant differential cross section [barn GeV^{-2}c^4].

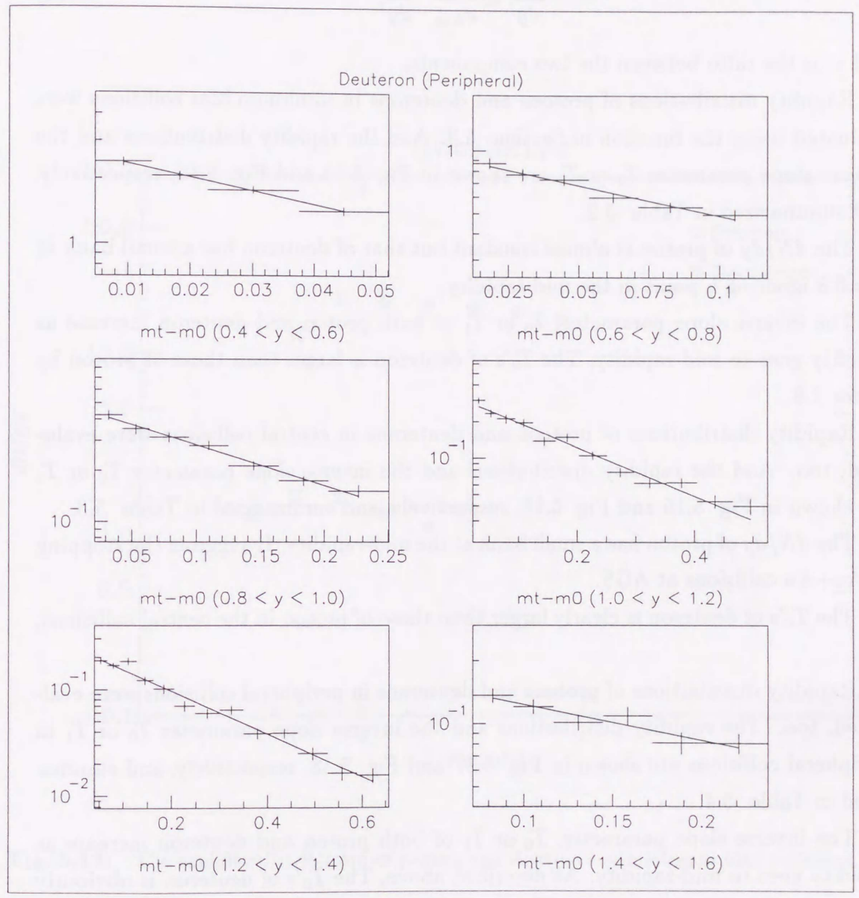

Fig. 5.12: Deuteron fitting in peripheral collisions. The x-axis is $m_t - m_0$ [GeV/c^2] and the y-axis is invariant differential cross section [barn GeV^{-2}c^4].

assuming the double exponential, where dN/dy is the particle yield per trigger in a unit rapidity (rapidity density) defined as

$$\frac{dN}{dy} \equiv \frac{1}{\sigma_{trig}} \cdot \frac{d\sigma}{dy}, \tag{5.14}$$

and w is the ratio between the two components.

Rapidity distributions of protons and deuterons in minimum bias collisions were evaluated using the function in Section 5.3. And the rapidity distributions and the inverse slope parameter T_0 or T_1 are shown in Fig 5.13 and Fig 5.14, respectively, and summarized in Table 5.2.

The dN/dy of proton is almost constant but that of deuteron has a small bank at $y = 0.8$ ignoring a point in the mid-rapidity.

The inverse slope parameter, T_0 or T_1 of both proton and deuteron increase as rapidity goes to mid-rapidity. The T_0's of deuteron is larger than those of proton by factor 1.8.

Rapidity distributions of protons and deuterons in central collisions were evaluated, too. And the rapidity distributions and the inverse slope parameter T_0 or T_1 are shown in Fig 5.15 and Fig 5.16, respectively, and summarized in Table 5.3.

The dN/dy of proton has a small bank at the mid-rapidity. It suggests the stopping of Au+Au collisions at AGS.

The T_0's of deuteron is clearly larger than those of proton in the central collisions, too.

Rapidity distributions of protons and deuterons in peripheral collisions were evaluated, too. The rapidity distributions and the inverse slope parameter T_0 or T_1 in peripheral collisions are shown in Fig 5.17 and Fig 5.18, respectively, and summarized in Table 5.4.

The inverse slope parameter, T_0 or T_1 of both proton and deuteron increase as rapidity goes to mid-rapidity. As described above, The T_0's of deuteron is obviously larger than those of proton in both the minimum bias and the central collisions. But T_0's of deuteron is similar to that of proton.

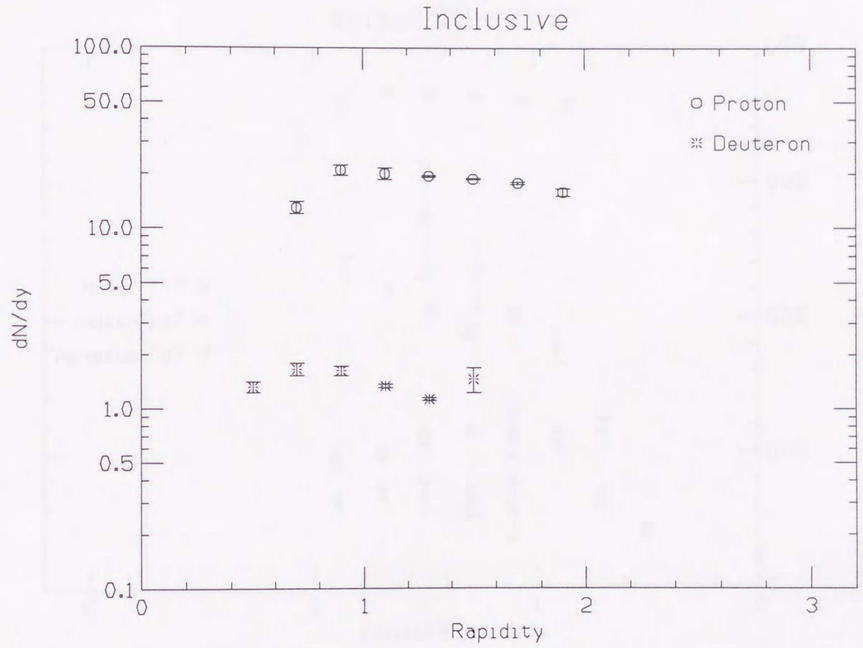

Fig. 5.13: The rapidity distribution of proton and deuteron in minimum bias collisions

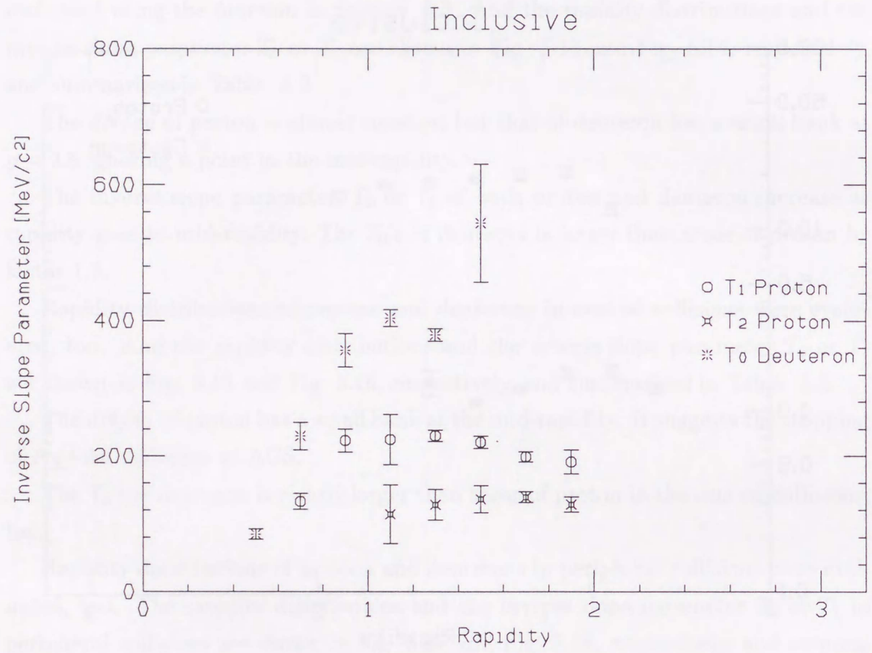

Fig. 5.14: The inverse slope parameter as function of rapidity for proton and deuteron in minimum bias collisions

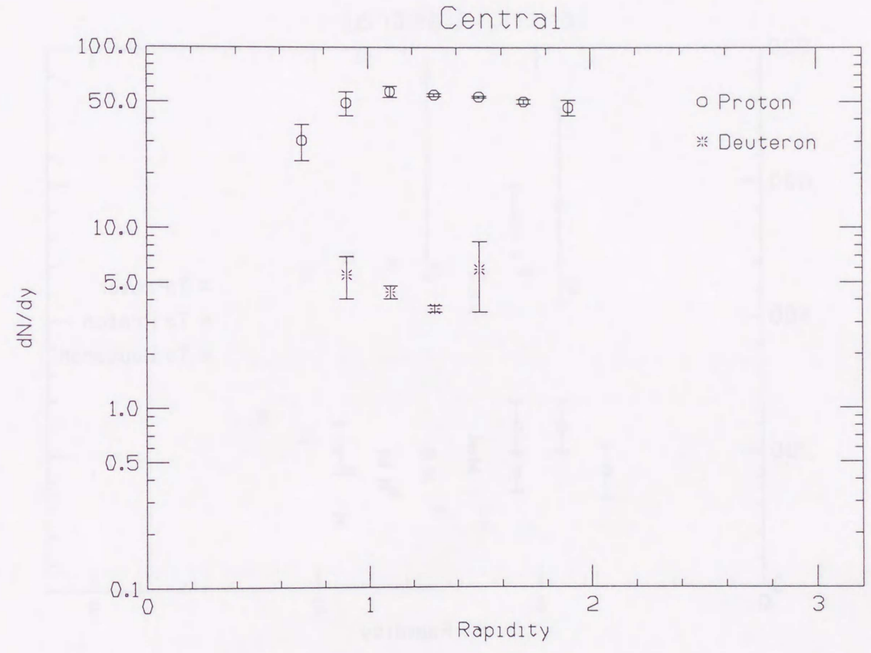

Fig. 5.15: The rapidity distribution of proton and deuteron in central collisions

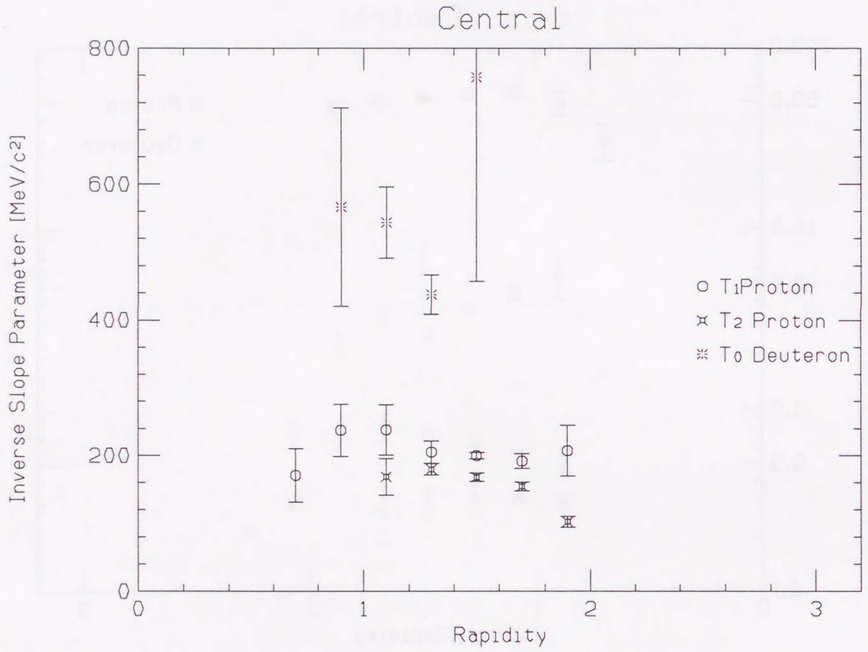

Fig. 5.16: The inverse slope parameter as function of rapidity for proton and deuteron in central collisions

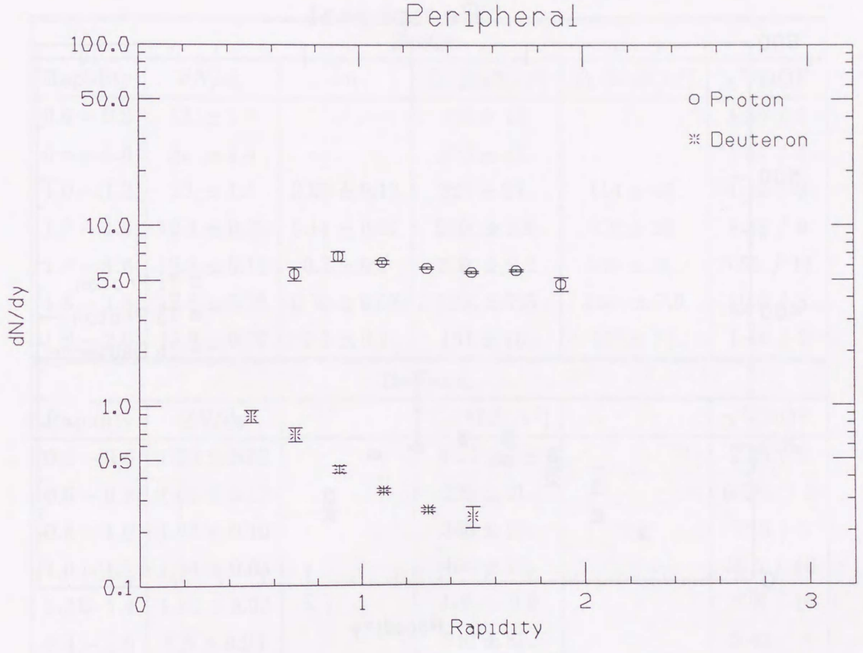

Fig. 5.17: The rapidity distribution of proton and deuteron in peripheral collisions

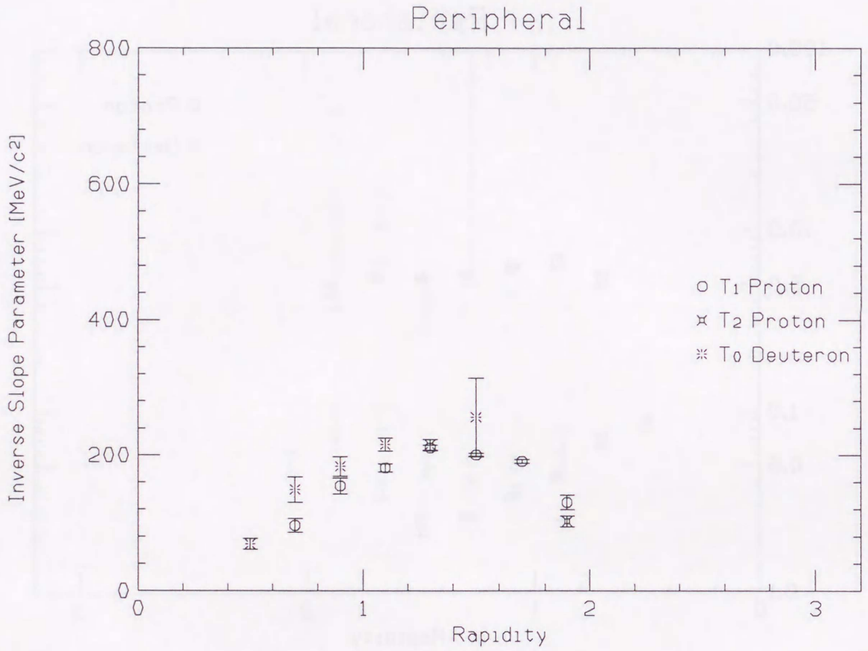

Fig. 5.18: The inverse slope parameter as function of rapidity for proton and deuteron in peripheral collisions

Proton					
Rapidity	dN/dy	$-w$	T_1 [MeV/c^2]	T_2 [MeV/c^2]	χ^2/DOF
$0.6-0.8$	$13.\pm1.0$		$133\pm12.$		5.59 / 3
$0.8-1.0$	$21.\pm1.4$		$223\pm17.$		1.47 / 4
$1.0-1.2$	$20.\pm1.5$	0.09 ± 0.13	$224\pm37.$	$114\pm43.$	1.66 / 3
$1.2-1.4$	19.4 ± 0.20	0.14 ± 0.07	$230.\pm8.6$	$128\pm23.$	9.58 / 9
$1.4-1.6$	18.8 ± 0.16	0.3 ± 0.1	$220.\pm9.2$	$136\pm20.$	5.87 / 14
$1.6-1.8$	17.8 ± 0.28	0.50 ± 0.08	$199.\pm7.5$	$139.\pm7.9$	10.8 / 8
$1.8-2.0$	15.9 ± 0.77	0.5 ± 0.1	$191\pm18.$	$129\pm11.$	1.16 / 3
Deuteron					
Rapidity	dN/dy		T_0 [MeV/c^2]		χ^2/DOF
$0.4-0.6$	1.32 ± 0.09		84.7 ± 7.8		2.26 / 2
$0.6-0.8$	1.66 ± 0.13		$229\pm21.$		0.781 / 3
$0.8-1.0$	1.63 ± 0.10		$356\pm25.$		3.15 / 5
$1.0-1.2$	1.34 ± 0.03		$404\pm12.$		28.5 / 10
$1.2-1.4$	1.13 ± 0.02		$379.\pm9.2$		26.8 / 10
$1.4-1.6$	1.5 ± 0.23		$540\pm87.$		5.43 / 4

Table 5.2: The rapidity densities dN/dy, the enhancement factor w, the inverse slope parameters T_0 or T_1 and T_2 and chi^2 in minimum bias collisions.

Proton					
Rapidity	dN/dy	$-w$	T_1 [MeV/c^2]	T_2 [MeV/c^2]	χ^2/DOF
$0.6-0.8$	30.4 ± 6.9		$171 \pm 39.$		1.06 / 3
$0.8-1.0$	49.1 ± 7.4		$237 \pm 39.$		0.341 / 4
$1.0-1.2$	56.8 ± 4.1	0.33 ± 0.17	$238 \pm 37.$	$169 \pm 27.$	6.26 / 7
$1.2-1.4$	54.4 ± 1.0	0.68 ± 0.13	$205 \pm 16.$	179.7 ± 8.4	5.91 / 9
$1.4-1.6$	53.2 ± 0.7	0.71 ± 0.05	199.9 ± 4.6	167.9 ± 6.0	12.5 / 14
$1.6-1.8$	50.1 ± 1.4	0.71 ± 0.07	$192 \pm 11.$	154.5 ± 6.6	13.1 / 8
$1.8-2.0$	46.4 ± 4.6	0.68 ± 0.18	$210 \pm 38.$	$170 \pm 20.$	0.404 / 2
Deuteron					
Rapidity	dN/dy		T_0 [MeV/c^2]		χ^2/DOF
$0.8-1.0$	5.5 ± 1.4		570 ± 146		2.29 / 5
$1.0-1.2$	4.39 ± 0.36		$544 \pm 52.$		24.6 / 10
$1.2-1.4$	3.54 ± 0.14		$438 \pm 29.$		13.7 / 10
$1.4-1.6$	5.9 ± 2.5		760 ± 300		1.27 / 4

Table 5.3: The rapidity densities dN/dy, the enhancement factor w, the inverse slope parameters T_0 or T_1 and T_2 and chi^2 in central collisions.

Proton					
Rapidity	dN/dy	$-w$	T_1 [MeV/c^2]	T_2 [MeV/c^2]	χ^2/DOF
$0.6-0.8$	5.40 ± 0.46		$96. \pm 10.$		7.26 / 3
$0.8-1.0$	6.73 ± 0.41		$155. \pm 12.$		7.97 / 5
$1.0-1.2$	6.24 ± 0.15		181.3 ± 6.0		5.47 / 6
$1.2-1.4$	5.78 ± 0.08		210.7 ± 4.4		12.6 / 10
$1.4-1.6$	5.47 ± 0.07		200.2 ± 2.5		17.7 / 17
$1.6-1.8$	5.58 ± 0.07		191.0 ± 2.9		22.0 / 11
$1.8-2.0$	4.68 ± 0.42	0.728 ± 0.072	$130. \pm 11.$	102.4 ± 8.1	6.74 / 3
Deuteron					
Rapidity	dN/dy		T_0 [MeV/c^2]		χ^2/DOF
$0.4-0.6$	0.874 ± 0.069		69.0 ± 8.0		0.136 /2
$0.6-0.8$	0.691 ± 0.061		$149. \pm 19.$		2.09 / 4
$0.8-1.0$	0.441 ± 0.020		$184. \pm 14.$		2.36 / 5
$1.0-1.2$	0.335 ± 0.009		215.7 ± 9.5		18.9 / 10
$1.2-1.4$	0.261 ± 0.007		215.3 ± 8.0		19.5 / 11
$1.4-1.6$	0.238 ± 0.032		$256 \pm 58.$		2.45 / 4

Table 5.4: The rapidity densities dN/dy, the enhancement factor w, the inverse slope parameters T_0 or T_1 and T_2 and chi^2 in peripheral collisions.

Chapter 6

Discussion

At the early stage of the heavy ion collisions, the baryon density and temperature goes up by nucleon+nucleon collisions, where the mean free path is expected to be less than 1 fm assuming the n-n cross section as 40 mb. The mean free path is much less than the radius of the reaction volume at this stage. Then, the baryon density and temperature go down due to expansion. After the mean free path becomes nearly equal to the radius of the reaction volume, the particles are expected to behave as free particles. This phenomenon is called freeze-out, and the density of the reaction volume at that time is called freeze-out density.

For the study of reaction mechanism, and also for the test of the creation of an exotic states of matter, it is important to study how and when the freeze-out occurs in the evolution. Study of composite particle production in terms of coalescence model will shed light on this subject.

6.1 Production Mechanism of Composite Particles

Productions of composite particles such as deuteron and triton in heavy ion collisions are interesting by itself. As an example, deuteron is made of proton and neutron with the binding energy of 2.2 MeV. Such weakly bound objects are produced in heavy ion environment where the temperature may be ~150 MeV or even higher. The composite particles may be struck out from the target or projectile nuclei in the heavy ion collisions. However, near the mid-rapidity region, it may not kinematically be correct.

In order to investigate the contribution of the fragment deuterons, probability of

deuterons at the beam(target) rapidity to be kicked to mid-rapidity region is evaluated using the elastic cross section of $d + p \to d + p$ [7],

$$\frac{d\sigma_{pd}}{dt} \leq 0.14\ [\mu\mathrm{b}/(\mathrm{GeV/c})^2], \tag{6.1}$$

where t denotes the momentum transfer. This differential cross section is measured at $t \geq 1.8$ $[(\mathrm{GeV/c})^2]$. A deuteron produced as the target fragment must get $t \sim 4(\mathrm{GeV/c})^2$ to be observed around mid-rapidity region at 12 A·GeV/c through a collision with a projectile nucleon. The mean free path of the elastic collision in the projectile rest frame for $3.5 < t < 4.5(\mathrm{GeV/c})^2$ is $d_{pd} > \frac{1}{\rho_0 \int_{t=3.5}^{t=4.5} \frac{d\sigma_{pd}}{dt} dt} \sim 4.2 \times 10^5$ [fm], where ρ_0 represents the baryon density in the normal nucleus of 0.17 [fm^{-3}]. On the other hand, the radius of a heavy ion, for example Au nucleus, is $R_{Au} \sim 8$ [fm]. Thus, the possibility that a target fragment is accelerated to the mid-rapidity region is less than of the order of 10^{-4} and this is negligible. Note that the probability to find deuteron in nucleus is ignored here.

Therefore, the composite particles near the mid-rapidity must be produced in the high density region. Although the composite particle can be produced directly with anti-particle in the high energy collisions, the probability of direct production is quite small.

Direct production of deuterons through $NN \to NNd\overline{d}$ can be estimated with anti-deuteron yields. E858 collaboration measured anti-deuteron production in 14.6 AGeV/c Si+Au collisions at zero degree [8]. They measured invariant $\overline{d}$ cross section at $p = 6.1$ GeV/c;

$$E\frac{d^3\sigma_{\overline{d}}}{dp^3} = (4 \pm 3) \times 10^{-5}\ [\mathrm{mb/GeV^2}]. \tag{6.2}$$

On the other hand, the d yield measured by the E886 collaboration at $p = 1.8$ GeV/c is as follows [22];

$$E\frac{d^3\sigma_d}{dp^3} = (6.91 \pm 0.27) \times 10^2\ [\mathrm{mb/GeV^2}]. \tag{6.3}$$

The ratio $\overline{d}/d$ is of the order of 10^{-7}. Thus, the contribution of direct d production is negligible.

6.2 Power Law in the Coalescence Model

The most successful model to describe composite particle production in A+A collisions at Bevalac and p+A and p+p at CERN is the coalescence model. One of the

first questions here is whether power law holds in the heavy ion collisions at AGS energy or not.

The invariant cross section of a produced composite particle with the mass number A is related to the observed cross section of proton in the coalescence model, as [46]

$$E_A \frac{d^3\sigma_A}{dp_A^3} = C_A \left(E_p \frac{d^3\sigma_p}{dp_p^3} \right)^A, \tag{6.4}$$

or

$$E_A \frac{d^3N_A}{dp_A^3} = B_A \left(E_p \frac{d^3N_p}{dp_p^3} \right)^A, \tag{6.5}$$

$$\frac{dN}{dy} \equiv \frac{1}{\sigma_{trig}} \cdot \frac{d\sigma}{dy}, \tag{6.6}$$

$$B_A = C_A \cdot \sigma_{trig}^{A-1}. \tag{6.7}$$

where $p_A = A \cdot p_p$, C_A and B_A are coalescence scaling coefficients, dN/dy is the particle yield per trigger in a unit rapidity (rapidity density). Those relations assume that the shapes of the proton and neutron spectra are identical. This relation is called as a power law of the coalescence model. Assuming that the probability depends on only the density at the momentum phase space, the coalescence scaling coefficient, B_A, can be given with the reduced coalescence radius, $\tilde{p_0}$, as [47]

$$B_A = A \frac{2S_A + 1}{2^A} \frac{1}{N!Z!} \left(\frac{N_p + N_t}{Z_p + Z_t} \right)^N \left(\frac{4\pi}{3m} \tilde{p_0}^3 \right)^{A-1}, \tag{6.8}$$

where S_A is the ground state spin of the composite particle, N, N_p, N_t are the composite particle, projectile, target neutron numbers, respectively, Z, Z_p, Z_t are the composite particle, projectile, target proton numbers, respectively, m is the nucleon rest mass. The value of $\tilde{p_0}$ corresponds to the maximum relative momentum for nucleons to merge together. To hold this power law, there are following requirements:

1. the density of nucleon is low enough for the gas picture to hold,
2. the yield of the composite particles is much smaller than that of proton(neutron), then the composite particle production does not affect the yield of proton(neutron).

The B_A should be constant for a given composite particle species since it depends on only mass number of the composite particle in Eq. 6.8. In order to test the power law, one has to show that the B_A does not depend on p_t (or m_t) and y of the produced composite particle.

The feature of the power law can be shown with the thermal model also. This is discussed in Section 6.5.1.

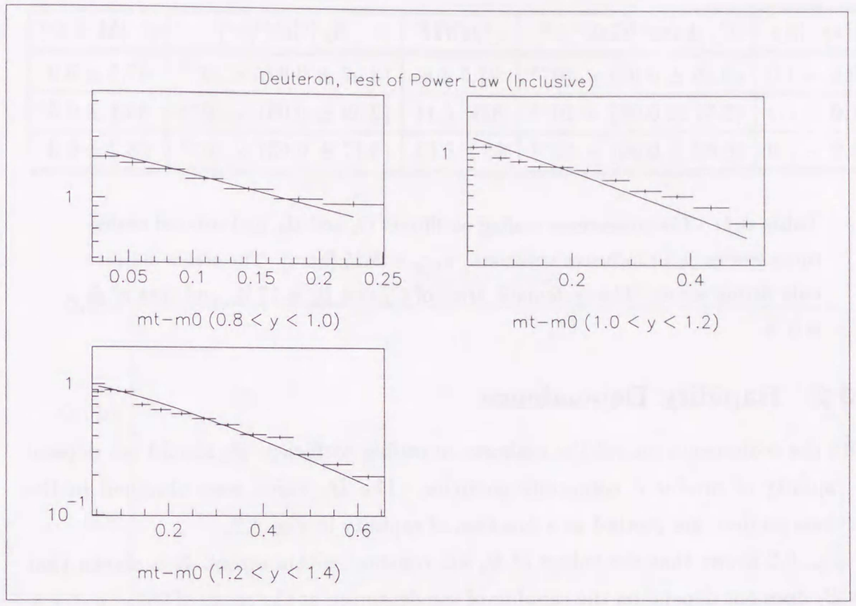

Fig. 6.1: Test of power law for deuteron in inclusive collisions. The x-axis is $m_t - m_0$ [GeV/c^2] and the y-axis is invariant differential cross section [barn GeV^{-2}c^4].

6.3 Test of Power Law in Inclusive Collisions

6.3.1 Power Law

The power law is examined to the inclusive spectra of deuteron at each rapidity slice, and we obtain the coalescence scaling coefficient C_2 of deuteron (A =2).

Fig. 6.1 shows deuteron spectra with fitting function obtained from proton spectra in the inclusive collisions. Although the slope of the deuteron seems to be larger, the expected spectrum by the power law is consistent with the spectrum of deuteron within 10% at the p_t region observed for all rapidity slices. The power law can describe deuteron spectra within 10 % in the inclusive collisions. The C_2 and B_2 are summarized in Table 6.1.

Rapidity	C_2 [barn^{-1}GeV^2/c^2]	χ^2/DOF	B_2 [GeV^2/c^2]	$\tilde{p_0}$ [MeV/c]
0.8 – 1.0	$(5.85 \pm 0.07) \times 10^{-4}$	21.5 / 6	$(3.07 \pm 0.04) \times 10^{-3}$	67.5 ± 0.3
1.0 – 1.2	$(5.51 \pm 0.06) \times 10^{-4}$	203. / 11	$(2.89 \pm 0.03) \times 10^{-3}$	66.1 ± 0.3
1.2 – 1.0	$(6.03 \pm 0.06) \times 10^{-4}$	85.1 / 12	$(3.17 \pm 0.03) \times 10^{-3}$	68.2 ± 0.3

Table 6.1: The coalescence scaling coefficient C_2 and B_2, and reduced coalescence radius $\tilde{p_0}$ in inclusive collisions. $\sigma_{trig} = 5.25$ [barn]. The errors indicate only fitting errors. The systematic error of C_2 and B_2 is 17 %, and that of $\tilde{p_0}$ is 6 %.

6.3.2 Rapidity Dependence

With the coalescence model, the coalescence scaling coefficient B_A should not depend on rapidity of produced composite particles. The B_2 which were obtained in the previous section, are plotted as a function of rapidity in Fig. 6.2.

Fig. 6.2 shows that the values of B_2 are constant within errors. It is shown that the B_2 does not depend on the rapidity of the deuterons at the range of $0.8 < y < 1.4$. The independence of B_2 from $p_t(m_t)$ and y of the produced deuteron suggests that the power law also holds in the Au+Au collisions at AGS energy.

6.3.3 Comparison with Collisions at Other Energies

The obtained B_2 are compared with the other experiments at the other collisions/beam energies in Fig. 6.3. All the measurements were carried out with minimum bias triggers in this figure. Many experiments at Bevalac claim that B_2 is fairly independent of the beam energy and of the system size of the collisions. The same value of B_2's are observed in p+A collisions at CERN also. The universality of coalescence scaling coefficient, B_2 has been considered to support that the coalescence scaling coefficients are governed only by $\tilde{p_0}$.

However, our B_2 of inclusive measurement is obviously smaller than those of the other experiments by a factor of 5. Such small B_2 was never reported from Bevalac experiments. There is clear departure from the general trend which has been believed from A+A experiments at Bevalac and p+A experiments at CERN. This dramatic change was also reported from the previous measurements at AGS. Systematic study of deuteron production were awaiting for in order to confirm and to clarify the im-

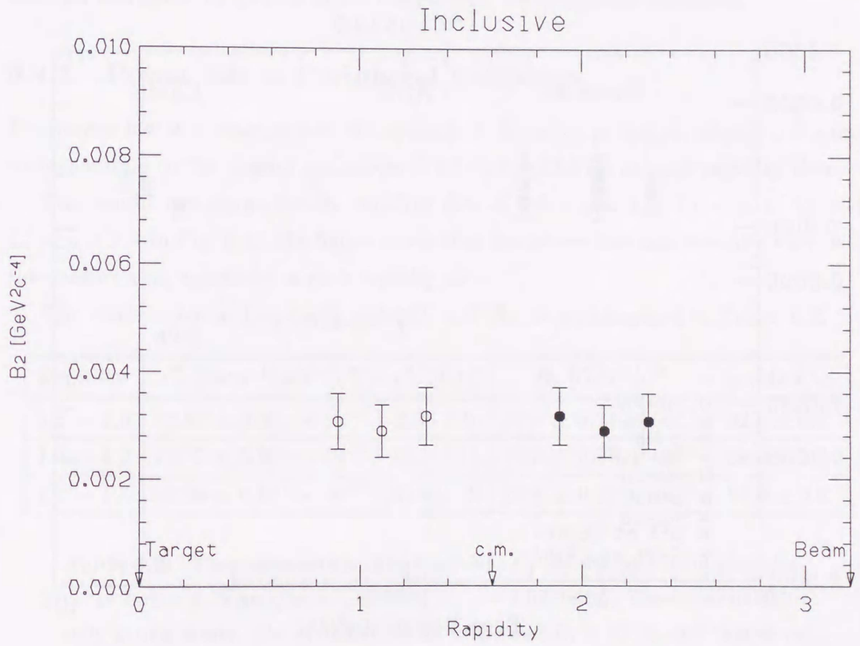

Fig. 6.2: B_2 as a function of the rapidity in inclusive collisions. The filled circles are reflected data. The error bars indicate the systematic errors.

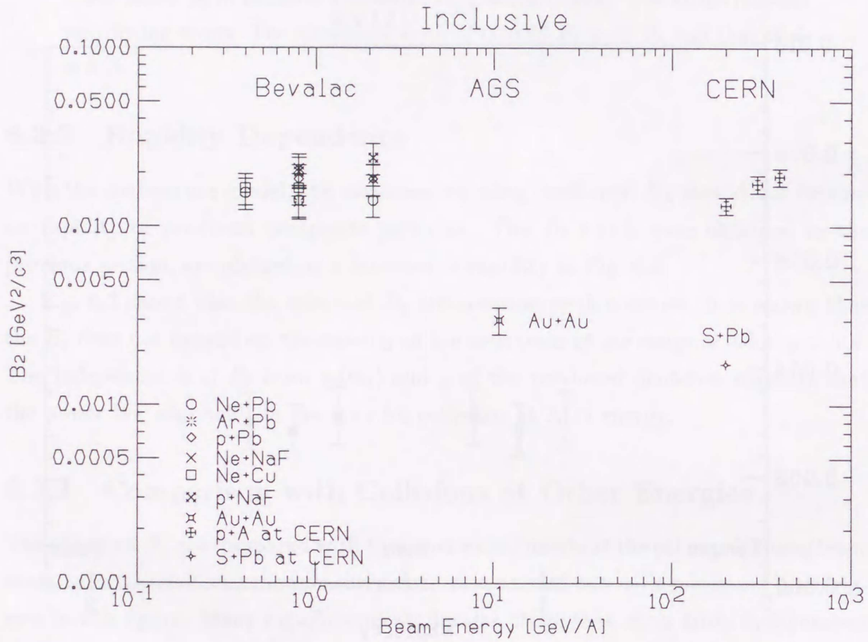

Fig. 6.3: B_2 as a function of beam energy in the inclusive collisions.

portance of this effect.

6.4 Centrality Dependence

To investigate the system size dependence of B_2, we perform the comparison of B_2 in the central collisions and the peripheral collisions. The test of the power law is also done for deuteron m_t spectra in the central and the peripheral collisions.

6.4.1 Power law in Peripheral Collisions

The power law was examined to the spectra of deuteron in the peripheral collisions corresponding to the impact parameter of $9.1 < b < 12.9$ fm at each rapidity slice.

The results are shown for the rapidity slice of $0.8 < y < 1.0$, $1.0 < y < 1.2$ and $1.2 < y < 1.4$ in Fig. 6.4. The figure shows that the power law can describe very well the deuteron m_t spectrum in each rapidity slice.

The coalescence scaling coefficients, C_2 and B_2 are summarized in Table 6.2.

Rapidity	C_2 [barn^{-1}GeV^2/c^2]	χ^2/DOF	B_2 [GeV^2/c^2]	$\tilde{p_0}$ [MeV/c]
$0.8 - 1.0$	$(2.98 \pm 0.08) \times 10^{-3}$	2.38 / 6	$(7.8 \pm 0.2) \times 10^{-3}$	92.0 ± 0.8
$1.0 - 1.2$	$(3.17 \pm 0.08) \times 10^{-3}$	18.1 / 11	$(8.3 \pm 0.2) \times 10^{-3}$	94.0 ± 0.8
$1.2 - 1.4$	$(2.59 \pm 0.07) \times 10^{-3}$	23.4 / 12	$(6.8 \pm 0.2) \times 10^{-3}$	87.9 ± 0.8

Table 6.2: The coalescence scaling coefficient C_2 and B_2, and reduced coalescence radius $\tilde{p_0}$ in peripheral collisions. $\sigma_{trig} = 2.62$ [barn]. The errors indicate only fitting errors. The systematic error of C_2 and B_2 is 17 %, and that of $\tilde{p_0}$ is 6 %.

6.4.2 Rapidity Dependence in Peripheral Collisions

The B_2 which obtained by examination of the power law, are plotted as a function of rapidity in Fig. 6.5.

Although the systematic errors of the B_2 in the peripheral collisions is larger, a clear dependence of B_2 on the rapidity is not found in Fig. 6.5.

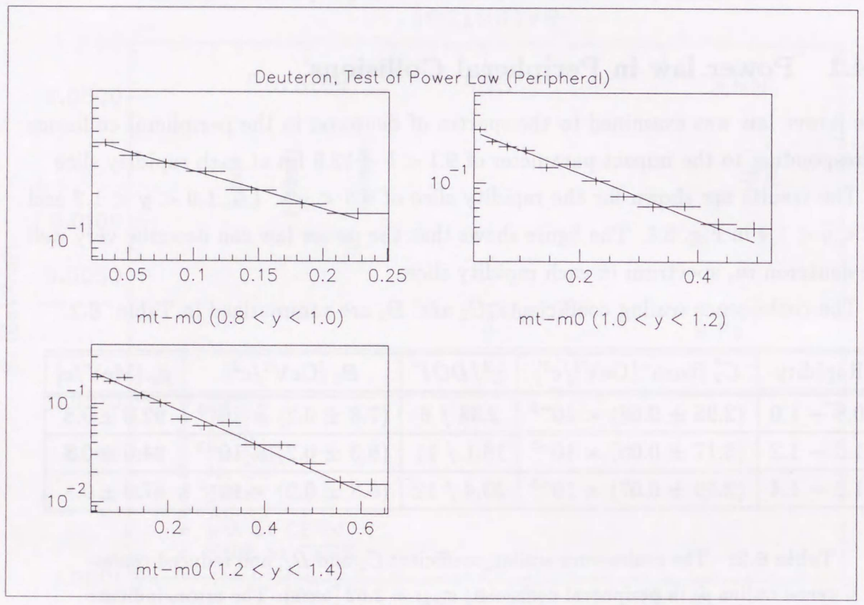

Fig. 6.4: Test of power law for deuteron in peripheral collisions. The x-axis is $m_t - m_0$ [GeV/c^2] and the y-axis is invariant differential cross section [barn GeV^{-2}c^4].

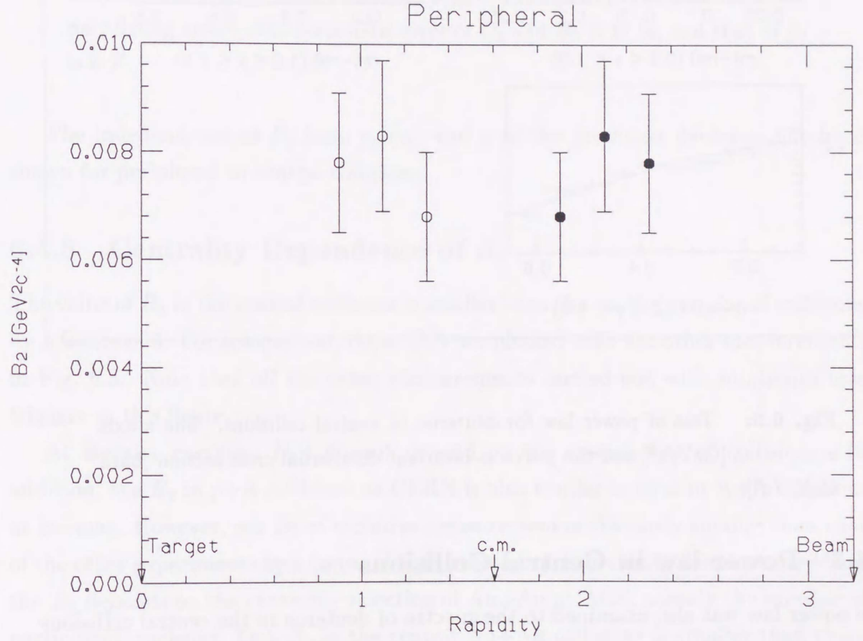

Fig. 6.5: B_2 as a function of rapidity in peripheral collisions. The filled circles are reflected data. The error bars indicate the systematic errors.

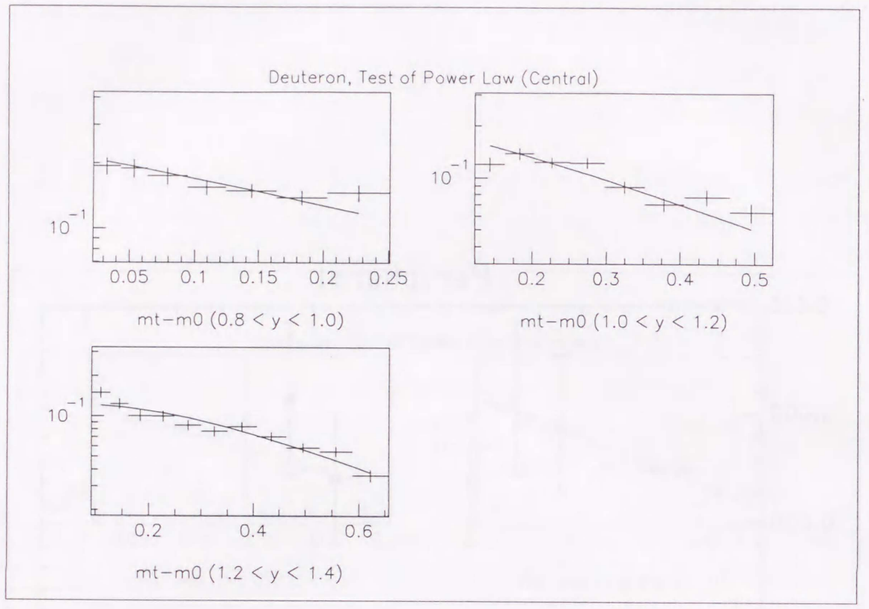

Fig. 6.6: Test of power law for deuteron in central collisions. The x-axis is $m_t - m_0$ [GeV/c^2] and the y-axis is invariant differential cross section [barn GeV^{-2}c^4].

6.4.3 Power law in Central Collisions

The power law was also examined to the spectra of deuteron in the central collisions corresponding to the impact parameter of $0 < b < 3.2fm$ at each rapidity slice.

The fitting results are shown in Fig. 6.6. The figure shows that the power law also can describe the deuteron m_t spectra in the central collisions within $10 \sim 20$ % in each rapidity slice.

The coalescence scaling coefficients, C_2 and B_2 are summarized in Table 6.3.

6.4.4 Rapidity Dependence in Central Collisions

The B_2 are plotted as a function of rapidity in Fig. 6.7. The figure shows that the values of B_2 are constant within errors. It is confirmed that the B_2 does not depend on the rapidity of the deuterons in the central collisions.

Rapidity	C_2 [barn^{-1}GeV^2/c^2]	χ^2/DOF	B_2 [GeV^2/c^2]	$\tilde{p_0}$ [MeV/c]
0.8 − 1.0	$(3.8 \pm 0.1) \times 10^{-3}$	6.24 / 6	$(1.19 \pm 0.04) \times 10^{-3}$	49.2 ± 0.5
1.0 − 1.2	$(3.9 \pm 0.1) \times 10^{-3}$	20.5 / 7	$(1.24 \pm 0.04) \times 10^{-3}$	49.9 ± 0.5
1.2 − 1.0	$(4.2 \pm 0.1) \times 10^{-3}$	16.4 / 10	$(1.32 \pm 0.04) \times 10^{-3}$	50.9 ± 0.5

Table 6.3: The coalescence scaling coefficient C_2 and B_2, and reduced coalescence radius $\tilde{p_0}$ in central collisions. $\sigma_{trig} = 0.315$ [barn]. The errors indicate only fitting errors. The systematic error of C_2 and B_2 is 17 %, and that of $\tilde{p_0}$ is 6 %.

The independence of B_2 from $p_t(m_t)$ and y of the produced deuteron has been shown for peripheral to central collisions.

6.4.5 Centrality Dependence of B_2

The value of B_2 in the central collisions is smaller than that in the peripheral collisions by a factor of 5. For comparison, those B_2's are plotted with the other measurements in Fig. 6.8. Note that all the other measurements carried out with minimum bias triggers in this figure.

At Bevalac energies, B_2's do not depend on the system size of collisions. In addition, the B_2 in p+A collisions at CERN is also similar to that in A+A collisions at Bevalac. However, our B_2 of inclusive measurement is obviously smaller than that of the other experiments by a factor of 5. Furthermore, it is clearly demonstrated that the B_2 depends on the centrality selection of Au+Au at AGS, namely the number of participant nucleons. Our B_2 in the central Au+Au collisions is smaller than those of other experiments by a factor of 10.

This small B_2 in the inclusive collisions and the system size dependence of B_2 clearly break away from what is expected in the conventional coalescence model. This result also suggests that the coalescence of nucleons into composite particles is extremely influenced by the collision dynamics.

To explain our results, we investigate the effect of deuteron breakup by nucleons on B_2. The inelastic cross section of p+d collisions is $70 \sim 90$ mb at the proton laboratory momentum of $1 - 10$ GeV/c [56]. The corresponding mean free path of deuterons is $0.7 \sim 0.8$ fm at the normal nucleus density. On the other hand, the radius of the participant volume in the central Au+Au collisions is about 7.2 fm, assuming

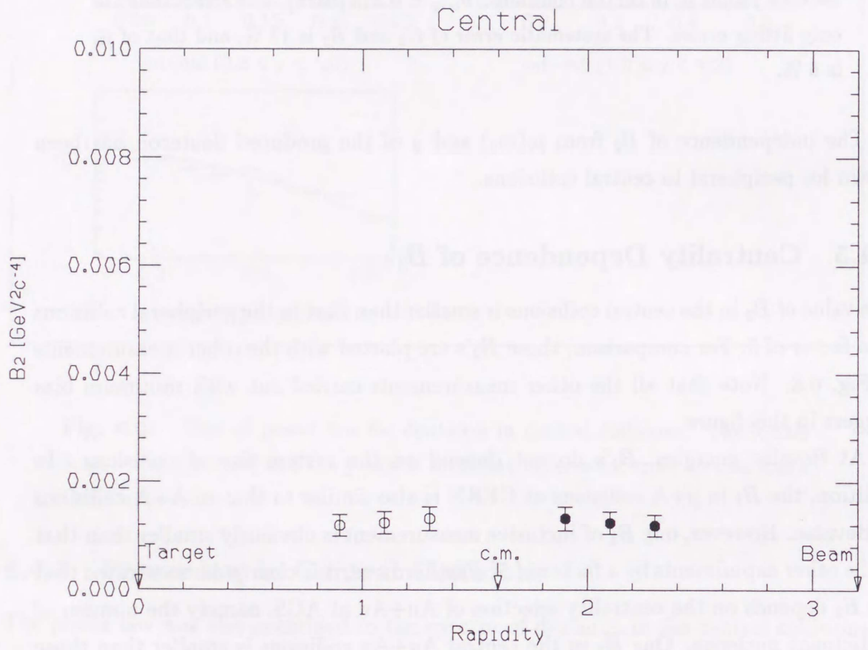

Fig. 6.7: B_2 as a function of rapidity in the central collisions. The filled circles are reflected data. The error bars indicate the systematic errors.

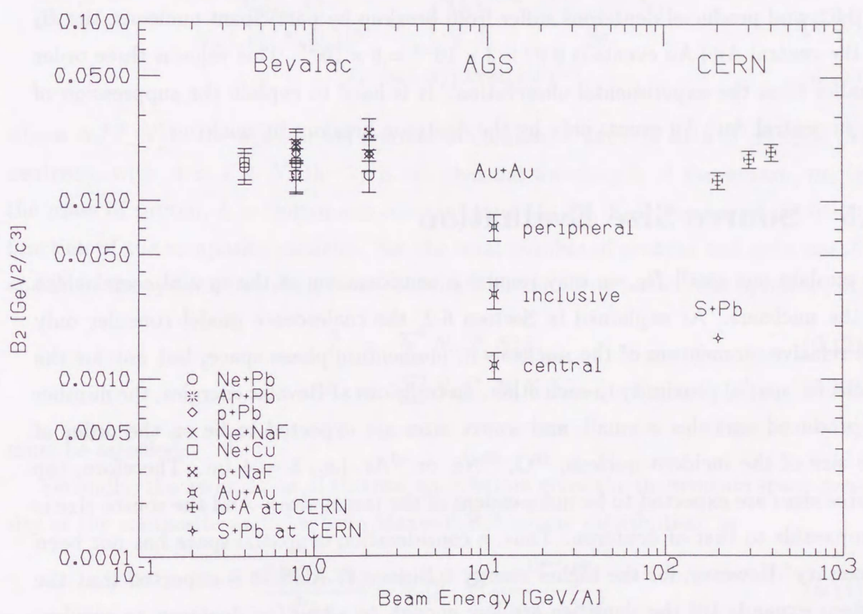

Fig. 6.8: B_2 as a function of beam energy.

the sphere shape. The mean free path is much smaller than the participant volume size. Therefore, the survival probability of a deuteron produced in the participant volume is 3×10^{-5} for the central events, assuming the deuteron path length to be the participant radius. The B_2's for Bevalac and CERN data in inclusive events are about 0.02 independent of the beam energy, while the B_2 in central Au+Au collisions is about 0.001.

Suppose the initial deuteron and proton yields are described with the universal B_2 of 0.02, and produced deuterons suffer from breakup by participant nucleons, the B_2 in the central Au+Au events is $0.02 \times 3 \times 10^{-5} = 6 \times 10^{-7}$. This value is three order smaller than the experimental observation. It is hard to explain the suppression of B_2 in central Au+Au events only by the deuteron breakup by nucleons.

6.5 Source Size Evaluation

To explain our small B_2, we may require a consideration of the spatial correlations of the nucleons. As explained in Section 6.2, the coalescence model consider only the relative momentum of the nucleons in momentum phase space, but not for the nucleons' spatial proximity to each other. In collisions at Bevalac energies, the number of produced particles is small, and source sizes are expected to be on the order of the size of the incident nucleus, ^{16}O, ^{20}Ne, or ^{40}Ar, i.e., $3 \sim 4$ fm. Therefore, the source sizes are expected to be independent of the target sizes. And the source size is comparable to that of deuteron. Thus, a consideration of spatial space has not been necessary. However, for the higher energy collisions at AGS, it is expected that the system expands till the densities are low enough to allow the deuteron to survive. Thus the values of B_A might contain the information of the source size.

To extract the source size from the scaling coefficient B_2, we apply a thermal model developed by Mekjian [47, 48, 49] and a model developed by Sato and Yazaki [50].

6.5.1 Thermal Model

The thermal model developed by Mekjian [47, 48, 49] assumes that the thermal and chemical equilibrium are established in a reaction volume, $V(= 4\pi R_I^3/3)$ and the momentum distribution of the particles in V are given by the Maxwell-Boltzmann distribution.

First, the assumption of chemical equilibrium is expressed as,

$$\mu_{Z,N} = Z\mu_p + N\mu_n, \tag{6.9}$$

where Z and N indicate the number of proton and neutron forming the composite particle, and μ_i indicates the chemical potential of particle specie i, which leads immediately to the law of mass action:

$$\frac{N_0[Z,N]}{N_0[1,0]^Z N_0[0,1]^N} = \left(\frac{\lambda_T^3}{V}\right)^{A-1} \frac{A^{\frac{3}{2}} Z_{int}(Z,N)}{2^A}, \tag{6.10}$$

$$\lambda_T = h/(2\pi m_p kT)^{1/2}, \tag{6.11}$$

where $N_0[Z,N]$ is the equilibrium number of composite particle with Z protons, N neutrons, with $A = Z + N$, the λ_T is the thermal wavelength of the proton, m_p is the mass of proton, k is Boltzmann constant, and $Z_{int}[Z,N]$ is the initial partition function of the composite particles. For the total number of protons and neutrons,$\tilde{Z}$ and $\tilde{N}$ in the system, including those contained in composite nuclei, the equations of,

$$\tilde{Z} = \sum N_0[Z,N]Z, \tag{6.12}$$

$$\tilde{N} = \sum N_0[Z,N]N, \tag{6.13}$$

must be satisfied.

Secondly, the assumption of thermal equilibrium gives the momentum space density of the composite particles from Maxwell-Boltzmann distribution, as

$$\frac{d^3N_0[Z,N]}{d^3p_A} = N_0[Z,N]\frac{e^{-E^{kin}/kT}}{(2\pi m_A kT)^{\frac{3}{2}}}, \tag{6.14}$$

where the p_A is the momentum of the composite particles with A nucleons which is related to the total kinetic energy $E_K = p_A^2/2m_A$. The momentum space density, Eq. 6.14 is isotropic and it applies to the distribution in a rest frame.

The momentum space density of the composite particles can be written as a power of the proton momentum space density. Defining the momentum per nucleon $p_n = p_A/A$, and the kinetic energy per nucleon $E_n^{kin} = E_A^{kin}/A$, Eq. 6.14 can be written as,

$$\frac{d^3N_0[Z,N]}{d^3p_n} = A^3 Z_{int}[Z,N]\left(\frac{h^3}{V}\right)^{A-1}\left(\frac{N_0[0,1]}{n_0[1,0]}\right)^N\left(\frac{d^3N_0[1,0]}{d^3p_n}\right)^A. \tag{6.15}$$

In the conventional coalescence model, the number of composite particles per event per unit element of phase space, $d^3\tilde{N}[Z,N]/d^3p_n$ is written as,

$$\frac{d^3\tilde{N}[Z,N]}{d^3p_n} = A^3\frac{2S_A+1}{2_A}\frac{1}{Z!N!}\left(\frac{N_t+N_p}{Z_t+Z_p}\right)^N\left(\frac{4}{3}\pi\gamma\tilde{p_0}^3\right)^{A-1}\left(\frac{d^3\tilde{N}[1,0]}{d^3p_n}\right)^A, \quad (6.16)$$

where the $\gamma = (1+p_n^2/m_p^2$. Comparing Eq. 6.15 and Eq. 6.16, the interaction volume V in the thermal model can be correlated with the sphere in momentum space of the coalescence model. Thus the root mean square radius, $R_T = (3V/4\pi)^{1/3}$ of the interaction volume is given as

$$R_T^3 = (Z!N!)^{\frac{1}{A-1}}\left(\frac{3\pi\hbar^3}{2\tilde{p_0}^3}\right). \quad (6.17)$$

For the deuteron, the R_T is inversely proportional to the $\tilde{p_0}$. Therefore, by using the formula, source radius can be evaluated with this model from the composite particle production.

6.5.2 Sato-Yazaki Model

To extract the source size from the coalescence scaling coefficient B_2, we apply a model developed by Sato and Yazaki [50]. This model uses a density matrix formalism to describe a highly excited part formed in collisions. The model assumes that after first collisions, a highly excited part (HX) is formed temporarily, which then decays by emitting various particles. The momentum distributions of these particles are assumed to be approximately given by the density matrix at this stage. In this picture, neither thermal nor chemical equilibrium needs to be assumed. The model also assumes that the internal wave function of the composite particle produced in collisions and the spatial distribution function of the nucleons in HX are described with Gaussian function. Then, the momentum distribution of emitted composite particle is described with the Fourier transforms of the internal wave function of the composite particle and the spatial distribution function of the nucleons. Finally the model can be cast in the same form as the conventional coalescence model and the reduced coalescence radius, $\tilde{p_0}$, can be related to the size parameter of the excited region as [22],

$$\tilde{p_0} = \frac{\kappa_A\hbar}{\sqrt{R_{SY}^2+R_A^2}}, \quad (6.18)$$

where κ_A is a phase space factor which is determined by the mass number, A, and spin of the composite particles, S_A, R_A is the root mean square radius of the wave

function of the composite particle, R_{SY} is the rms radius of the source. The the κ_2 is 1.90 and the R_2 is 2.739 [fm] for deuteron. This model, however, needs caution for the application. First, this model is non-relativistic. In our case, this might require additional caution. Second, this model assumes a Gaussian distribution for the nucleon distribution. Therefore, the actual value of the source size might not be correct. However, as a first order evaluation, this model is very useful.

6.5.3 Source Size

The source sizes, R_T and R_{SY}, are obtained from the thermal model and the Sato-Yazaki model using Eq. 6.17 and Eq. 6.18, respectively, and listed in Table 6.4. The

Centrality	B_2 [GeV^2/c^2]	$\tilde{p_0}$ [MeV/c]	R_T [fm]	R_{SY} [fm]
Inclusive	$(3.0\pm0.5)\times10^{-3}$	67 ± 4	7.1 ± 0.4	4.9 ± 0.3
Peripheral	$(7.6\pm1.3)\times10^{-3}$	91 ± 5	5.2 ± 0.3	3.1 ± 0.2
Central	$(1.3\pm0.2)\times10^{-3}$	50 ± 3	9.5 ± 0.6	7.0 ± 0.4

Table 6.4: The source sizes, R_T and R_{SY}, deduced from the thermal model and the Sato-Yazaki model using Eq. 6.17 and Eq. 6.18, respectively. The errors indicate the systematic errors.

source sizes strongly depend on the centrality of the collisions, namely the values of both R_T and R_{SY} increase as collision system becomes large. To investigate the source size dependence, we have calculated the average number of participant nucleons from trigger cross sections. We have obtained the number of nucleons in spherical overlap of the target and projectile nucleus with the impact parameter calculated from the measured trigger cross sections. The source sizes are plotted as a function of the average number of participant nucleons in Fig. 6.9. The dot line represents the radius of normal nucleus. The figure shows that both R_T and R_{SY} relate the cubic of the number of participants, which suggests the nucleon density is constant when the deuterons are produced.

Assuming that the source is isotropic and the nucleon density is constant in the source, the nucleon density can be evaluated with R_T and R_{SY} and the number of participants. In Fig. 6.9, three points of R_T and R_{SY} are fitted with $y = R_0A^{1/3}$,

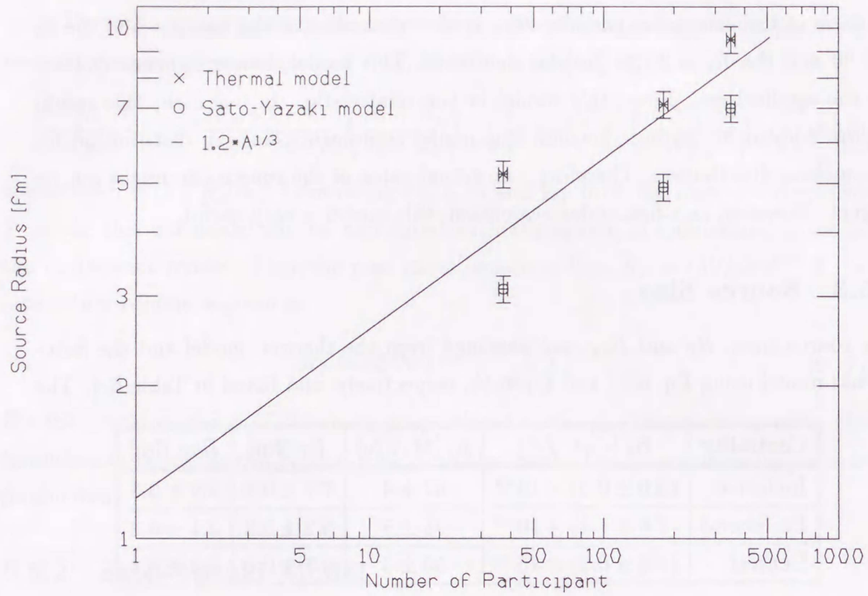

Fig. 6.9: The number of participant vs source radius deduced by the thermal model and the Sato-Yazaki model. The error bars are systematic errors.

respectively, and the nucleon density of the source, ρ is calculated as,

$$\rho = \frac{1}{\frac{4}{3}\pi R_0^3}. \tag{6.19}$$

The number densities of nucleon of the source from R_t and R_{SY} are 0.29 and 0.10 [fm^{-3}], respectively. These values are consistent with the nucleon density of normal nuclei, 0.16-0.17 [fm^{-3}], within a factor of 2. However, the source may not be isotropic, the nucleon density may not be constant in the source and the number of participant nucleons may not be the number of nucleons in spherical overlap of the target and projectile nucleus. Need caution for these numbers.

6.6 Comparison with RQMD

6.6.1 RQMD

RQMD(Relativistic Quantum Molecular Dynamics) is a microscopic cascade model to investigate space-time evolution of relativistic heavy ion collisions at Dubna, AGS and CERN energies. The model explicitly follows the trajectories of all hadrons including produced hadrons. Their propagations are done in the framework of relativistic constraint Hamiltonian dynamics [55]. The model combines the classical propagation of the hadrons with quantum effects as stochastic scattering, Pauli blocking in collisions. The formation probability of composite particles d, t and He is calculated by projecting a final nucleon phase space distribution on cluster wave-functions [52, 53, 54]. The source function for the nucleons is defined by the freeze-out positions x_i^μ and momenta p_i^μ of nucleons after their last scattering or decay. The basic assumption is that the single particle phase space density given by the transport model is good approximation to the density operator in the Wigner-representation.

6.6.2 Transverse Mass Spectra

If that the power law holds, the inverse slope parameters of deuterons are exactly equal to those of protons. In the peripheral collisions, the inverse slope parameters of deuterons are same with those of protons within 20 %. However, in the central collisions, the inverse slope parameters of deuterons seem to be larger than those of protons.

We compare our inverse slope parameters with those predicted by RQMD in which deuterons are produced with the coalescence scenario. With this model, Mattiello *et al.* has predicted m_t spectra of protons and deuterons in central Au+Au collisions ($b < 3$ fm) at AGS energy, 11.5 A·GeV with the mean field which causes the collective flow [51]. They claim that the influence of the flow increases the deuteron yield on the whole m_t, and makes the inverse slope parameter , T, larger. Further, the inverse slope of deuterons with the flow is larger than that of protons due to the flow. The m_t spectra were fitted to the Boltzmann function, as

$$\frac{1}{2\pi m_t}\frac{dN}{dm_t dy} = A \cdot m_t \exp\left(-\frac{m_t}{T}\right), \tag{6.20}$$

where A and T are fitting parameters.

Fig. 6.10 shows the m_t spectra of protons and deuterons with flow at $1.1 < y < 2.1$, and our spectra of protons and deuterons at the rapidity range of $1.2 < y < 1.4$.

In order to compare our data with their results, our m_t spectra for protons and deuterons in the central collisions at a rapidity slice of $1.2 < y < 1.4$ are refitted with Eq. 6.20. The inverse slope parameter T's, 214 ± 8 MeV/c^2 and 340 ± 28 MeV/c^2 are obtained for protons and deuterons. We also examine the power law to the deuteron spectrum of RQMD. In $0.3 < m_t - m_0$ [GeV/c^2] < 0.6, the power law can describe the deuteron spectrum within 20−30 %, but in lower $m_t - m_0$ less than 0.3 [GeV/c^2], the power law can not describe the deuteron spectrum. The B_2 in $0.3 < m_t - m_0$ [GeV/c^2] < 0.6 is $(1.4 \pm 1.2) \times 10^{-3}$ which is consistent with our $B_2 = (1.3 \pm 0.2) \times 10^{-3}$. Quantitatively, the strength of the effect does not agree, but, the tendency seems to be right direction. It is very interesting to compare RQMD calculations with high statistics deuteron data in future.

	Rapidity	$m_t - m_0$ [GeV/c^2]	T [MeV/c^2]		B_2 [GeV^2/c^4]
			p	d	
E866	$1.2 - 1.4$	$0.3 - 0.6$	214 ± 8	340 ± 28	$(1.3 \pm 0.2) \times 10^{-3}$
RQMD	$1.1 - 2.1$	$0.3 - 1.4$	$\simeq 200$	$\simeq 250$	$(1.4 \pm 1.2) \times 10^{-3}$

Table 6.5: The inverse slope parameters and the B_2 of E866 and RQMD in the central collisions. The errors of T of E866 and B_2 of RQMD are fitting errors and the error of B_2 of E866 is systematic error.

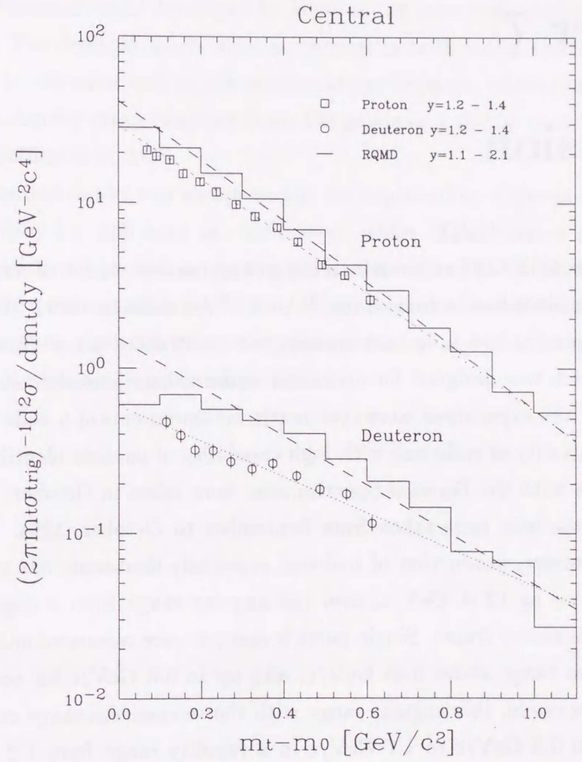

Fig. 6.10: The m_t spectra of protons and deuterons predicted by RQMD and E866 data. The solid histograms show the proton and the deuteron spectra by RQMD and the squares and circles are protons and deuterons of E866, respectively. The dash lines and dot lines show fitting result of the Boltzmann function.

Chapter 7

Conclusion

We performed the AGS-E866 experiment aiming at systematic studies of semi-inclusive spectra of various identified hadrons from ^{197}Au + ^{197}Au collisions at 11-12 A GeV/c. To measure hadrons at low p_t in mid-rapidity, we constructed a new forward-angle spectrometer which was designed for operation under a high particle-density condition. Features of the experiment were systematic measurements of a wide kinematic coverage and centrality of collisions with high capability of particle identification.

The first data with the Forward Spectrometer were taken in October, 1993, and data with large statistic were taken from September to October, 1994. With the Forward Spectrometer, production of hadrons, especially deuterons was studied for Au + Au collisions at 12 A GeV/c, over the angular range from 6 degrees to 28 degrees in the laboratory frame. Single particle spectra were measured and analyzed in the momentum range above 0.45 GeV/c, and up to 5.0 GeV/c for protons and deuterons. For example, this angular range with the momentum range corresponds to p_t ranges from 0.3 GeV/c to 1.7 GeV/c in a rapidity range from 1.2 to 1.4 for deuteron. Most importantly, proton and deuteron spectra such in the wide kinematic coverage with event characterization by the centrality of collisions were measured for the first time such a heavy collision system of Au+Au at the AGS energy.

We have shown that the observed deuteron spectra are consistent with the power law predicted and also the scaling coefficient, B_2 stays constant in the whole rapidity range of this experiment. Since this thesis contains data of deuteron only, we cannot claim all the composite production follows the power law. But, the deuteron production in the kinematic region covered in this experiment has been shown to be consistent with the power law.

Furthermore, we found that the scaling coefficient, B_2 depends strongly on the centrality of the collisions. This is the first real measurement of the centrality dependence of B_2. To explain this dependence, spatial proximity of nucleon is considered as an additional condition to the deuteron production. Using the Sato-Yazaki model and also the thermal model developed by Mekjian, we have evaluated the source sizes from the B_2. The deduced source sizes are similar in both model calculation and are proportional to the cubic root of the number of participants, which may suggest that the deuteron density stays constant from the peripheral to the central collisions of the Au+Au collisions at AGS.

Simple thermal model was shown to fail the explanation of the proton/pion production in heavy ion collisions at this energy, while RQMD seems to explain the deuterons production as well as proton/pion. Therefore, an intra-nuclear cascade model with composite particle production using the coalescence scenario, with higher statistical accuracy, and with other composite particles might be the most promising direction for further analysis of this problem.

Acknowledgments

I could never complete this thesis without helps, supports, and encouragements of a lot of people.

First of all, I thank Prof. K. Yagi for inviting me to this fascinating field of the relativistic heavy ion physics, and giving valuable advice. Special thanks are due to Prof. Y. Miake and Dr. K. Kurita for their continuous guidance, fruitful discussions, and zealous support in many aspects. Dr. Y. Miake gave me many great advice not only physics but also various techniques in hardware. A lot of discussions with him on this thesis helped me. Dr. K. Kurita told me many things not only physics but also life in America. His advice in analysis helped me.

I acknowledge three co-spokespersons of the BNL-E866, Dr. C. Chasman, Dr. H. Hamagaki, and Dr. S. G. Steadman for their great effort to organize for the collaboration.

I thank Ms. S. Ueno-Hayashi who and I worked together on the construction of FTOF.

I thank Dr. H. Sako for his advice in software and discussions with him and his friendship. These discussions helped me.

I thank Dr. Y. Akiba for their advice, supports and encouragements. I thank K. Shigaki for his contribution to the E866 Forward Spectrometer in hardware and software and his friendship.

I acknowledge Japanese collaborators, Prof. R. S. Hayano, Prof. S. Homma, and S. Nagamiya, for their advice, supports and encouragements.

I especially thank collaborators who worked for the Forward Spectrometer; Dr. Z. Chen, Ms. E. -J. Kim, Dr. J. H. Lee, Dr, C. Muentz, Mr. K. Nagano, Mr. T. Tamagawa, Mr. K. Ohyama, and Dr. F. Zhu.

I thank collaborators of the E866 collaboration; Mr. L. Ahle, Dr. K. Ashktorab, Dr. M. Baker, Dr. D. Beavis, Dr. H. C. Britt, Dr. J. Chang, Dr. C. -Y. Chi, Dr. Y. Y. Chu, Dr. V. Cianciolo, Dr. Dr. B. A. Cole, Prof. H. J. Crawford, J. B. Cumming,

Dr. R. Debbe, Mr. W. Eldredge, Dr. J. Engelage, Prof. S. -Y. Fung, Dr. M. Gonin, Dr. S. Gushue, Mr. L. F. Hansen, Mr. G. Heinzelman, Dr. E. Judd, Prof. J. Kang, Dr. M. J. Le Vine, Mr. H. Liu, Dr. J. Luke, Prof. A. Mignerey, Dr. B. Moskowitz, Mr. M. Moulson, Dr. M. N. Namboodiri, Prof. C. Ogilvie, Dr. J. Olness, Dr. L. P. Remsberg, Prof. J. Ryan, Dr. T. C. Sangster, Prof. R. Seto, Dr. J. Shea, Dr. R. Soltz, Dr. S. G. F. Stephans, Dr. M. J. Tannenbaum, Prof. J. H. Thomas, Dr. F. Videbæk, Dr. F. Wang, Dr. Y. Wang, Dr D. Woodruff, Mr. Y. Wu, Mr. H. Xiang, Dr. G. H. Xu, Mr. X.Yang, Prof. W. A. Zajc and Dr. Q. Zhu.

I thank Ms. C. Feliciano, a very kind and able group secretary, for her hospitality and guidance for a stranger in the United States.

I would like to acknowledge Mr. K. Asselta, Mr. E. Baker, Mr. H. Diaz, Mr. J. Dioguardi, Ms. B. McBreen, and Mr. R. A. Scheetz for their technical support, help, and kindness.

I thank a previous generation of Japanese students, Dr. S. Hayashi, Dr. H. Sakurai, Dr. Y. Tanaka, and Mr. H. Kaneko

I am grateful to the Tandem staffs and AGS staffs for delivering the Au beam. The E866 experiment is supported in part by the U.S. Department of Energy under contracts with ANL, BNL, the University of California at Riverside, Columbia University, LLNL, and MIT, in part by NASA under a contract with the University of California, and by the U.S.-Japan High Energy Physics Collaboration Treaty.

Finally, I would like to thank my parents, brother, sister, and my wife for their supports and encouragements.

Bibliography

[1] J. C. Collins and M. J. Perry, Phys. Rev. Lett. 34 (1975) 1353.

[2] T. Hatsuda, Nucl. Phys. A544 (1992) 27c.

[3] N. H. Christ, Nucl. Phys. A544 (1992) 81c.

[4] Z. Chen *et al.*, Proc. Winter Workshop on Nuclear Dynamics.

[5] Y. Akiba, *et al.*, Phys. Rev. C50 (1994) 1024.

[6] R. Hanbury-Brown and R. Q. Twiss, Nature 178 (1956) 1046.

[7] F. Bradamante, *et al.*, Phys. Lett. 32B (1970) 303.

[8] M. Aoki *et al.*, Phys. Rev. Lett. 69 (1992) 2345.

[9] M. Gyulassy, Proceeding of HIPAGS, BNL-44911.

[10] B. Anderson, *et al.*, Nucl. Phys. B281 (1987) 289.

[11] Y. Pang, T. J. Schlagel, and S. H. Kahana, Phys. Rev. Lett. 68 (1992) 2743.

[12] Y. Pang, T. J. Schlagel, and S. H. Kahana, Nucl. Phys. A544 (1992) 435c.

[13] H. Sorge, *et al.*, Ann. of Phys. C47 (1989) 266.

[14] A. Schwarzschild and Č. Zupančuč, Phys. Rev. 129 (1963) 854.

[15] H. H. Gutbrod *et al.*, Phys. Rev. Lett. 37 (1976) 667.

[16] J. Gosset, H. H. Gutbrod, W. G. Meyer, A. M. Poskanzer, A. Sandoval, R. Stock, and G. D. Westfall, Phys. Rev. C16 (1977) 629.

[17] S. Nagamiya, M.-C. Lemaire, E. Moeller, S. Schnetzer, G. Shapiron, H. Steiner, and I. Tanihata, Phys. Rev. C24 (1981) 971.

[18] B. V. Jacak, D. Fox, and G. D. Westfall, Phys. Rev. C31 (1985) 704.

[19] B. V. Jacak, G. D. Westfall, C. K. Gelbke, L. H. Harwood, W. G. Lynch, D. K. Scott, H. Stöcker, M. B. Tsang, and T. J. M. Symons, Phys. Rev. Lett. 51 (1983) 1846.

[20] J. W. Cronin, H. J. Frisch, M. J. Shochet, J. P. Boymond, P. A. Piroué, and R. L. Sumner, Phys. Rev. D11 (1975) 3105.

[21] J. Barrette, *et al.*, Phys. Rev. C50 (1994) 1077.

[22] N. Saito, *et al.*, Phys. Rev. C49 (1994) 3211.

[23] J. S.-Gillo, *et al.* Nucl. Phys. A590 (1995) 483c.

[24] T. Roser, 4th European Particle Accelerator Conference, EPAC-94, London England. BNL Preprint BNL-49700 (1994).

[25] R. Debbe, private communication.

[26] J. B. Cumming, E-866-MEM-16, BNL-62000 (1995).

[27] D. Beavis *et al.* Nucl. Instrum. Methods A281 (1989) 367.

[28] J. C. Dunlop and M. D. Baker, E-866-MEM-19 (1995).

[29] D. R. Nygren, LBL Int. Report (1974); D. R. Nygren, Phys. Scripta 23 (1981) 584.

[30] K. Shigaki, Master's thesis, University of Tokyo (1992).

[31] H. Sako, Master's thesis, University of Tokyo (1993).

[32] A. R. Clark *et al.*, Proposal for a PEP facility based on the TPC, PUB5012 (1976).

[33] E. Gatti *et al.*, Nucl. Instrum. Methods 163 (1979) 83; E. Mathieson and T. J. Harris, Nucl. Instrum. Methods 159 (1979) 483; H. Van Der Graaf and J. P. Wagenaar, Nucl. Instrum. Methods A252 (1986) 311; R. Bellazzini *et al.*, IEEE Trans. Nucl. Sci. NS-32 (1985) 389.

[34] C. R. Gruhn *et al.*, Proposal submitted to the CERN SPSC 84-13 (1984); C. R. Gruhn *et al.*, Nucl. Phys. A461 (1987) 391c.

[35] S. J. Lindenbaum *et al.*, Nucl. Phys. A461 (1987) 431; W. A. Love *et al.* (E810 Collaboration), Nucl. Phys. A498 (1989) 523c.

[36] A. Kumagai, Master's thesis, University of Tsukuba (1994).

[37] K. Ashktorab, M. J. LeVine, and R. A. Scheetz, IEEE Transactions on Nuclear

[38] D. Beavis, private communication.

[39] J.-H. Lee, private communication.

[40] CERN Computing and Network Division, GEANT 3.1.5 Manual.

[41] H. Sako, Doctor thesis, University of Tokyo (1996).

[42] H. Bøggild *et al.*, Nucl. Phys. B57 (1974) 77.

[43] V. Blobel *et al.*, Nucl. Phys. B69 (1974) 454.

[44] T. Abbott *et al.* (E802 Collaboration), Phys. Rev. D45 (1992) 3906.

[45] T. Abbott *et al.* (E802 Collaboration), Phys. Rev. C50 (1994) 1024.

[46] M. -C. Lemaire, S. Nagamiya, S. Schnetzer, H. Steiner, and I. Tanihata, Phys. Lett. 85B (1979) 38.

[47] A. Z. Mekjian, Phys. Rev. Lett. 38 (1977) 640.

[48] A. Z. Mekjian, Phys. Rev. C17 (1978) 1051.

[49] A. Z. Mekjian, Nucl. Phys. A312 (1978) 491.

[50] H. Sato and K. Yazaki, Phys. Lett. 98B (1981) 153.

[51] R. Mattiello, A. Jahns, H. Stöcker, W. Greiner, and H. Sorge, PRL 74 (1995) 2180.

[52] E. A. Remler and A. P. Sathe, Ann. of Phys. 91 (1975) 295.

[53] E. A. Remler, Ann. of Phys. 95 (1975) 455.

[54] E. A. Remler. Ann. of Phys. (NY) 136 (1981) 293.

[55] H. Sorge, A. v. Keitz, R. Mattiello, H. Stöcker, and W. Greiner, Phys. Lett. B243 (1990) 7.

[56] Phys. Rev. D45, Review of Particle Properties.